UNIVERSITÀ
DEGLI STUDI
FIRENZE

PhD in
Atomic and Molecular Photonics

CYCLE XXXVI

COORDINATOR Prof. Diederik Wiersma

Brain-wide mapping of the full intact mouse brain with micrometre-scale resolution:

Enhanced expansion microscopy and light-sheet microscopy for large tissue applications

Academic Discipline (SSD) FIS/03

Doctoral Candidate
Niamh Brady

Supervisor
Dr. Ludovico Silvestri

Coordinator
Prof. Diederik Wiersma

Years 2020/2023

Brain-wide mapping of the full intact mouse brain with micrometre-scale resolution:

Enhanced expansion microscopy and light-sheet microscopy for large tissue applications

I dedicate this thesis to my parents.

Table of Contents

Part 1 Introduction

Chapter 1 Motivation

One of the most fundamental requirements of all research is having the tools available to facilitate reaching the end objective; with the goal of mapping the neuronal architecture of the brain in mind specifically, sample preparation techniques and imaging modalities reveal the anatomy of the sample in question. The ability to analyse large intact volumes at various resolutions remains a palpable challenge. Current state of the art employs sophisticated techniques, often involving complex protocols, advanced and costly equipment, as well as being only adequate for small tissue volumes. Large samples, such as neuronal projections and circuits, cover an area greater that this limited data field causing them to be cut before imaging (H. Chen et al., 2021; Long et al., 2017).

Each organ system holds its own unique structure that corresponds to its functionality which generates a need to create whole structural maps to achieve an unbiased system-wide understanding. From a whole organ perspective, there exists extensive knowledge of all organ systems with the exception of one. This organ being the brain, where the knowledge of the relationship between spatial anatomy and the associated functionality is insufficient. At the core of neuroscience, the study of the nervous system must begin with a thorough understanding of the diverse networks and types of cells working in communication to achieve functionality of the four systems of motor, cognitive, sensory and behavioural state. Due to the highly complex anatomical systems and fine neuronal architecture spanning across multiple brain regions attaining complex and hierarchy distribution, the imaging and identifying of the heterogeneity is a daunting task while we work to increase our knowledge in securing a detailed map of the brain (Philipp J. Keller & Ahrens, 2015). The mouse brain alone is home to over 70 million neurons that interconnect between multiple regions, determining the organisation of these projections has been approached, specifically by the Allen Mouse Connectivity Project in which EGFP-labelled axonal projections from defined areas and cells, for example cortical areas reaching the thalamus, were imaged coupled with two-photon microscopy and a vibratome facilitating

physical segmentation (Oh et al., 2014). Other groups have since developed imaging and processing tools to trace and reconstruct projections using a whole brain sample, adding to the database of known projections. In 2019, a group developed and used a platform fulfilling this purpose to reconstruct over 1,000 neuronal projections across the motor cortex, subiculum, thalamus and hypothalamus (Winnubst et al., 2019). These methods, however, all require the physical slicing of the tissue, necessary for limiting penetration depth two photon penetration, compromising structural integrity and eliminating possibility for re-imaging.

When considering the investigation of whole neuronal circuits and projections in a mouse brain, techniques should ideally allow for the sample to be imaged as a whole, in an uncompromised manner (C. I. Bargmann & E. Marder, 2013). In order to study the associated functionality against anatomy, a clear map or established method able to resolve vast neuronal infrastructure must be achieved. Over time the focus on achieving higher resolution has increased in order to resolve these fine features over large volumes of brain tissue up to the entire mouse brain. Methods for full-brain imaging, such as MRI, are limited by the lack of resolution, advanced methods such as two-photon imaging are limited by the imaging depth and other immunohistochemical techniques have elevated our means in reaching our goal but can be difficult to apply to the whole brain. Indeed, the 3D morphology that expands over vast scales provides the key to understanding fundamental system-level mapping (Douw et al., 2021). With this in mind, neural research relies on robust protocols and imaging techniques in order to investigate neuronal circuits and projections in an unbiased, uncompromised and holistic manner. Until now, this aim has been limited to labs with specialised equipment and reagents. Here I present a novel pipeline consisting of a sample preparation technique that optically clears and expands biological tissue which I have adapted to the full mouse brain, improving the resolution in the sample itself, combined with a custom-built light sheet microscope capable of imaging the full expanded mouse brain, which comprises of standard laboratory equipment. A detailed description of the sample preparation protocol is given along with a comprehensive explanation of the design process and building of the light sheet microscope enabling this work to be replicated and expanded upon. Possessing the knowledge of neuronal systems facilitates a plethora of further research into the nervous system and fundamental brain functionality all which would help to better characterise the architectural alterations of the system with the correlating cognitive performance. This goal of mapping neuronal connections across the brain, termed the “connectome”, could

ultimately reveal the composition of the brain in general, as well as the unique differences between each individual (Cornelia I. Bargmann & Eve Marder, 2013).

Imaging human brain tissue presents its own set of unique challenges and subsequent implementations are dependent on the sample itself. Samples are precious due to the scarcity in which human brain tissue is available and suitable for specific research lines. Since most tissue is retrieved via autopsy, there can be a significant delay, often over 5 hours, between the death of the individual and the subsequent tissue retrieval making ultrastructure preservation and increasingly difficult task (DeFelipe, 2015). When considering adult human brain tissue specifically, the obstacles are also centred around the clearing of aged tissue and managing the sheer size of the sample (Rusch et al., 2022). Developing sample preparation techniques, strategic measures in facing these challenges must be considered. Once a technique has been established, customised imaging equipment can be designed around the sample and required mounting in order to achieve optimal image quality.

Utilising the non-invasive principles of light sheet microscopy and the resolution-enhancing capabilities of expansion microscopy, the work presented in this thesis details the experimental tools to achieve microscale resolution for brain-wide anatomical mapping. The key motivation of developing this pipeline is to provide methods that can be easily implemented in standard laboratories in a cost-efficient manner. This work facilitates the feasibility of more researchers contributing to the field of neuroscience, supported through the completion of the connectome map and understanding neuropathology. Although not limited to brain tissue, the work in this thesis focuses on the whole mouse brain. Indeed, having the experimental tools opens the doors to extracting the anatomical data and the geometrical arrangement.

Also presented in this thesis, is the work conducted alongside these developments in supporting large-scale, brain-wide mapping of the human brain. As part of this large-scale project, I discuss methods used to troubleshoot complications arising in standard, in-house built light sheet microscopes and how to improve image quality.

Thesis outline

The work is this thesis is broken down into 5 sections, comprehensively detailing the development of the sample preparation techniques, the design of the customisable light-sheet microscope and the associated applications of these novel tools.

Part 1 introduces the background to the phenomena that forms the basis to the motivation of this work and its progress up until this point.

Part 2 describes the development of Expansion microscopy techniques for large biological samples that until now, have been problematic for large volumes.

Part 3 describes the construction of a light-sheet microscope designed to accommodate fully expanded mouse organs using standard laboratory equipment, easily replicable and cost-efficient in producing micrometre resolution.

Part 4 describes an experimental workflow in which a customised dual-inverted light sheet was optimised specifically for the target of human brain tissue for brain-wide mapping and the methods to optimise image quality, trouble-shooting errors during long-term data acquisition.

Part 5 discusses the biological significance of the work produced in this thesis and its applications beyond this project. Future outlook is considered from these highly-adaptable, revolutionising tools.

Chapter 2 Fluorescence Theory

The well-established phenomenon of fluorescence was first described in 1852 by Sir G. Stokes, an Irish physicist and mathematician, when he observed the mineral fluorspar emitting light when illuminated by ultraviolet light. Interestingly though, Stoke observed that the emission light occurred at a wavelength longer than that of the excitation light. This shift in wavelength was termed the 'Stokes shift' is shown in figure 2.1, which is the shift measured from the peaks of excitation and emission spectra.

Fluorescence spectra express the probability by which a fluorophore will be excited and subsequently go through emission as a function of the wavelength corresponding to those processes. The absorption maximum refers to the wavelength most capable and so most efficient in exciting the fluorophore, the range of wavelengths across the spectra are also able to excite the fluorophore with a corresponding intensity. The emission maximum characterises the most likely wavelength output through emission as the spectrum provides the other wavelengths possible to be emitted at lesser intensities.

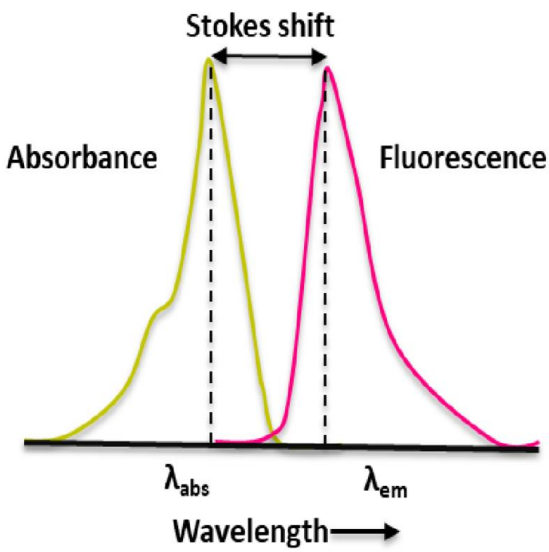

Figure 2.1 – Stokes shift

The difference in wavelength (energy, frequency, wavenumber) between band maxima of the absorption and emission spectra during electronic transitions in a system (atom or molecule). The transitions occur when a system absorbs a photon, gaining energy to move into an excited state. The system relaxes through the emission of a photon losing energy. The difference in the energy of the absorbed and emitted photon is termed the Stokes shift.
Modified from (Mazi, 2019).

On a fundamental scale, the absorption of a photon of electromagnetic light causes an electron within a molecule to be excited, able to move up to a higher energy state. This absorption of energy takes place in the closely-positioned vibrational and rotational energy levels of each excited state in the various molecular orbits.

These cycles of the movement through these various energy levels concerned with the absorption and emission of light were presented by Professor Aleksander Jablonski, a Polish physicist, in the classical Jablonski energy diagram. A many-level energy diagram providing a visual for these mechanisms which was first published in 1933 namely, the Jablonski Diagram: the characteristic behaviour of electrons in an atom due to the excitation by and emission of photons as shown in figure 2.2. This phenomenon which exists in some molecules, now named fluorophores, is due to this distinctive electronic structure.

The schematic diagram displays the increasing energy levels of the system from ground state including the spin states, shown grouped, taking singlet (S) or triplet (T) state. Each of these energy levels is further divided into vibrational and rotational states holding somewhat different energies.

An electronic transition is triggered by the absorption of a photon, exciting a system from the ground state, S0, to a higher energy state, S1 or S2. As the system quickly relaxes, energy can be dissipated in multiple ways. Internal conversion occurs in timescales of 10^{-14}-10^{-10} seconds, is a process bringing the electron to the lowest vibrational level, within the same state or between two if there is a strong overlap, where energy is dissipated. From which, the occurrence of vibrational relaxation, over a timescale of 10^{-12}-10^{-10}, takes places between different vibrational levels in a non-radiative way. The energy is dissipated by being given away as kinetic energy to other vibrational modes. This energy can stay within the same molecule or can be transferred to other molecules, closely neighbouring.

The longest sub-process in the complete fluorescence process occurs when an excited molecule exists in the lowest excited singlet state S1 in which timescales in order of nanoseconds occur. From here, the molecule relaxes down to its ground state accompanied by the emission of a photon, the mechanisms causing the fluorescence effect. Fluorescence is mostly observed between these states as higher energy levels would likely take the path of internal conversion or vibrational relaxation. A wide range of photon energies are triggered through this mechanism since the vibrational levels of the ground state are closely spaced. It is because of this that fluorescent emission intensity is noted over a range of wavelengths. The energy loss, as described by the Stokes shift, is

predominantly due to the rapid decay of energy to get to the lowest vibrational level in the S1 state. A consequence of this is that the emitted photon has less energy. Energy is dissipated also in the form of heat during the transfer of energy from the photon to the system. As by Kasha's rule, the "emitting level of a given multiplicity is the lowest excited level of that multiplicity" where multiplicity refers to the spin angular momentum of the level; 1 for singlet states and 3 for triplet states. What this means is that fluorescence occurs originally from the vibrational ground state of S1, the lowest exited singlet state and the same can be said for phosphorescence in which the phosphorescence originates from the vibrational ground state of the T1, the lowest excited triplet state. This rule arises due to the rate constant in complex molecules of the internal conversion and vibrational relaxation from the higher states is reasonably greater when compared to the rate constant characterising the return to the ground state (Kasha, 1950).

Intersystem crossing is the name of another pathway taken during the energy dissipation of a system as an electron changes its spin multiplicity from an excited singlet state to that of an excited triplet state (T1) which is of periods of 10^{-10} – 10^{-8} seconds. This relatively rare event results in phosphorescence as a photon is emitted, the slowest process in the Jablonski energy diagram in orders of 10^{-3}-100 seconds. Alternatively, delayed fluorescence can occur in which there is a transition back to the excited singlet state. Rate constants for triplet emission, phosphorescence, are much lower than those for fluorescence as unfavourable processes must happen. Spin conversion as first order must take place in molecules, producing unpaired electrons and allowing second order processes to happen. Importantly, the triplet state enables high chemical reactivity in molecules when in this state consequently leading to photobleaching and also producing damaging free radicals.

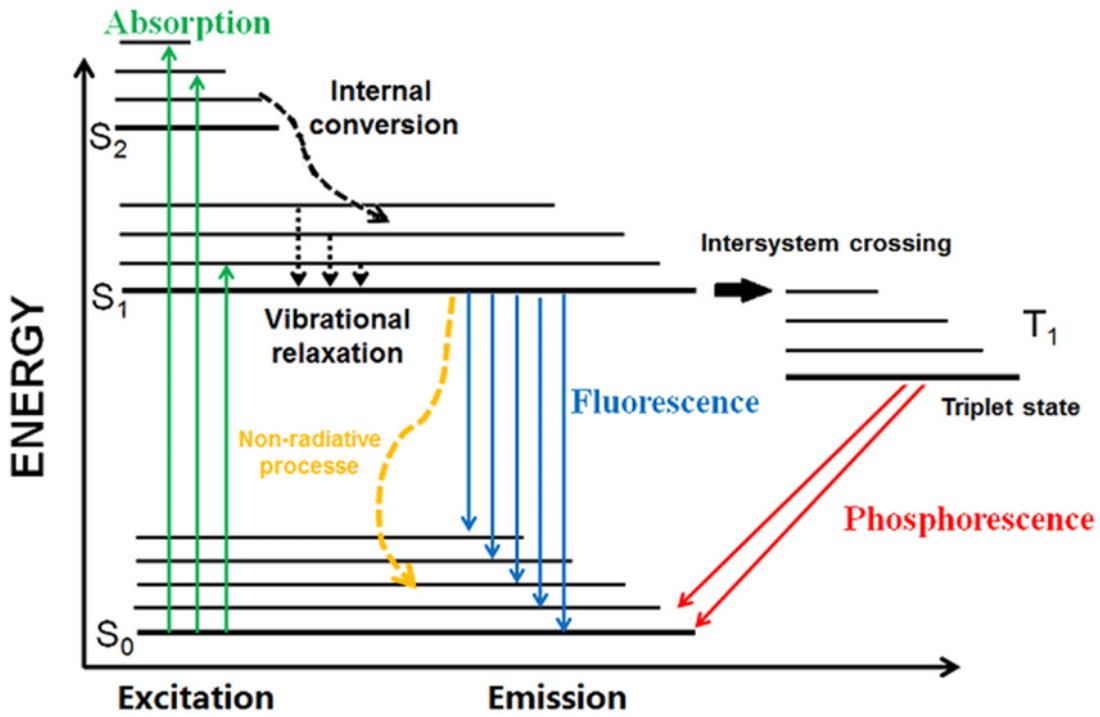

Figure 2.2 – Jablonski diagram

The schematic illustration of the electronic states and their corresponding energies in an atom or molecule which are arranged vertically by increasing energy. The grouping of each state represents the spin multiplicity (singlet or triplet). The vibration levels are indicated along with the associated electronic transitions.
Adapted from (Schweizer, Kubach, & Koch, 2021).

The high reactivity is a product of the long-lived triplet state, creating a dynamic that is more susceptible to interacting with other molecules as more molecules exist in this state over longer periods of time. However, even in an excited singlet state, interactions with molecules can occur, potentially creating permanent covalent modifications. The more cycles of excitation and emission that happen give rise to the increased possibility of these various events occurring which in turn lead to the photo-bleaching of the sample; a phenomenon in which the fluorophore ceases to fluoresce due to environmental factors occurring over time, this effect is demonstrated in figure 2.3. Reducing factors, such as light intensity or exposure time, successively limits the cycles of excitation and emission that a system can undergo and therefore minimising the risk of photo-bleaching. Consequently, the signal is reduced and hence a balance should be calculated.

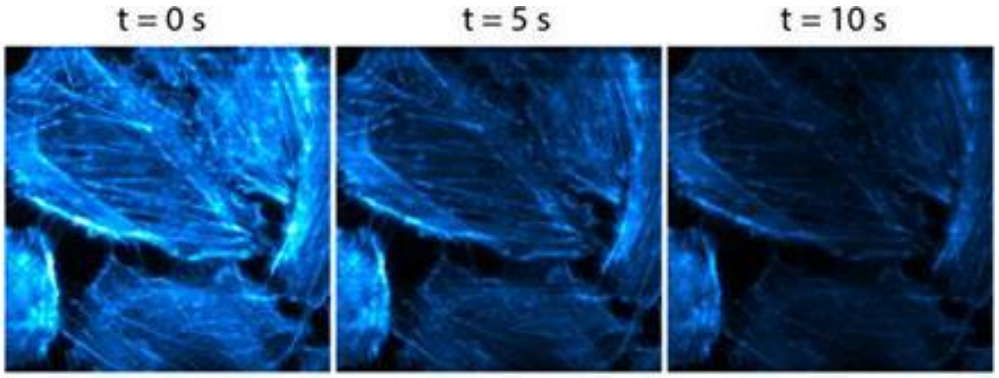

Figure 2.3 – Photobleaching of a sample through time

As the sample is more exposed to illumination light, the molecules are able to go through the excitation-emission cycles, vulnerable to environmental factors likely to cause photobleaching. Adapted from (Tang & Han, 2019).

During the mid-1900s, initial investigations into this phenomenon found that many specimens, such as crystals and vitamins, naturally fluoresce when exposed to ultraviolet light; this was termed 'autofluorescence'. Some of the more common biomolecules molecules showing high degrees of autofluorescence are those containing collagen and elastin (Monici, 2005). Despite being exploited for gain in many circumstances, autofluorescence also generates some issues, when present, particularly at high amplitudes, during the detection of exogenous emission (Croce & Bottiroli, 2014). In order to address these issues, strategies in the form of optical filtering were used in order to block the emission of unwanted fluorescence or in post processing to filter out any unwanted signal (Monici, 2005) (Hüpfel, Yu. Kobitski, Zhang, & Nienhaus, 2021; Toader et al., 2022). An alternative method is to bleach the sample in a pre-irradiation session.

Chapter 3 Creating Fluorescent Samples

Fluorescent biological samples emit complementary information encoded within the sample itself. These samples can be created featuring endogenous fluorescence or go through external administration of the fluorescence. While endogenous fluorescence facilitates minimal disturbance to the sample, exogenous fluorescence permits more selective specificity of many target features.

The broadened range of data acquired from the physical visibility of biological structures generates more and more ability to bridge the knowledge between biological structures against their functionality: what is essentially the key to understanding life. The applications fostered from the advancing approaches include, developmental biology, progression and treatment and disease, as well as the morphology of neuronal projections in the brain.

Discussed in this chapter are the various methods to render a sample fluorescent but first a discussion into the mouse model that serves popularly and commonly as a model in brain mapping using fluorescent imaging techniques.

3.1 The mouse model

The history of the mouse model in biomedical research

For well over a century, rats and mice have been some of the leading models in biomedical research with mice taking lead as a major model due to the increased genetic flexibility associated. In the quest to have a greater understanding of the human brain functionality, appropriate models should closely mirror mechanisms occurring in the human brain. Despite not attaining a full phenocopy of human disease, the mouse model features similar

pathologies and pathophysiologic events that can be associative to humans. For more than 100 years, science has taken tremendous leaps forward through amassing knowledge of the mouse physiology, anatomy and genetics.

The rise of the mouse model effectively took steam in 1915 when John Burdon Sanderson Haldane began to genetically map the mouse, continuing to be built upon over the following 50 years. Indeed, understanding their genetics would go on to inspire the successive decades. Genetic modification emerged in 1980 with the advent of various techniques, including the first 'knockout' mice which removed isolated genes in order to determine its unique role (Austin et al., 2004). The Human Genome Project launched in 1990 giving results which were able to be compared to those of mice; extraordinarily showing a striking similarity to the genetics of the results of mice, almost all genes are shared or found in a similar form with only less than 10 of the 4000 studied found not to be communal (Collins & Fink, 1995).

From this time, the era of genetically modified mouse models joined the world of neuroscience to create incredibly diverse models replicating human conditions overcoming a huge hurdle in human brain research.

The mouse brain for human brain mapping and research

The study of the human brain is challenging for different factors, particularly in that human brain samples are more difficult to obtain, especially those without being pathological or compromised by disease. Many techniques have low throughput adding on to the prior contest. Since human brain samples are very precious, the use of other models sharing relevant neurophysiology support the revelation of neuronal anatomy pertinent to the human brain.

Machine learning has been a useful application in rapidly identifying and classifying cell types and features. This was demonstrated by a group in which only electrophysiology data was used to identify Parvalbumin (Pvalb) cells using machine learning techniques with ~76% accuracy (M. H. Kim et al., 2023). Kim et al. found supporting evidence in this study of the similarities between mouse and human brains on the neuronal level and associated connections. For example, the Pvalb cells that were identified were part of a studied circuit motif in the human brain. In this circuit motif there was an excitatory neuron, a pyramidal cell, and an inhibitory interneuron, the Pvalb cell. The rate and quantification of neurotransmitters released at the synapse between these cells determines whether early-

onset inhibition or late-onset inhibition is likely to occur, as depicted in figure 3.1. Furthermore, the transcriptomes of cells, Pvalb and Somatostatin (Sst), taken from the cortex in the mouse and human brain were compared revealing the similarities; over 70 genes relating to the connection between neurons characterising the events occurring in the synapse. This circuit also exists within the mouse brain, suggesting that these interneuron subclasses have been conserved despite years of evolution, making it an ideal model for further studies of this circuit motif.

At a glance, the human and mouse brains display obvious differences, the prior being much larger and more complex, for example more neocortical invaginations, than the latter. The amount of specialised zones in the human brain outweighs those of the mouse brain as well as the thousand-fold difference in size and quantity of cells. However, the increasingly detailed maps of both architectures reveal homologous features, in particular the compelling evidence of similar inhibitory circuit motifs, that still exist in both brains since the last common ancestor existed 65 million years ago.

Once the physiology and morphology of these circuits is established, further investigations can take place to understand their role in disease and functionality, shared between both species. Other studies systematically investigate autopsies and their function in both human and mice brains revealing substantial similarities (Szegedi et al., 2020). More recently, McFarlan et al, investigated further the role carried out by inhibitory interneurons and their respective plasticity contributing to healthy functionality. The study was conducted on mouse brains due to the prior knowledge of the paralleled mechanisms in both mouse and human cortex (McFarlan et al., 2023).

Not only for genetic reasons and the ability to be very specifically genetically manipulated, mice are widely used as they can also be inbred to generate identical strains, a prominent tool for repeatability and accuracy in experiments. They can host patient tumours and other specific gene mutations found in humans. These animals also have shorter lifespans, with one mouse year being equivalent to around 30 human years, permitting the study of complete life cycles. Fundamentally, the production of mice as a research tool is efficient and cost-effective; they can be reproduced very quickly as well as being easy-handled and easy to transport.

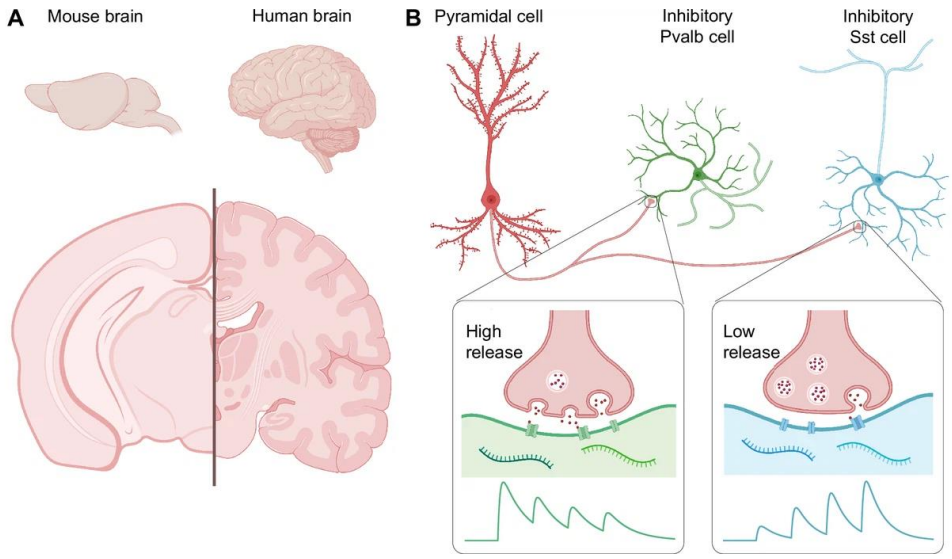

Figure 3.1 – Comparison of the mouse and human brain

Inset (A) depicts how the larger human brain displays more neocortical invaginations through its larger volumetric area. Inset (B) Neuronal types and respective connections are similar between the mouse and human brain. Rapid and high release of neurotransmitters found at the synapse between pyramidal and Pvalb cells leads to early-onset inhibitions, shown in green. The contrast of low and gradually increasing release leads to late-onset inhibition, shown in blue. Due to these shared structural and functional characteristics, the mouse serves a good model for human brain studies in this respect.
Adapted from (Wong, Chou, Watt, & Sjöström, 2023).

Neuronal circuits

Considerably the building blocks of functionality, neuronal circuits are the components that make up the architecture of the brain. Each input and output neuron forms part of a wider set of neurons, eventually forming the circuits responsible for particular functions. The study of this complex anatomy can facilitate the research into what makes life function in the way it does and why disease takes over the body.

Circuit motifs contain varying fusions of interconnected excitatory and inhibitory neurons. Displayed in the mouse model, diseases such as epilepsy and autism create an imbalance between the excitation and inhibition in the brain (Nelson & Valakh, 2015). Until now, there

have been significant steps in associating these networks to processing sensory information, how various stimuli can motivate behaviours, learning and maintaining memories and the morphological differences in sex-shared neurons (Lohse, Bajo, King, & Willmore, 2020) (Al-Hasani et al., 2015) (Ruder et al., 2021) (D. Kim & Kim, 2022).

3.2 Endogenous fluorescence

1955 marked the year in which the first publication described fluorescent material present in biological tissue; the eosinophils of the Hydromedusae, a subclass of jellyfish (Davenport, Nicol, & Russell, 1955). Although unknown at the time, what was described was actually green fluorescent protein (GFP). In 1962, the photogenic component was officially confirmed to be a protein by Osamu Shimomura at Princeton University (Shimomura, Johnson, & Saiga, 1962). The extensive and widespread use of GFP initiated in 1994 after a paper, published by Professor Martin Chalfie at Columbia University, demonstrated the ability of the gene encoding GFP to be expressed in prokaryotic and eukaryotic cells (Chalfie, Tu, Euskirchen, Ward, & Prasher, 1994). This work ultimately led to a shared Nobel Prize in Chemistry victory in 2008, together with Roger Tsien, for their part in the discovery and application of GFP.

From this time, many variants have been engineered, revolutionising the field of microscopy and biomedical imaging: the variants are equipped with different colours of the spectrum, named after their respective associated wavelength. The tremendous manifestation of light-matter interaction provides samples which are intrinsically capable of emitting fluorescent signals under excitation. The specific emission profiles and high specificity of fluorescence can be exploited to understand the spatial organisation within a sample.

These unique variations, and distinguishing shifts between the excitation and emission wavelength, are characterised by each fluorophore's molecular structure and electron configuration (Germond, Fujita, Ichimura, & Watanabe, 2016).

Transgenic animals

Transgenic animals, facilitated by genetic engineering, have alleviated descriptive life science research into an actionable and adaptable paradigm. Various types of transgenic

animals, of GFP and other similar proteins, serve as models for mapping neurons in which the proteins and axon pathways express fluorescence endogenously. Initially, the coding sequence of the fluorescent protein is introduced into the sample in order to encode the DNA (Ikawa et al., 1995) . The fluorescence can be localised to specific targets so that a comprehensive map of the networks can be made from the distinct signals coming from the relevant cells expressing endogenous fluorescence (Arias, Manubens-Gil, & Dierssen, 2022). The fluorescent signal enhances the viability of the fine anatomical features within a sample since the areas of fluorescence are known prior.

Viral vectors

Fluorescence can also be delivered to the sample via an injection of a virus equipped with fluorescent markers. This method is most commonly used to facilitate neuronal tracing, particularly those which travel between different regions of the brain (Bartlett & Samulski, 1998).

This method utilises the infecting nature of viruses that migrate through neurons, having the ability to travel across synaptic connections. The movement of these viruses takes one of two forms: anterograde tracing starts from the cell bodies and migrates to the axon terminals while retrograde tracing flows in the opposite direction. The advantages of this labelling technique is that the targeted infection is specific to a desired target which can be labelled more quickly than the production of a transgenic animal.

Specifically, adeno-associated virus (AAV), containing a single-stranded DNA molecule, is widely used within neuroscience due its ability to inhibit neuronal cells with genetic material. Since the AAV particles are small in size (20 nm) and have low immunogenicity, they can diffuse easily in the extracellular regions.

GFP-tagged AAV vectors have been employed in a variety of studies: to study cellular trafficking and nuclear entry (Lux et al., 2005) and protein-protein interactions (Becirovic et al., 2016).

3.4 Tissue clearing and immunofluorescence

Many protocols consist of immunofluorescence, which follows the physical sections of the samples in order to image them consisting of fewer layers of cells. This allows the light to penetrate enough to view the sample as well as providing a shorter distance for antibodies to permeate through to reach the targets (Long et al., 2017). However, these slices must be eventually aligned in order to generate a three-dimensional reconstruction of the sample, a cumbersome approach that is time-consuming and error-prone.

In the 1900s, German scientist Werner Spalteholz developed a technique that renders biological tissue transparent since tissue is opaque due to the highly-scattering lipid content (J. Zhao, Lai, Qi, He, & Sun, 2021). Since then, many other tissue clearing methods have emerged, (Azaripour et al., 2016) (Renier et al., 2014), each with corresponding strengths and weaknesses; the various techniques include hydrogel embedding such as CLARITY (Chung & Deisseroth, 2013), organic solvent-based protocols such as BABB (Foster et al., 2019), and 3DISCO (Ertürk et al., 2012), and aqueous-based such as Scale (Hama et al., 2011), and SeeDB (Ke, Fujimoto, & Imai, 2013). Each of these methods, and those emerging, are continuously under development so that they have more practical implementation across different samples, for example large samples, and greater compatibility with labelling techniques. Elegant labelling techniques strive to improve the rigidity of fixation procedures to permit the use of stronger reagents and methods, for example through the use of stochastic electro-transport which uses electric fields to force electro-mobile molecules through the tissue to enhance the penetration time (S. Y. Kim et al., 2015).

Figure 15 (A9 depicts the underlying principles, both chemically and physically, in which the homogenisation of the refractive index (RI) of the biological specimen and the mounting medium minimises the scattering of light. While on the other hand, the removal of haemoglobin, myoglobin and melanin reduces the absorption of light. Each clearing method attempts to optimise these parameters arising from refractive index mismatch. Water has a low RI of ~1.33, while dry lipids exhibit those within an intermediate range of ~1.46-1.48, (Pusterla, Malfatti-Gasperini, Puentes-Martinez, Cavalcanti, & Oliveira, 2017), and higher RI values of ~1.540-1.598, (Bashkatov et al., 2018), are exhibited by dried proteins and dry DNA.

A transparently-rendered biological tissue is a sample that is capable of permitting light to deeply enter a sample with little scattering while preserving the structural integrity of the

sample and therefore the spatial resolution of proteins and nucleic acids, components which are often aimed to be preserved during the clearing process. Three chemical processes are frequently established during tissue-clearing methods: delipidation to remove lipids that cause scattering of light, decolourisation to remove pigments, immersing in a medium that matches the RI of the biological sample (Ueda, Dodt, et al., 2020).

Following tissue clearing, the RI of a biological tissue-polymer hybrid can be calculated using the Lorentz-Lorenz equation, figure 15 (B). Since biological tissue is composed of varying sub-structures and non-uniform constituents, the RI is seldom homogeneous throughout. The Lorentz-Lorenz equation considers the contributing elements, such as the monomer refractive index (Rm) and monomer volume (V) in order to calculate an average refractive index (Rp).

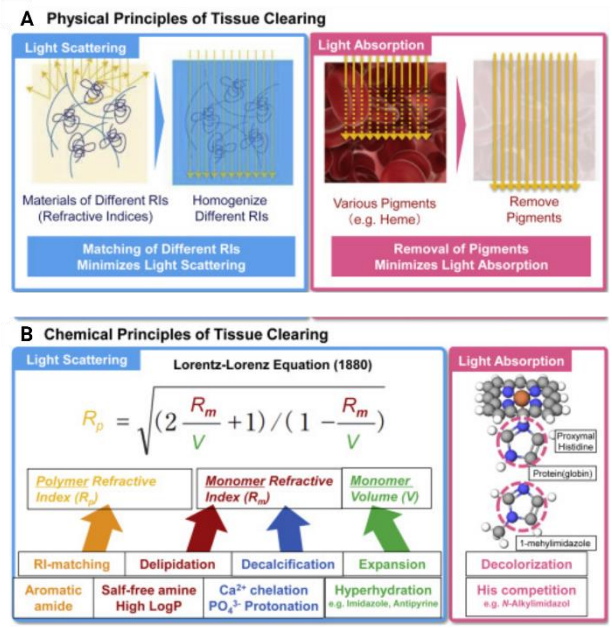

Figure 3.4 – Principles of tissue clearing, physical and chemical.

(A) depicts the physical principles of the process of tissue clearing, proposed by Spalteholz. The homogenisation of RI in the sample minimised scattering and the removal of pigments reduces light absorption. (B) shows the contributing factors to the composite RI of a cleared biological sample which employs the Lorentz-Lorenz calculation. This is used to find an appropriate RI-matching solution for the sample.
Adapted from (Ueda, Dodt, et al., 2020).

3.3 Exogenous fluorescence

Fluorophores (or fluorochromes) were developed through the chemical synthesis of fluorescent molecules to bioactive reagents, such as antibodies, in order to enhance biological investigations. These antibodies, equipped with fluorophores, act as fluorescent probes to attach to specific proteins, labelling specific features such as molecules, cells, organelles; this has been employed both in vivo and ex vivo (Gu, Xing, Han, Tso, & Hong, 2009) (Levanon et al., 2010). Fluorophores are fluorescent chemical compounds that emit light following irradiation. Researchers were then able to specifically target components and stain them with these fluorescent markers in order to specifically image these features using a fluorescent microscope. This technique has become a well-utilised tool in many fields from biomedical sciences to material science.

Moreover, producing fluorescent samples exogenously enables the use of a more flexible labelling approach since the researcher is able to be flexible with the fluorescent target as well as being less time consuming than producing transgenic animals.

Immunofluorescence

The development of fluorophores designed to target a greater range of components paved the way for new insights into fields involving physiological research. Features of interest can be labelled using immunofluorescence (IF). This technique labels the antigens of specific targets with a fluorophore, conjugated to an antibody, which facilitates the detection of the target biomolecule through increasing the quantity of photons. IF can also be expanded to be used as a signal amplification method. In some applications, in which the endogenous signal is weak or compromised by other treatments, it becomes necessary to boost the signal already present.

With the purpose of maintaining antigenicity, the samples must be fixed before performing IF. Fixation is required in order to preserve the sample morphology, locking the biomolecules in place as they are in their natural condition while autolysis is avoided. Fixation methods must cause little disruption to the cellular architecture while immobilising antigens in a way that provides an accessible route for the antibodies to reach the target. Fixation methods need to be empirically selected with respect to the target antigen since the nature of the methods can conserve a particular epitope immunoreactivity while degrading that of another. Chemical fixation methods utilise cross-

linking reagents, such as formaldehyde and glutaraldehyde, or organic solvents such as methanol and acetone (Im, Mareninov, Diaz, & Yong, 2019).

Following fixation, IF can be performed to bind the fluorophore-conjugated antibody to the target antigen. There are two ways in which to achieve this: direct and indirect immunofluorescence.

In direct immunofluorescence a single antibody, equipped already with a fluorophore, targets the antigen. Once bound, the fluorophore can emit the subsequent light following irradiation as shown in figure 2.2. These fluorophore-bound antibodies tend to be costly compared to indirect immunofluorescence antibodies yet give grounds to a shortened technique.

Indirect immunofluorescence requires two different types of antibodies to label the target antigen, a primary and a secondary. Despite the extra step and subsequent time necessary, the sensitivity of this technique is higher since multiple fluorophores are able to be conjugated achieving greater signal and so easier detection, as shown in figure 3.3.1 Furthermore, these antibodies are usually less costly than those required for direct immunofluorescence.

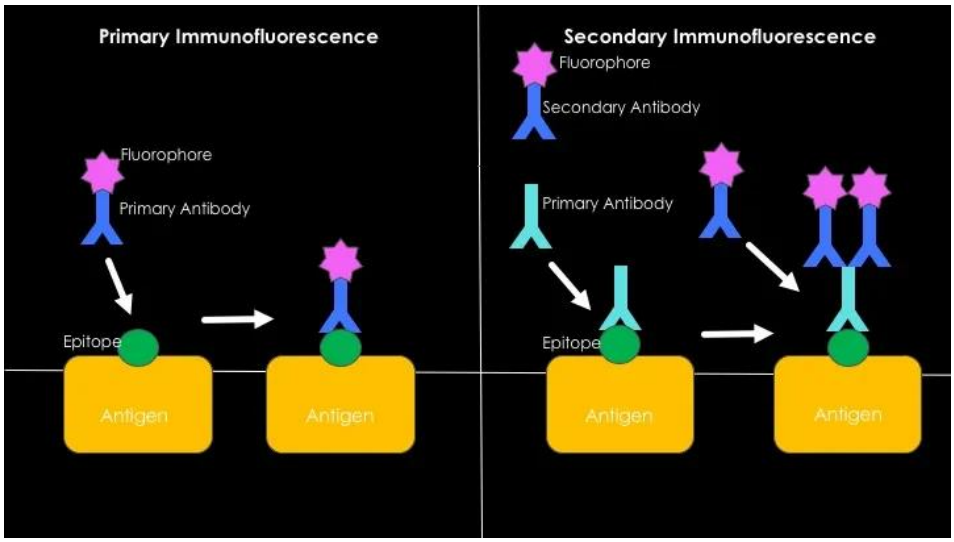

Figure 3.3.1 – Primary immunofluorescence versus Secondary Immunofluorescence

Both sharing a similar structure, antibodies have 3 portions and are Y-shaped molecules. They are made of two identical light chains and also 2 identical heavy chains. The two heavy chains are

bonded by di-sulphide bonds which then bond to a light chain. The direct immunofluorescence is ready to produce a signal as the first antibody binds to the antigen while in indirect immunofluorescence, secondary antibodies facilitate the ability to be detected.
Adapted from *Wikimedia Commons*.
https://commons.wikimedia.org/w/index.php?title=File:Immunofluorescence_Mechanism_.png&oldid=573832812.

Multiplexing (Multispectral imaging)

Multiple fluorescent probes can be used simultaneously to identify and gain spatial information of a variety of features in the same sample at the same time, optimising sample preparation time and imaging. Since the emission wavelengths of these markers range from ultraviolet-visible to near-infrared, the user is able to strategically select the fluorophore colligated to each target. The subsequent sample contains a variety of features that will individually fluoresce under different excitation wavelengths. This process is known as 'multiplexing' (Hickey et al., 2022). The use of multiple excitation wavelengths and appropriate detection filters, allows the production of images showing only the desired feature in a single acquisition, as shown in figure 3.3.2.

This method also assists in avoiding the nuisance of autofluorescence. The exogenous fluorescence can be selected to have an emission wavelength in a range outside that of the natural fluorescence so as to only allow the detection of the appropriate photons.

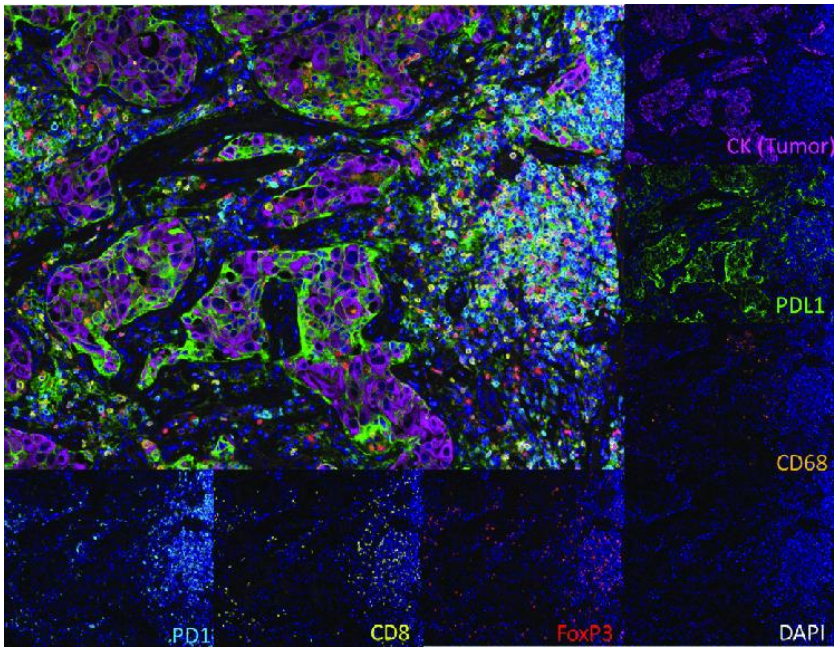

Figure 3.3.2 – Multiplexing components and final image

Multispectral imaging with 6 targets with individual fluorophores that are excited separately with their corresponding excitation wavelength. The images are combined to create a highly detailed image with much spatial data.
Adapted from (Taube et al., 2020).

Chapter 4 Light Sheet Fluorescence Microscopy

Optical microscopy has been in use since times before the 18th century. The traditional optical microscope utilises lenses to produce a magnified image of a smaller sample that has been illuminated with visible light. This magnified image of the sample can then be used for analysis.

Fluorescence microscopy further enhances these capabilities. Visible light is used to excite the fluorescence present in the sample. The subsequent light emitted by these fluorescent species creates an image from the collected photons reaching the sensor as opposed to the original source of light as done in traditional microscopy.

4.1 Light sheet microscopy

The light sheet microscope, in its simplest form, appeared in 1903 by Siedentopf and Zsigmondy, described as ultramicroscopy, in which gold particles were observed by sunlight projected through a slit aperture. It wasn't until 90 years later that a system of this nature re-appeared in the form of orthogonal-plane fluorescence optical sectioning (OPFOS) which featured the common elements present in modern light sheet fluorescence microscope (LSFM) (Voie, Burns, & Spelman, 1993). This setup was then used to, for the first time, optically section cochleae that had undergone staining and immunofluorescence (Voie & Spelman, 1995). Optical sectioning is the process by which thin slices of a larger sample are illuminated in the imaging plane and therefore emitted photons are collected only from this section as out-of-focus light isn't a contributing factor. This process avoids the need to physically section the sample in order to illuminate sections that are deeper in the sample. Despite the plethora of imaging processing programs to regenerate 3D structures from multiple slice images, image stacking can be unreliable, anisotropic in nature and laborious.

The process of physical sectioning also can compromise the structural integrity of fine features in the sample. Fiji (Schindelin et al., 2012), MATLAB (Křížek, Lukeš, Ovesný, Fliegel, & Hagen, 2016) and Imaris (Haass-Koffler, Naeemuddin, & Bartlett, 2012) have aided in these processes while tissue slicing was unavoidable.

Arne Voie and David Burns, the creators of OPFOS, took inspiration from resources around them; specifically, the front cover of a book on photomicrography, "Photomacrography, an introduction" by William White (1987), that appeared to feature an image on the cover of a sectioned pig embryo as well as a description inside the book of a microscope with a side-illuminating light sheet.

During the production of OPFOS, a group was simultaneously trying to improve the axial resolution of the confocal microscope which led to the production of a confocal microscope with oblique illumination in 1995, termed the confocal theta microscope (Lindek, Pick, & Stelzer, 1994). This setup laid the foundation for the group to go on to develop the selective- (or single-) plane illumination microscopy (SPIM), the fundamentals behind the multiple compositions of light sheet microscopy. The basic principles of the set up are shown in figure 4.1.

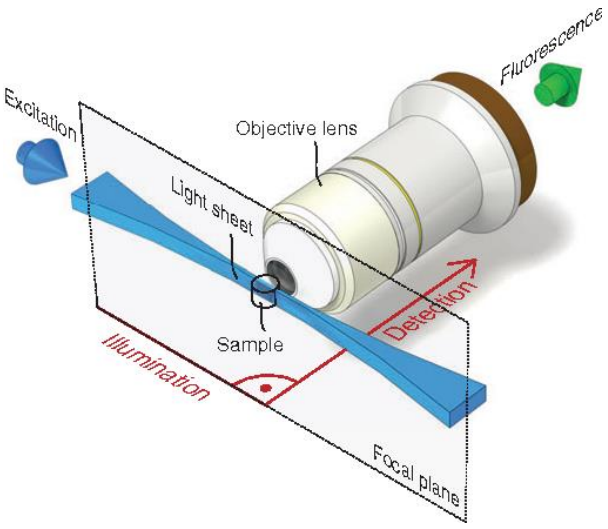

Figure 4.1 – Principle of set-up of the light sheet microscope

The detection and excitation pathways are positioned perpendicularly from each other. The sheet of light penetrates the sample to fill the detection field of view with a signal allowing for a fast and non-invasive illumination in transparent samples.
Adapted from (Huisken & Stainier, 2009)

2004 is when the development and implementation of the LSFM really took speed, following the publication of the SPIM article (Huisken, Swoger, Del Bene, Wittbrodt, & Stelzer, 2004). This particular article drew attention to the possible application of this technique when the development of embryos was investigated over a period of time taking imaging to 4 dimensions (x, y, z, t). Due to the high-penetration depth, high acquisition speed, non-invasiveness and low photo-bleaching qualities, it is established as an ideal tool suited to time-lapse experiments.

Over the last couple of decades, various adaptations have been made to the initial setup, each with features appropriate for the sample in question. The combination of enhanced features led light sheet microscopy to be crowned the 'Method of the year' in 2014 by Nature methods ("Method of the Year 2014," 2015).

LSFM has been widely used for the imaging of large specimens since the camera field of view can be fully made use of as an entire focal plane can be illuminated, provided by optical sectioning. This, in turn, reduces imaging time significantly when compared to other imaging techniques such as confocal microscopy which only permits a small area, the width of the illumination beam, to be imaged while causing out-of-focus fluorescence and bleaching in the subsequent laser path. Due to the axial confinement of illumination, LSFM also addresses one of the major challenges in fluorescence microscopy in general, the effect of photo-toxicity and the resulting photo-bleaching of the samples. Through side illumination, especially by a digitally scanned light-sheet, the field of view is illuminated over a shorter period of time, effectively maintaining the sample health for a longer time (Reynaud, Krzic, Greger, & Stelzer, 2008).

When comparing LSFM to other techniques, the acquired benefits of the technique must also withhold the standards set previously with regard to spatial resolution. Indeed, the resolving power of any system should fit the purpose of the experimental requirements. Often, diverse approaches are implemented to surmount these goals in order to not compromise other factors through the pursuit of extraneous resolution.

4.2 Applications of LSFM

Developmental biology has seen large strides made using LSFM. The technique changed the game since large specimens rely on deep light penetration, a challenge with respect to both illumination and detection. Small organisms, largely embryos and larvae (Huisken et

al., 2004), as well as fully-cleared organs have been imaged, generating the mapping of the vascular structure of the heart that, in turn, gave rise to a more profound development of associated coronary disease (Nehrhoff, Ripoll, Samaniego, Desco, & Gómez-Gaviro, 2017).

The nervous system has been imaged across all scales, from the single neuron, to the dendritic arbour and up to the system in its entirety (Haslehurst, Yang, Dholakia, & Emptage, 2018).

3D organoid cultures, stem cells that are able to self-organise to form a structure that shares the morphology and functionality of real organs, benefit greatly from the higher imaging depth provided (Beghin et al., 2022).

It isn't just the high penetration depth that has seen the technique heavily implemented, the temporal resolution and low photo-exposure attract the study of cell-sized samples. During the dynamic processes of cell motion, cell tracking and Ca^{2+} activity, the speed of imaging is paramount. Sampling frequency is increased through the fast sequential process of volumetric imaging (Wan, McDole, & Keller, 2019).

Resolution

Isotropic resolution is difficult to achieve using light sheet microscopy since lateral and axial resolution is influenced by differing components. The lateral resolution is governed by the numerical aperture (NA) of the detection objective alone while the axial resolution of a LSFM is achieved based on the interception of the focal planes by detection and illumination: the thickness of the light sheet, combined with the numerical aperture (NA) of the detection objective. Axial resolution is generally governed by the thickness of the light sheet and the NA of the detection objective and can be practically measured when a system is built.

The NA, equation below, is defined by the refractive index (n) of which the light input forms the beam and the sine of the ray angle of which the system can collect light (θ) (Paschotta).

$$NA = n\ sin(\theta)$$

In order to quantify the lateral resolution of the system, the point spread function (PSF) can be taken in the lateral directions. The PSF is a physical diffraction, shown in figure 4.2.1, pattern in three-dimensions emerging through the objective of NA that has been taken

from the light emitted from a light source in the imaging plane. The NA plays a significant role in determining a desired resolution; a higher NA generates a more refined cone increasing the resolution capabilities yet generally attains a lower depth of field. The minimum distance between two point sources that can still be individual resolved is the lateral resolution of the system.

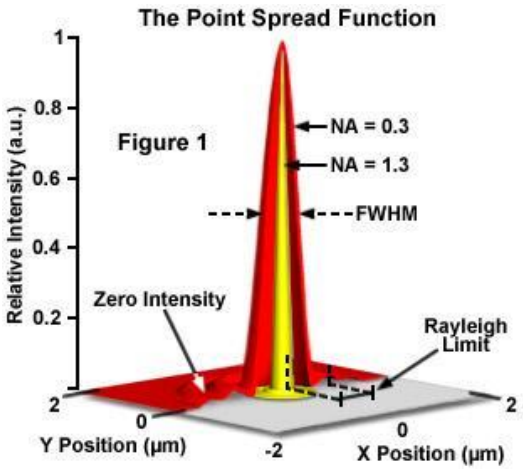

Figure 4.2.1 The point spread function

The relative intensity is plotted as a function of the x and y spatial positions to form the PSF. The image shows the difference in full-width at half-maximum (FWHM) for different NA objectives.
Adapted from *Ziess*
From https://zeiss-campus.magnet.fsu.edu/print/basics/psf-print.html

Theoretically, the value of the lateral resolution can be calculated by the respective point spread function laterally using the equation below (Olarte, Andilla, Gualda, & Loza-Alvarez, 2018). It can then be experimentally measured using fluorescent beads placed in the imaging plane; the beads should be of the same illumination and emission range of the target that the system will image as wavelength contributes to the result.

$$PSF_{lateral} = \frac{0.61\,\lambda_{emission}}{NA_{detection}}$$

Ultimately, a light sheet with a larger thickness than that of the axial point spread function governs the overall axial resolution. Using a lower NA lens for excitation produces a light-sheet with a thicker beam waist yet a more homogenous sheet over a longer distance. The thicker beam waist limits the axial resolution yet this can be enhanced by the detection objective resolving power. What can't be avoided, is the presence of more out-of-focus fluorescence and scattered light producing spatial frequency background noise which varies between each pixel as photons reach the detection. These factors all contribute to a high signal-to-background ratio and, consequently, poor image quality. Methods have been implemented in post processing to correct this in which models of the noise are applied to automatically tune the fidelity of the data and regularising it to a discrepancy principle or methods that use discrete wavelet transforms that decompose images into their varying frequency components and reconstructed after filtering the noise in the data (Toader et al., 2022) (Hüpfel et al., 2021).

Principle of setup

Given the flexible adaptability of the light sheet microscope, the key aspect of inspiration for the design should be the specific question or application. The light-sheet microscope exists in many forms, arbitrarily constructed to accommodate the sample itself (Power & Huisken, 2017) . What separated LSFM from other fluorescent imaging techniques is the decoupled, often orthogonal, illumination and detection arms, as shown previously in figure 4.2.2. Another feature unique to the LSFM is the ability to optically isolate each axial-plane within the sample, illuminating and imaging one layer at a time through the axial direction.

The illumination arm is preceded by optics designed to produce the light sheet which can take a variety of profiles. Most commonly implemented are light sheets featuring a Gaussian beam profile, as shown in figure 7, where the beam waist (w_0) is defined by the parameters which the irradiance falls between $1/e^2$ of the maximum value.

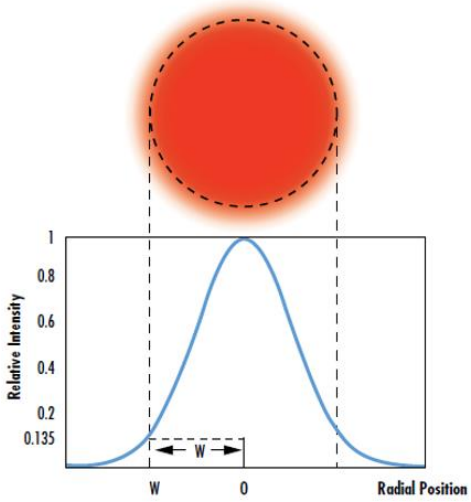

Figure 4.2.2 – Gaussian beam waist

Defined by the location at which the irradiance is $1/e^2$, or 13.5%, of the maximum value.
Adapted from *Edmunds optics.*
From https://www.edmundoptics.com/knowledge-center/application-notes/lasers/gaussian-beam-propagation/

Initial designs saw the light sheet formed by a cylindrical lens in which the beam retains its width while focusing its height until reaching the focal point where the beam waist is formed and, from here, continues to increase in thickness. The confocal parameter (b) characterises the distance in which the beam waist remains roughly constant that is also the range in which the sample appears to be in focus, a characteristic dependent also on the wavelength of the light source (λ). Outside of this range, the features become blurred and undefined. The degree of convergence and divergence, the convergence angle (θ) is measured using these parameters. The equations below represent the relations (Paschotta).

$$b = \frac{2\pi w_0}{\lambda}$$

$$\theta = \frac{\lambda}{\pi w_0}$$

The alternative method utilises a sweeping Gaussian beam that creates a virtual light sheet, namely a digitally scanned light-sheet implemented in the variation digitally scanned light sheet microscopy (DSLM) (P. J. Keller & Stelzer, 2010). The sweeping effect is formed by a fast scanning galvanometer. The plane is consequently illuminated only partially at any given time, decreasing the pixel dwell time, a feature that can be synchronised with the rolling shutter of the CMOS camera to increase the sensitivity and, subsequently, the image quality (Baumgart & Kubitscheck, 2012). The laser power must be adjusted accordingly to maintain the appropriate SNR. However, compensating the reduced dwell time with the increased laser power leads to increased photobleaching due to the increased fluorophore saturation (Daetwyler & Huisken, 2016). The advantages of the digitally scanned light sheet include the ability to modify the light-sheet thickness, by means of laser diameter, as well as the light-sheet height, by means of the scanning angle via the scanning amplitude.

Both methods form a light sheet, of Gaussian profile, with a thin waist characterised by the equation above and shown in figure 4.2.3.

The detection arm is designed to attain a desired working distance in which the objective is able to gain sharp focus of the illuminated region in the sample, the focal plane. The region of sharp focus is positioned to coincide with the focal plane of the light sheet accordingly, producing a region of overlap in which only the fluorescence in this region is detected, eliminating the out-of-focus fluorescence, resulting in optical sectioning. This also extends to the point-spread functions (PSF) of the illumination and detection in that the overlap occurs at both of their focus points creating an increase in axial resolution when compared to confocal techniques (Remacha, Friedrich, Vermot, & Fahrbach, 2020). Due to the non-invasive nature of this technique, it has been employed for tracking and observing dynamical systems in live imaging, at single-cell resolution, to correlate activity patterns with neuronal populations (Ahrens, Orger, Robson, Li, & Keller, 2013).

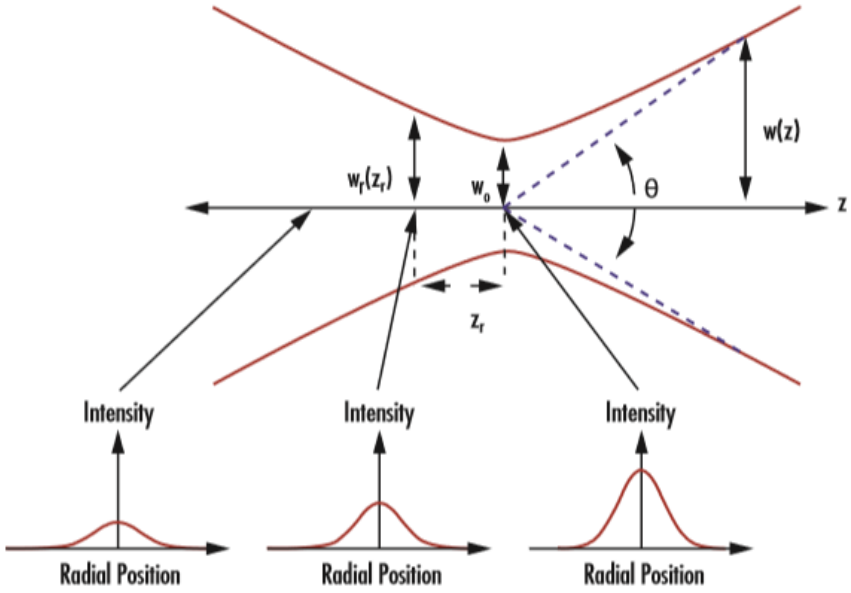

Figure 4.2.3 – Components defining the Gaussian beam waist and the respective intensities around the optimised point.

The relative intensities are compared at the different points around the beam waist, where the intensity is at its greatest. The Rayleigh length (Zr), the point from the beam waist where the cross-sectional area is doubled, is half of the confocal parameter (b) in the above equation.
Adapted from *Edmunds optics.*
From https://www.edmundoptics.com/knowledge-center/application-notes/lasers/gaussian-beam-propagation/

The need for long distance working objectives increases with large samples and optical sectioning, since there are more z-stacks to acquire. As seen previously, in order to overlap with the deep penetrating distance of the illumination plane, long working-distance objectives are required. Typically, these objectives feature low NA yet, as noted with the illumination arm, this compromises its resolving power. Long working distances are also useful when thick glass coverslips/cuvettes are present or when special housing is present during techniques, such as chemical microscopy, where environmental hazards are present and the sample must be appropriately sealed in thick housing.

Amongst the benefits of side-illumination, the technique also presents some drawbacks since the features, impurities and air bubbles within the sample, particularly optically dense samples, cause the light to be scattered, absorbed or refracted while passing through; it becomes a substantial issue within living samples in which the refractive index is,

unsurprisingly, inhomogeneous. Image quality is therefore compromised as well as the potential monitoring of biological processes during in vivo experiments. This effect has been termed 'striping' since dark lines of shadow are featured within the images and, similarly, has seen many novel techniques to confront this issue. Self-constructing beam modes emerged as a promising technique, notably the Bessel beam illumination, that propagated over longer distances without being affected by diffraction and so, maintaining the cross-section invariant (Durnin, Miceli, & Eberly, 1987). Alternatively, a multidirectional SPIM has been used as a solution in which multiple light sheets are applied in order to shine the shadows produced by a single light sheet (Huisken & Stainier, 2007). Another optical solution to tackle this problem is to pivot the light sheet through a range of angles in the detection focal plane to provide light from multiple directions to illuminate the areas affected by striping (Sancataldo et al., 2019).

4.3 Light sheet microscope variations

A great deal of modification has been seen since Voie's original establishment of the light sheet set up; each providing a somewhat different set up supported by a new acronym. Aforementioned include the dual-sided light sheet and the Bessel-beam light sheet. These adaptations tend to be classified by the objective of the imaging and the size of the sample presented for volumetric imaging.

Two-photon light sheet microscopy

Two-photon excitation (2PE) is defined when two photons are absorbed in a single quantum event where the energies combined are within the realms of that needed for single-photon excitation. Due to the absorption of double the amount of photons, the background signal is supressed. High-power is needed for this event to occur so generally a high-power femtosecond-pulsed laser is used in the near-infrared range (NIR) is used for excitation: these mode-locked pulse lasers are essential in order to achieve a high temporally-concentrated flow of photons which also must be spatially concentrated. This process can be described as 'non-linear' since the rate of occurrence depends on the second power of laser intensity. It further differs from single-photon excitation in that the excitation wavelength is longer than that of the emitted; a benefit of using infrared is that it is typically scattered less in biological tissue. This was first introduced by Maria Göppert-Mayer in 1931 as her doctoral dissertation found an alternative mechanism by which

fluorescence could be excited (Masters & So, 2004) (Denk, Strickler, & Webb, 1990) . A light sheet is then made using a two photon laser beam in order to maintain the benefits of increased penetration depth and reduced background signal whilst taking advantage of the advantages of the light sheet configuration.

Inverted selective plane illumination microscopy (iSPIM)

Inverted light sheet microscopes provide an excellent alternative for sample mounting, altering how the sample is illuminated and its position towards detection. This has been implemented for various motivations.

In toto imaging is often desired when investigating developmental processes, such as cell division and specification of cell fate. In the original set-up of the light sheet microscope, the sample is held in a narrow space in the focal plane of illumination and detection, often embedded in agarose, small capillaries or cuvettes filled with index-matching solution. This configuration isn't compatible with the study of embryo development which triggered the realisation of the inverted microscope in which samples were able to be imaged and illuminated from below while the samples are held down by the force of gravity (Strnad et al., 2016).

The need for customised sample mounting extends to larger samples, for example thick slices of the human brain. Indeed, volumetric reconstruction is often done with very thin slices of less than 100µm in thickness. However, this strategy can compromise the structural integrity of the sample, introduce artefacts as well as being time consuming. Through the use of an inverted light sheet microscope, the sample can be illuminated and detected from a 45° angle from above, in both the left and right direction, allowing for a large sample chamber below, capable of accommodating large samples and more than one. A benefit of mounting more than one sample is that the system can now be operated remotely, requiring just one session of sample mounting for many acquisition sessions. What this also provides is increased axial resolution, since more of the sample is imaged in the z-plane (Pesce et al., 2022).

Further modifying this setup has led to the creation of dual-illumination iSPIM which makes use of two orthogonal and inverted objectives that each illuminate and acquire the same sample. During the post-processing, the two images can be merged to form a resulting image that contains a broader range of spatial information, ultimately striving towards

gaining isotropic resolution (Wu et al., 2013). Since two fields of view must be illuminated, two illumination light sheets must be employed, increasing the factor by which the sample is photo-bleached.

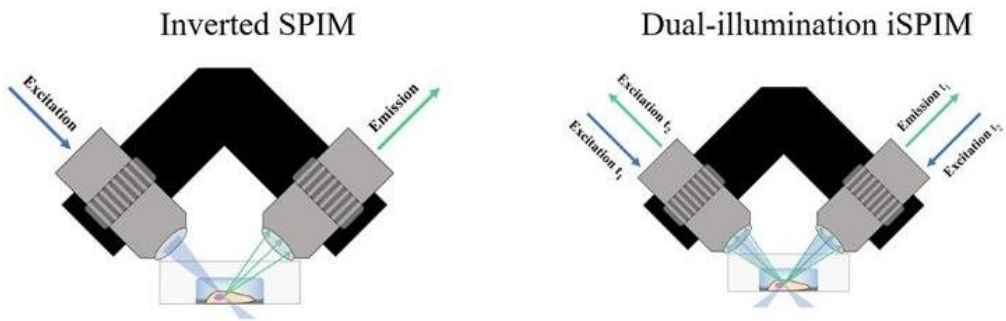

Figure 4.3 – comparison of set-up of iSPIM and Dual-iSPIM

The inverted spim is flexible and able to be modified to increase axial resolution by adding a second illumination and detection path, pushing towards isotropic resolution.
Adapted from (Albert-Smet et al., 2019)

Optical lattice light sheet

Optical lattice light-sheet designs expanded on the idea behind the Bessel beam light sheet microscope; the non-diffracting nature, propagating through y with a constant cross-sectional profile. The novel technique employs topical lattice patterns to illuminate the sample, optimised for illumination confinement as well as axial resolution. The pattern is created through the superposition of two or more plane waves, holding 2D or 3D structure, where discrete points about the annulus are illuminated. As with other light-sheet forms there exists a trade-off; in this case between the thickness of the light sheet and its length in y, the effective field of view is limited due to the confinement when limiting the annulus in z (B. C. Chen et al., 2014).

This type of image is often applied for in-vivo cellular localisations and applications requiring super resolution. Cells within the excitation band are well-held in focus, with minimal artefacts, consequently making it an ideal mode to visualise dynamic cellular interactions, specifically tracking of individual cells with a high density of molecules as large, out-of-focus signal is reduced.

Chapter 5 Expansion microscopy

5.1 The development of Expansion Microscopy

Until recently, all attempts to increase the resolution of the system had focused primarily on optical modification, manipulating refraction through magnification. Expansion microscopy (ExM) is a ground-breaking tool that increases the resolution of imaging through sample preparation alone. It is an approach which combines multiple fields together: the physics of polyelectrolyte gels capable of swelling, a phenomenon explored by groups such as that of Toyoichi Tanaka in the 1970s, along with the field of preserved biological samples being embedded in polymer hydrogels for imaging, a method led by groups such as that of Peter Hausen and Christine Dreyer in the 1980s (Wassie, Zhao, & Boyden, 2019). The technique is centralised on the idea of covalently anchoring biomolecules in fixed biological samples to a polymer network, generally through molecular handles. Once the key elements have been fixed in place, the sample is digested removing all other structures not attached to the gel while those pre-attached remain unharmed. Facilitating the physical expansion is the presence of water-absorbent polymers in the treated tissue; the fundamental principle of polyelectrolyte gels that incur swelling in volume when immersed in water (Tokita, 2022). The remaining features are either fluorescently labelled or were already fluorescent biomolecules and therefore can be imaged in their original composition by a fluorescent microscope.

The initial requisite of expansion microscopy is attaining a fixed sample. Aldehydes are commonly employed as fixatives since they permit the stabilisation of the fine structures in cells and tissues. Formaldehyde (HCHO) molecules, where the aldehyde group is the –CHP, which when dissolved in water combines to form methylene hydrate, HO-CH_2-OH. These methylene hydrate molecules combine with one another, reacting to form polymers. Higher polymers, containing many repeated units such as paraformaldehyde, are insoluble.

A solution that works optimally as a fixative contains monomeric formaldehyde, methylene hydrate, which reacts with primary amino groups such as proteins. The aldehyde group has a carbonyl carbon present which combines nucleophilically with the free electron of nitrogen in the amine groups. These then go on to react with other atoms of proteins through a methylene bride, $-CH_2-$ (Kiernan, 2000).

In 2015, a group at MIT of Chen, Boyden and Tillberg manufactured a protocol which synthesises, within a specimen, a swellable polymer network that can physically expand in an isotropic fashion by ~4.5 fold linearly in all directions (F. Chen, Tillberg, & Boyden, 2015). The polymer network was produced by utilising the expandable properties of polyelectrolyte gels infused into the biological sample. In order to preserve the structural identity of the specimen, specific labels are covalently anchored to the polymer network, as shown in figure 5.1.1. The resulting specimen, containing anchored biomolecules, is then physically enlarged, physically increasing the space between biomolecules, rendering them easier to resolve before even entering the optical system. An interesting feature of this technique is that it was able to provide a way to break through the optical diffraction limit by separating labels that are spaced closer than this diffraction limit of light through expansion.

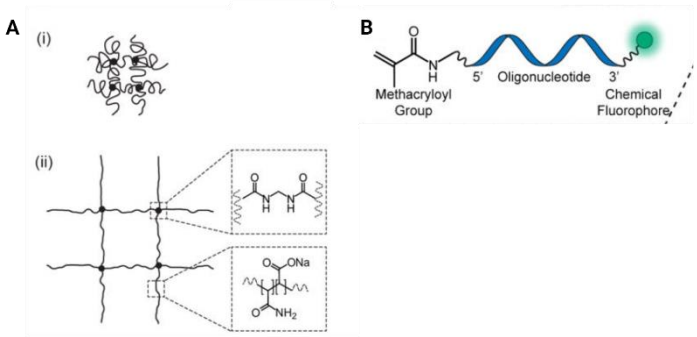

Figure 5.1.1- Concept of Expansion Microscopy

Inset (A) Schematically represents the collapse of the polyelectrolyte network with the polymer chain (line) and the crosslinker (dot) and the subsequent expanded system following dialysis with water. (B) Schematic of a fluorescent label anchored to the biomolecule.
Adapted from (F. Chen et al., 2015)

This original paper exploited the well-established property of polyelectrolyte gels in which expansion is triggered through dialysing the gel in water. This type of gel was infused into the specimen, demonstrated on mouse brain tissue, that had been first chemically fixed and permeabilized. Sodium acrylate, a monomer reagent capable of rendering a material super-absorbent, together with co-monomer acrylamide and with N-N'-methylenebisacrylamide, a crosslinking reagent formed the monomer solution. Once diffused into the tissue, the polymerisation process can be triggered via free radicals using ammonium persulfate (APD) and tetramethylethylenediamine (TEMED) as accelerators. Following this, protease treatment is applied for the purpose of homogenising the mechanical characteristics and digesting undesired biomolecules. Most fluorescent dyes are compatible with this process and are not destroyed during digestion, cyanine dyes however are mostly destroyed. At this point, the sample is in form to be expanded through dialysis in water. Since the expanded samples consist largely of water, the expanded specimen are rendered transparent and ready to be optically imaged.

Following on from this significant demonstration, many variants have appeared by other groups with developments made to support various goals. The variants continue to facilitate the imaging of biomarkers, such as proteins and RNA, in samples that have been fluorescently labelled or genetically encoded. The process is robust enough to explore a range of expansion factors through the engineering of the polymer network; indeed, the ratio the sodium acrylate and acrylamide proportions are inversely proportional to the expansion ratio (Okay & Sariisik, 2000). More than several have been produced and published, below are some examples in more detail.

ProExM (Protein retention Expansion Microscopy)

The first version of Expansion Microscopy, as described above, required labelling reagents to be synthesised by users for the targets of interest which limited the applications. ProExM, developed a year later by the same group, applied only off-the-shelf chemicals. One of these chemicals is acryloyl-X present to equip the amines on the proteins with a polymerisable carbon-carbon double bond facilitating the anchoring to the polymer gel (Tillberg et al., 2016). All proteins, including fluorescent antibodies or those that have been genetically encoded, are bound to by acryloyl-X.

During this time, another group of Chozinski developed a protocol that implemented methacrylic acid N-hydroxysuccinimidyl ester (MA-NHS) or glutaraldehyde to serve as anchors instead of acryloyl-X (Chozinski et al., 2016). Each reagent has its own benefits in

that MA-NHS is a smaller molecule so requires shorter incubation times while glutaraldehyde preserves more details however generates high background noise.

In this study, it was also shown that biotin-labelled antibodies could be used, with visualisation enabled post-expansion by application of fluorescent streptavidin, which allows for utilisation of fluorophores that would have been destroyed by the expansion process.

ProExM, conducted with any of the anchoring reagents, has been continuously validated using a broad range of fluorescent proteins, and antibodies, and applied to the imaging of proteins and structures. Some examples include keratin fibres, myelin, glial markers, chromosomes, mitochondria, pre and postsynaptic proteins, microtubules existing in different tissues and cell types (Freifeld et al., 2017).

Another protocol developed in parallel, and independently, to these protocols is the Magnified Analysis of the Proteome (MAP) which shares the same goal of retaining the epitope. To this aim, the protocol is slightly different in each step, particularly through application of hydrogel solution to the sample, conducted via transcardial perfusion. During the formaldehyde fixation step, the cross-linking between proteins is reduced through the addition of a high concentration of acrylamide which reacts to the formaldehyde bound to proteins which, in turn, blocks protein-protein crosslinking. This bound acrylamide is subsequently able to equip proteins with a moiety that can be anchored to the gel due the ability of acrylamide being able to participate in free radical polymerization which form the tissue-hydrogel network. Proteins and clearing of lipids is done at high temperatures using a detergent and the gel can finally be immersed in water to facilitate isotropic expansion. This protocol was tested on whole organs and cerebral organoids which then underwent post-clearing staining. A strong feature of this technique is that immunolabeling is performed after the clearing has been done, enhancing the scaling capabilities since signals can be amplified or reinforced following clearing. Furthermore, one is able to conduct multiple rounds of antibody de-staining and re-staining: a feature that enhances the use of a single sample (Ku et al., 2016).

Polyacrylamide gels, used in this protocol, must undergo polymerisation in an anoxic environment since oxygen is detrimental to the formation of polyacrylamide gels which form under free radical polymerisation. Inhibition of the reaction can be caused by any element or compound that traps free radicals (Chrambach, 1985). Oxygen is an example of a free radical trap. Oxygen can penetrate through the sample, and inhibit polymerization if

present in the surrounding air or dissolved into solutions. It is reported that oxygen reacts very rapidly with carbon-centred radicals which go on to form peroxyl radicals. These peroxyl radicals do not readily react with alkenic double bonds of the acrylate monomers which prevents the polymerization process. The degassing process is therefore a critical step.

Temperature is also a critical factor in the acrylamide polymerisation process since it is an exothermic reaction; the heat generated in turn encourages the rate of the reaction. The process of polymerization accordingly occurs rapidly once begun.

After some inconsistent immunolabeling results, the Chung lab that had produced the MAP protocol, released an updated version of the protocol in 2021. The articles addressed the issues and the corresponding hypothesis that were present in the MAP protocol in that fluorophore-bound antibodies were being prevented from binding to the epitope in the target. Endogenous proteins containing amines react with formaldehyde and, subsequently, acrylamide, potentially creating long polymer chains lining the epitope of the target. This process can physically block antibody-epitope interactions when conducting immunofluorescence. Furthermore, the tethering of these acrylic monomers to the epitope site can create alterations in the weak interactions that play an essential role in the antibody bonding process. As a result, the newer protocol aims to conserve the epitope site and is appropriately termed Epitope preserving Magnified Analysis of the Proteome (eMAP) (Park et al., 2021). Instead, eMAP begins with formaldehyde-fixed samples that are thoroughly washed to remove excess formaldehyde and in the absence of formaldehyde, acrylic monomers cannot react with endogenous biomolecules. What this means is that the chemical tethering of biomolecules to the gel cannot happen but rather, the gel physically traps the biomolecules by physically linking them in a tissue-gel hybridization, as shown in figure 5.1.2. The end result minimises the loss of antigenicity to optimise immunofluorescence with the expansion microscopy technique. Indeed, the ability to use formaldehyde-fixed samples renders this improved technique more feasible since transcardial perfusion with complex solutions, as in the original MAP paper, can be problematic and less prone to success.

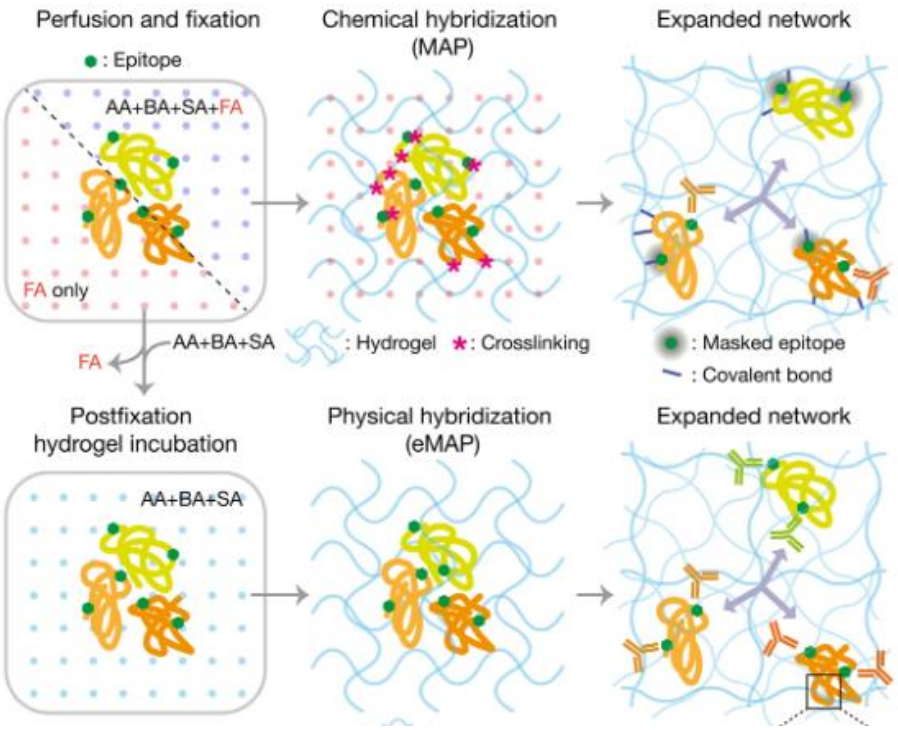

Figure 5.1.2 – Schematics comparison of hydrogel procedure in MAP and eMAP

MAP creates a chemical bond between the biomolecules and the hydrogel through the presence of formaldehyde leading to long unwanted acrylamide chains that have the potential to mask the epitope. eMAP avoids this potential occurrence by omitting formaldehyde from the process, instead physically entangling the biomolecules to the hydrogel.
Adapted from (Park et al., 2021)

Iterative Expansion microscope (iExM)

The expansion factor of expansion microscopy has been pushed to its expandable limits through the development of iterative expansion microscopy; a sample already expanded is then treated with a second gel that is synthesised again within the sample in order to be further expanded (Chang et al., 2017). The two gels are chemically different; in the first

step a chemically cleavable crosslinker is included so that, when the second gel is added, the first can be cleaved. No spatial information is lost in this process as the biomolecules of interest are thereafter transferred from the first gel to the second. Expansion factors have achieved ranges of up to ~20-fold with an effective resolution of ~25 nm producing resolved images of the geometric organisation of pre- and post-synaptic proteins, as shown figure 5.1.3, of the neurotransmitter receptors and scaffolding proteins within the synapses. Fluorescent labels can be added before the first gel is added to ensure the chemical anchoring of these markers.

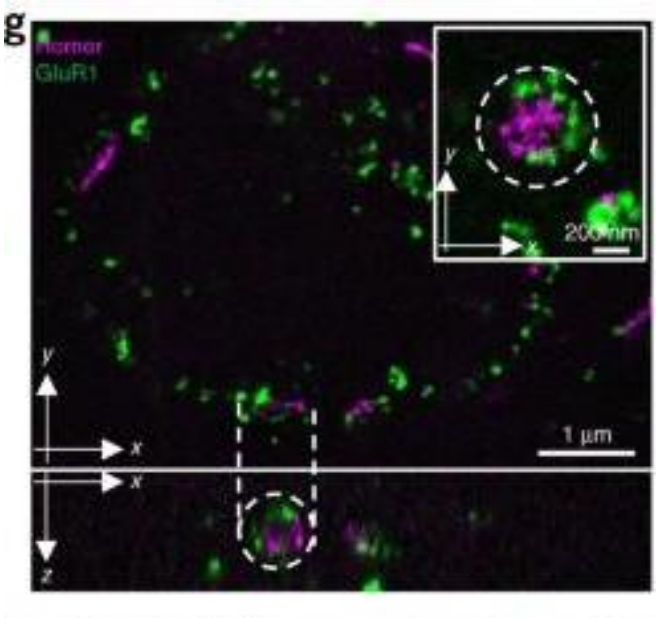

Figure 5.1.3 – Synaptic protein

Cultured hippocampal neurons prepared with 20-fold expansion with labelled Homer1 (magenta) and Glutamate receptor 1 (green)
Adapted from (Chang et al., 2017)

Digesting buffer with Proteinase-K of clearing solution with SDS

The varying techniques employ varying methods to render the tissue transparent. In the review above, the original expansion microscopy paper approaches this using a digestion buffer containing Proteinase-K. More recent papers, such as the original MAP paper use a softer method that utilises the clearing capabilities of Sodium dodecyl sulphate (SDS).

The two sample preparation techniques use differing solutions to render the tissue transparent. While eMAP strives to preserve the entire proteome, allowing for post-digestion immunolabeling and therefore must avoid complete protein digestion, classical ExM uses a much harsher method. Sodium dodecyl sulphate (SDS) which is known to denature some, but not all, native proteins. SDS disrupts the tertiary structure of proteins, unfolding them into a linear molecule. SDS coats the protein linearly, coating the protein in negative charges which mask the intrinsic charges present on the amino acid groups of the protein. This separation of proteins is based upon the individual molecular weight.

Being able to remain active in harsh conditions such as a varying pH range, enzyme Proteinase-K is very useful in digesting all proteins and nucleases which are not molecularly anchored to the tissue-hydrogel matrix. In the presence of protein-denaturing chelating agents, in this case EDTA, the enzyme is activated, destroying proteins in cell lysates.

5.2 Limitations of expansion microscopy

Although this technique can be adapted to suit the goal of the project, it holds some limitations. Each step must be completed correctly in order to achieve a transparent and isotopically enlarged sample. Indeed, when working with large samples such as entire organs, the length of time required for incubation steps increases exponentially. In some cases, errors may only be evidently presented during the final steps and therefore not able to be corrected. This potentially causes distorted images or samples no longer useful, a loss of time and resources.

To add to this, expansion microscopy can be temperamental with some fluorophores since they can be bleached during high temperatures in the process which effectively renders the specimen unusable since the signal would be missing. Some are fairly reliable, for example Alexa 488 and Atto 565, yet they are still subject to losing their efficacy throughout the process by around 50%. Each time more signal amplification is needed, the specimen becomes costlier and time consuming, limiting its feasibility for implementation in standard laboratories.

5.3 Light sheet fluorescence expansion microscopy (ExLSM)

LSFM and ExM go hand in hand for imaging the structural composition of biological samples. The flexible nature of the LS microscope design provides grounds for customisation around the samples and avoiding the requirement to cut into slices the tissue under study.

Resolution can be optimised both optically and within the sample itself while the transparent samples permits the optical sectioning by the illumination light to image the sample slice-by-slice while intact since the photons in the illumination plane are able to pass through the sample to reach detection.

Perhaps an obvious limitation to this is the increased data field, generating longer sample preparation times, longer acquisition times and larger amounts of data generated. After establishing these techniques, work continues to be done in order to optimise the shortcomings while considering trade-offs between resolution and imaging time with data volume.

Part 2 The development of Expansion Microscopy techniques for large biological samples

Chapter 6 Methods and Materials

6.1 Mice

Brains from both male and female FosTRAP mice (B6.129(Cg)-Fostm1.1(cre/ERT2)Luo/J × B6.CgGt(ROSA)26Sortm9(CAG-tdTomato)Hze/J) were used in this study (Guenthner, Miyamichi, Yang, Heller, & Luo, 2013). Prior to perfusion/scarification they were housed in groups where they received water and food ab libitum. They lived as 'social animals', free to behave freely while maintained in a controlled environment of light and dark cycles, each of 12 hours (light starts at 7:00 am), with a temperature of 22 ± 2 °C and humidity of 55 ± 10 %. The adult mice, between 3-6 months old, were grouped in cages of 2-3 mice.

Brains from both male and female mice injected with an adeno-associated virus that carries the tdTomato gene under the Synapsin promoter, AAV8 hSyn-tdTomato. The injections were performed in the nucleus reuniens, Thalamus region, so that long-range projections of neurons originating in the Thalamus were labelled brightly with tdTomato fluorescent protein.

All experimental procedures were approved by the Italian Ministry of Health (Authorization n. 512-2018_FC) and conducted according to principles of the 3Rs.

6.2 Perfusion and Fixation

Mice underwent deep anaesthesia of isoflurane solution (1.5% - 2%) and Transcardial perfused using 50mL of chilled 0.01 M phosphate buffer solution (PBS), pH 7.6, proceeding 75mL of paraformaldehyde (PFA) solution, 4% (wt/ vol), pH 7.6. The brains were extracted and then incubated in the same 4% PFA-PBS solution at 4 °C overnight, then washed with PBS with 0.02% sodium azide and finally stored in this solution until used. The brains were used from a time frame of immediately to a maximum of a few months.

6.3 eMAP (Epitope-preserving Magnified Analysis of the Proteome) protocol optimised and adapted for large samples

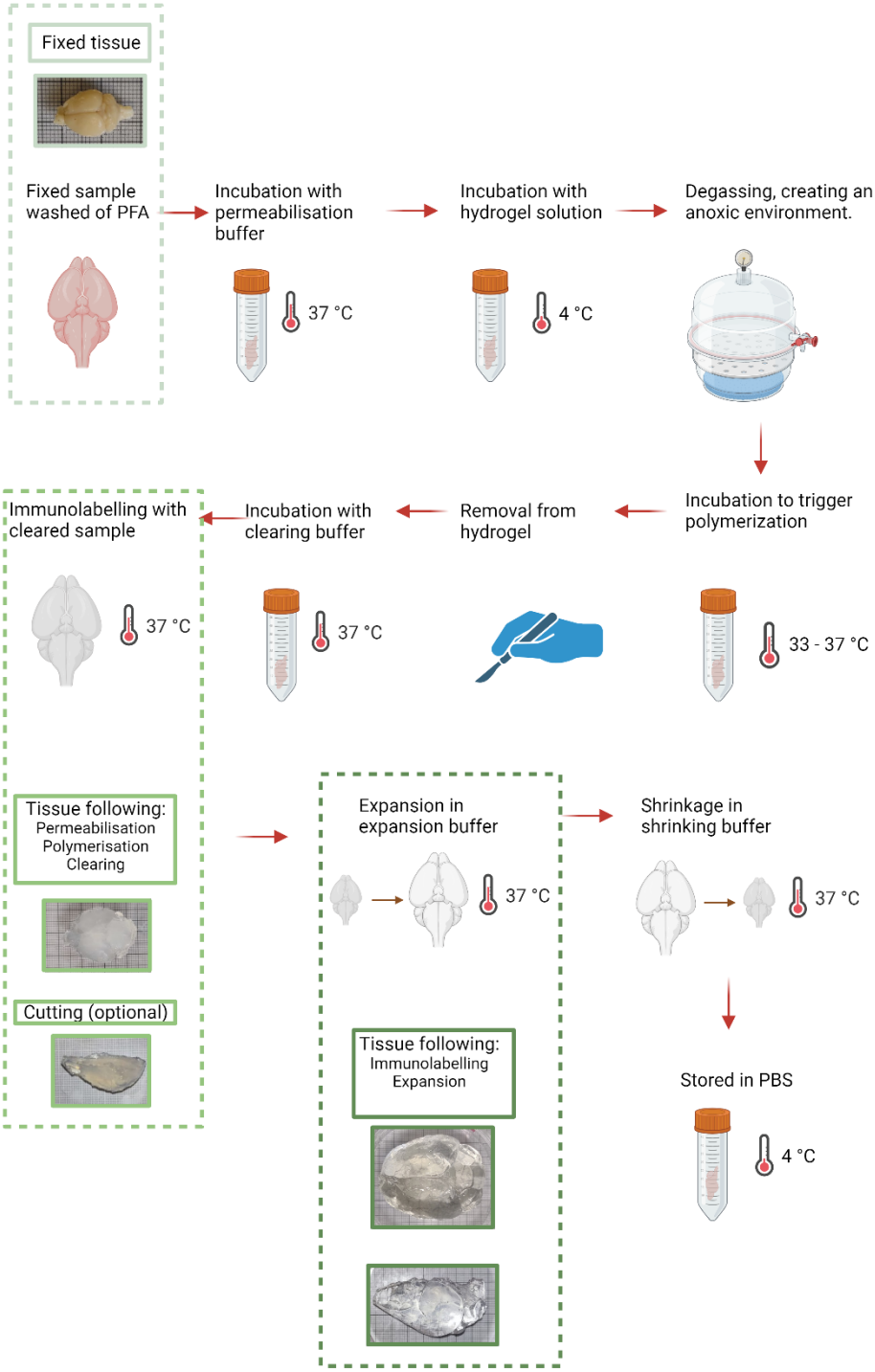

Figure 6.3.1 Schematic representation of the adapted eMAP protocol

Each step is provided with relevant temperature incubation along with insets of expected sample at stages throughout the protocol. Information regarding incubation times and solution compositions are discussed in more details below in this chapter.

Required solutions

Permeabilisation buffer

Chemical	Concentration
Triton X-100	5% (w/v)
Sodium azide	0.02% (w/v)
PBS	

eMAP Hydrogel solution

Chemical	Concentration
Acrylamide	30% (w/v)
Bis-acrylamide	0.1% (w/v)
Sodium acrylate	10% (w/v)
VA-044	0.03% (w/v)
PBS	

Clearing solution (Titrated to pH 7.4)

Chemical	Concentration
Sodium dodecyl sulfate	6% (w/v)
Phosphate buffer	0.1 M
Sodium sulphite	50 mM
Sodium azide	0.02% (w/v)
DI water	

Expansion buffer

0.01x PBS or simply DI water

Before starting the procedure, the samples are measured in order to have preliminary data for having an initial idea of the expansion factor. Images below, shown in figure 6.3.2, are examples of the different cuts of brain tissue used.

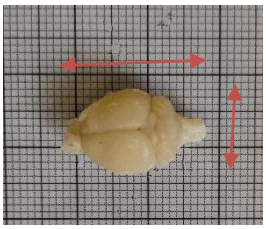

Figure 6.3.2. Sample is measured prior to beginning treatment

Orange arrows indicate the axes in which measurements were taken, on a whole mouse brain, in order to calculate the final expansion factor upon expansion.

Fixed tissue samples initially underwent permeabilisation to facilitate easier transport of molecules through the tissue. This is both useful for hydrogel embedding, as well as the ensuing immunofluorescence which uses antibodies/molecules of larger dimensions. The permeabilisation removes some cellular membrane lipids which ultimately allow the passing of large molecules inside the sample. Different permeabilisation buffers were tested in order to fulfil the permeabilisation that are in the table below. All buffers were tested on mouse brain tissue and incubation time is dependent on the buffer itself. Using PBST as a buffer was investigated in order to provide flexibility when choosing a permeabilisation buffer.

	PBST x1	*PBST x5*	*CHAPS buffer 10% in 1x PBS*
Full brain	Incubated from perfusion and fixation until use (several weeks)	2 days	2 days
¼ - ½ brain	Incubated from perfusion and fixation until use (several weeks)	1 day	1 day

The permeabilised fixed brain samples were washed several times over a full day period, recommended also overnight for full organs, and then incubated in the eMAP hydrogel gel monomer solution as per the original protocol – 30% acrylamide (w/v), 10% sodium acrylate (w/v), 0.1% bis-acrylamide and 0.03% VA-044 (w/v) (Park et al., 2021). The solution was freshly made directly before incubation due to the longevity of incubation time for large samples, in order to reduce light or heat exposure. Light exposure and thawing can compromise the polymerization process and thus lead to homogeneity in samples. The solution should be light-protected during the preparation and storage process. Due to the sensibility when measuring small quantities, the initiator quantity can be difficult to precisely measure. To overcome this, the initiator solution can first be made into a stock solution of 10% in order to weigh more precisely a larger quantity and later added to the eMAP solution, taking the final concentration into consideration. Alternatively, the solution can also be frozen though the monomer solution and initiator stock solution should be stored and frozen separately at -20 °C before use, though light and heat exposure must be kept to a minimum during the storage.

Sodium acrylate can be of inconsistent qualities which consequently affects the quality of the eMAP procedure. This becomes evident during the preparation of the monomer solution in which the solution never reaches a state of full transparency but instead a tainted yellowish colour, oily phase separation or possibly the presence of black particles due to impurity. A control to check this is to add the sodium acrylate to DI water, allow it to mix and if one or all of these effects occurs, the quality has been compromised. After trials from different suppliers, the sodium acrylate from AK Scientific, Inc. USA was found to provide the best quality.

Incubation takes place at a temperature of 4 °C in order to allow the monomer solution to penetrate through the entire sample without beginning the polymerization process initiated by the VA-044 initiator. At 4 °C, the initiator isn't reactive and so the polymerization process won't begin. VA-044 is a type of compound known as an azo polymerization initiator, characterised by the azo group (R-N=N-R') which forms carbon radical when decomposed due to light or heat exposure. This carbon radical initiates free radical polymerization of the monomers to create the polymer gel. Each step must take place sheltered from light.

Diffusion is a process which occurs rapidly over very short distances yet becomes increasingly longer over longer distances. Indeed, this is a great consideration when working with large samples; the whole mouse brain. The time (t), in seconds, required for

diffusion is given by the approximation of the Fick's second law for diffusion time calculation (Atkins, P.W, Physical Chemistry, 5th ed., Freeman, 1994, 104-108):

$$t \approx \frac{d^2}{D}$$

Where d is the distance in metres that must be diffused through and D represents the diffusion coefficient (m^2/s). This means an incubation time must be squared proportionally to the radius of the sample, the distance of diffusion to the centre of the sample. Since initial trials with 1mm brain slices were successfully embedded with overnight incubation (~16 hours), a preliminary calculation using the relation was used as a guidance, resulting in a 10-day incubation for tissues from ¼ brain and upwards. Since the shortest diffusion distance of a whole mouse brain is the dorso-ventral axis, with an average length of 8.5mm, the shortest diffusion distance necessary to reach the centre was theorised to be ~4.25mm.

Once the moment solution has effectively penetrated the tissue volume, the samples were incubated at a higher temperature, 33 – 37 °C, to trigger the polymerisation process. Lower temperature was employed for larger samples to account for the exothermic nature of this gelation step. At a lower temperature, the polymerization process takes longer to trigger meaning this must be optimised depending on the volume and size of the sample. In general, overnight incubation at 35-6°C is necessary for a ¼ - full brain since both are placed in a 50ml conical tube filled with eMAP hydrogel. This process of polymerization/gelation must take place in an oxygen-deprived environment. To meet this goal, the samples are first placed in a degassing chamber, with the conical tube lids slightly ajar, where oxygen is removed through vacuuming before an influx of nitrogen is added. The conical tubes are then quickly closed tightly to prevent oxygen entering and then placed in the appropriate incubation tank to polymerize. In case a degassing chamber isn't available, an influx of argon is an appropriate alternative yet not completely reliable. A conical tube with the sample and hydrogel solution should be exposed to a positive influx of argon gas for 1 minute. The density of argon is much higher than that of air allowing for it to eventually replace the air remaining inside the conical tube. Once satisfied that the conical tube is filled with argon, the top can be sealed and incubation can begin. There remains a risk that oxygen present in the air remains in the conical tube deeming this alternative to not be on par with the prior.

Following gelation, the hydrogel was removed from the conical tube before removing all excess gel from around the brain sample. Here, the gel is soft enough to be easily removed from the tissue-gel hybrid surface causing minimal disturbance. When working with smaller pieces, this can be more challenging as surfaces are more scabrous; the brain intact tends to be easier to remove due to being equable. This is an important step, which can be done at other points before expansion, since the pure gel has a lower expansion rate than the tissue-gel hybrid and thus, restricting the tissue expansion. Gel should be removed at any possible step since the gel tends to have an affinity to some antibodies used during immunolabeling. The tissue-gel hybrid was then incubated in PBS at 37 °C overnight for hydration for all large samples from ¼ brain and larger due to diffusion time during which the sample expands linearly around 2.5x linearly, up to 2x depending on incubation time. Should it be necessary, the sample can be cut here, before denaturation. The hydration step is necessary for gel-embedded samples prior to clearing.

The tissue-gel samples were then ready to begin the denaturing process which works to remove the lipids in the cell membranes, improving the optical transparency as well as macromolecule permeability. The denaturing solution is made up of sodium dodecyl sulphate (SDS) which serves to dissociate and solubilise protein complexes by forming negatively-charged SDS-protein complexes. This cleaves the non-covalent bonds between the protein chains breaking hydrophobic interaction and hydrogen bonds, all the while not affecting the disulphide bridges (Schmid, Prinz, Stäbler, & Sängerlaub, 2017). The digestion buffer also contains sodium sulphite which serves to reduce chemical crosslinking. By concentration, the denaturing solution consists of 6% SDS (w/v), 50mM sodium sulphite and 0.02% sodium azide (w/v) titrated to a pH of 7.4. Conducted at 37 °C, the solution was preheated to which then the samples are added and subsequently incubated at constant shaking; for a full brain, the time taken usually was around 3 weeks with the solution changed every few days yet this is dependent on the sample itself; the process should be followed until the sample is cleared of lipids. If endogenous fluorescence is not desired in the final step, this temperature can be increased to speed up the process otherwise 37 °C must not be exceeded. Again, this step can cause an expansion which is important to keep in mind when selecting the container. In order to gage whether denaturing was completed, the sample was inspected on millimetre paper with the aim of being totally translucent without any opaque regions, as shown before in figure 6.3.1 The sample have total transparency once expanded, prior to expansion the sample should be transparent but there is a slight opaqueness.

The fully-cleared sample was then thoroughly washed, recommended at least 5 times over a 24-hour period at 37°C. SDS is a very useful component for clearing and expansion; however large detergent micelles tend to get stuck within the sample, thereafter leading to unsuccessful antibody staining. Several washes are conducted over a two-day period using PBST, with 0.02% (w/v) sodium azide, at a higher percentage of triton with at least five solution changes. Alternatively, a non-ionic surfactant C12E10 has been known to effectively clear out SDS leading to improved staining afterwards. With peak activity at 60°C, a short incubation here of an hour followed by multiple washes at 37°C is equally as effective. Any excess gel can be removed continuously if present during this step, since it is more soft, the gel can be easily removed.

Immunolabeling was thus able to be performed. Considering uniform labelling, this step must be optimised around the sample in question, in this case the full brain or large tissue pieces. Samples were incubated in conical tubes with enough solution to completely cover the samples. Standard concentrations of 1:500, both for primary and secondary antibodies in PBST, adequately labelled the thick samples. The increased number of antigens and already slight tissue expansion were considered in both the concentration and incubation time for labelling. Since the expansion ratio is approximately 4-fold, the dilution of the signal is also expected by 64-fold therefore high labelling density is necessary. The samples were incubated at 37 °C with gentle shaking for around 15-17 days for 1⁄4 - ½ brain samples while a full brain was incubated in the same concentrations for a minimum of 3 weeks. Prior to adding secondary antibodies, the samples were washed over a 2-day period with multiple solution changes with PBST at 37 °C to clear out any unbound primary antibodies, avoiding the mis-detection of bound fluorophores.

Once immunolabeling was concluded, the samples were ready for expansion. In order to achieve maximum expansion, the samples were incubated in the expansion buffer, DI water, with shaking at 37°C for 2 days, changing the DI water at regular intervals. The samples linearly expanded in all directions by ~4-fold. Images shown in figure 6.3.1 show the transparency and growth of the tissue volumes.

The level of expansion can be controlled by selectively choosing the expansion solution, for example varying concentrations of PBS induced a lower expansion factor. The benefit of using low-concentration PBS (0.01x) is that it creates a more stable environment for antibodies while DI water can cause antibodies to slowly dissociate over time, certainly problematic in long imaging sessions typical of large samples. Samples prior to expansion, or those that had been shrunk, required an index matching solution different from that of

the PBS solution. This could be due to the contribution of the tissue in the tissue-gel hybrid altering slightly the RI, as explained by the Lorentz-Lorenz equation (Ueda, Dodt, et al., 2020). Varying concentrations of 2,2 - thiodiethanol (TDE) were used to match the RI of the sample in a marginally less expanded state before imaging and to achieve osmotic pressure to render the sample in a stable state for imaging. A 68% TDE solution was incubated with the sample overnight to allow diffusion, this could be imaged in a 91% glycerol solution to achieve imaging of the whole sample in a shorter time frame than when totally expanded. This step must be done with samples pre-expanded or shrunk back to this state since putting an expanded sample directly in TDE will cause the concentration of TDE as a refractive index matching solution to change and therefore be inaccurate. This also allows the user to find the areas of fluorescence which can then be imaged in an expanded state and therefore at higher resolution; a process known as hierarchical imaging (Wacker et al., 2016).

The expansion factor was measured initially by measuring each axis of the brain before and after expansion in order to have an estimated value of the expansion factor. This can be further measured upon analysis of images pre- and post- expansion.

Finally, after imaging, the samples were shrunk in PBST at 37°C and maintained in this state for storage. The shrinkage step takes less time than that of the expansion step which can be troublesome in larger, thick samples. The fast shrinkage process can cause inhomogeneous shrinkage amongst the tissue regions, creating cracks and even breakage. In order to prevent this, the sample was shrunk in multiple steps using serial dilutions of the shrinkage solution, PBST. If left expanded in the expansion buffer, the samples lose structural integrity after 8-10 days. For long term use, samples are best preserved in PBS at 4°C.

6.4 Expansion Microscopy (ExM) scaled and optimised for large samples

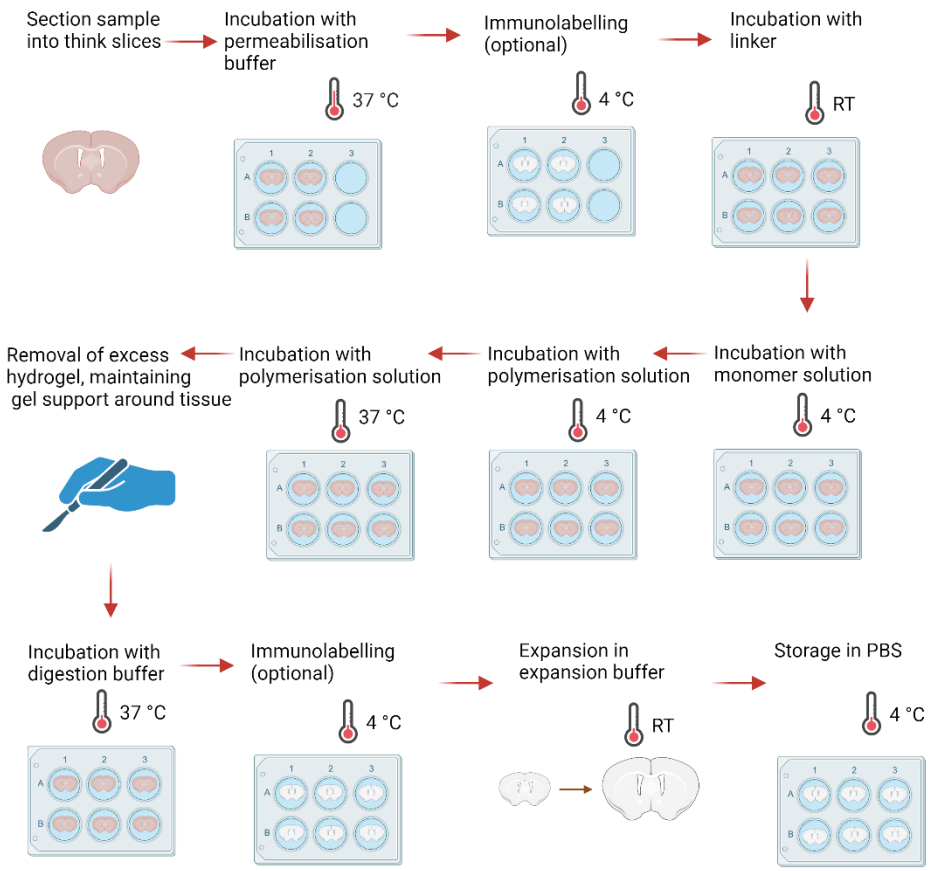

Figure 6.4.1 Schematic representation of the adapted ExM protocol

Each step is provided with relevant temperature incubation along with insets of expected samples at stages throughout the protocol. Information regarding incubation times and solution compositions are discussed in more details below in this chapter.

Required solutions

Linking

1M MA-NHS in dimethyl sulfoxide.

Monomer solution

Chemical	Concentration
Sodium acrylate	8.6%
Acrylamide	2.5%
N,N'-Methylenebisacrylamide	0.15%
Sodium Chloride	11.7%
PBS	

Digestion buffer (titrated to pH 8)

Chemical	Concentration
Tris	0.6057 g
Ethylenediaminetetraacetic acid (EDTA)	0.0372 g
Triton X-100	500 µl
Guanidinium	7.6424 g
DI water	96 mL

An alternative tissue clearing and expansion technique was a protocol from Rodrigues et al. here scaled and modified for large samples (Rodriguez-Gatica et al., 2022). A benefit of this technique is that endogenous fluorescence is preserved with a key drawback being the long clearing time and an output of extremely delicate samples rendering sample handling and mounting difficult.

The fixed, large tissue volumes of up to ¼ of a brain, underwent permeabilisation which effectively punctures the cell membrane, facilitating the detection of intracellular antigens by a primary antibody since entering the cell membrane is now possible. The permeabilisation buffer is made using the detergent CHAPS, rather than Triton X, a procedure first described by Zhao et al in which renders the sample more deeply and

efficiently permeabilized due to the smaller micelle size of CHAPS (S. Zhao et al., 2020). This effectively preserved the autofluorescent proteins as well as providing a clearer path for the penetration of many commercial antibodies to reach their target sites, producing full-sample staining. In order to optimise time, a higher concentration of CHAPS was used for overnight incubation to achieve full permeabilization. The samples were incubated at 37 °C with constant shaking, overnight being sufficient for slices of 2mm while at least 48 hours for ¼ brain. Without full permeabilsation, samples need longer subsequent steps.

Following a thorough washing of the samples over a 24-hour period at RT with constant shaking, allowing the full penetration of PBS to clean the innermost parts, the samples were able to undergo linking. The linking solution serves to chemically anchor fluorescently-labelled structures to a fixed point. The selected linker for this protocol is methyl acrylic acid-NHS (MA-NHS) (Sigma-Aldrich) as it is generally a smaller molecule than other linkers leading to reduced incubation times. MA-NHS also leads to a moderately low background contribution. It works by coupling protein residues, by that means, creating a polyacrylamide gel within the tissue; a protein residue is an individual amino acid that is liked in a polypeptide chain, a protein chain, in which the amino acids are linked by peptide bonds. The methylene bridge formed provides a basis for the subsequent linking between biomolecules and the polymer matrix. Concentrated at 2mM MA-NHS in PBST, samples of 2mm thickness were sufficiently incubated for 24 hours at RT, while ¼ brain for 48 hours.

Now the sample could readily be immersed in the monomer solution. This incubation is first done without the initiator reagents to allow the diffusion of the monomer solution into the centre. If the monomer solution doesn't reach the centre, those areas will disintegrate during digestion. The monomer solution is made using 8.6% sodium acrylate (Sigma), 2.5% acrylamide (Sigma-Aldrich), 0.15% N,N'-methylenebisacrylamide (Sigma) and 11.7% NaCl in 1x PBS (Carl Roth GmbH) at 4°C with constant shaking encouraging the penetration and in turn, the linking of the polyacrylamide matrix. The incubation for large samples was 24-48 hours depending on the size ranging from a quarter of the brain to a whole brain.

The complete gelling solution is made using an initiator, ammonium persulphate (APS) (Sigma-Aldrich), serving as a source of free radicals to polymerize the monomers. This is accompanied by tetramethylenediamine (TEMED) (Sigma), which further catalyses the polymerization process by accelerating the rate at which free radicals are formed (Menter & Drive, 2000). Finally, an inhibitor is added, tetramethylpiperidin-1-oxyl (4-hydroxy-TEMPO) (Sigma-Aldrich) which is particularly useful when working with larger samples

since it sets out to decrease the rate of polymer chain reaction allowing the gelling solution to have time to diffuse totally through the sample before polymerizing (Maafa, 2023). By composition, the gelling solution consists of 0.01% 4-hydroxy-TEMPO, 0.2% TEMED and 0.2% APS in the monomer solution. Prepared freshly over ice to avoid triggering the reaction, the samples were incubated for a couple of hours for 2mm samples and overnight for ¼ brain samples.at 4°C with constant shaking to permit the penetration of the sample before triggering the reaction. From here, the samples were transferred to a 37 °C incubator to trigger the polymerization process which takes around 2-3 hours until the gel is fully polymerized; this can be seen by eye and is dependent on the amount of gel surrounding each sample. Each of these steps is conducted in a wet, closed container to avoid the dehydration of the gel and, potentially, affecting the sample.

Since large samples need to be incubated with a fair volume of the gelling solution, gel can be trimmed but it was found that keeping a solid volume of gel around the sample helped in sample handling since this protocol renders the tissue very soft therefore having a supporting gel frame helps to avoid compromising the structural integrity of the sample. Following from here, the sample could be immersed in the digestion buffer in order to be mechanically homogenised through the digestion of lipids and un-anchored proteins. The digestion buffer is a solution based on Tris (Carl Roth GmbH) and ethylenediaminetetraacetic acid (EDTA) (Carl Roth GmbH) to solubilise nucleic acids while protecting the denaturing proteins; Tris, specifically, buffers the pH and protease inhibiting EDTA safeguards the integrity of the anchored proteins. Triton-X100 (Sigma-Aldrich) contributes the lysis of the tissue to break down the cell membranes in combination with Proteinase-K (New England BioLabs) that breaks down peptide bonds linking the proteins by enzymatically cleaving the links between the amino acid groups. The final concentration of the components is 50mM Tris, 1 mM EDTA, 0.5% Triton-X100, 0.8M guanidine HCl, and 18 U/mL of proteinase- K, titrated to pH 8. Incubation took place at 37 °C in which the digestion buffer was changed every 24 hours; for larger samples, this was extended to every 48 days, for samples of ¼ mouse brain dimensions, and double the concentration of the enzyme Proteinase-K in order to give enough time for sample penetration and also with enough enzyme to digest the tissue volume. The samples were continuously incubated at 37°C in a totally sealed, wet container. For example, if a sample is in a well-plate, it should be placed in a container over a damp tissue with the lid slightly ajar; the container can then be tightly sealed with paraffin. It is essential that full digestion takes place in that no unwanted biomolecules are still attached to the gel matrix. In the latter case, the

homogenous elastic properties of the gel cannot be fully employed otherwise which would render the expansion of the gel anisotropic with deformations.

Nuclear staining of 1:2000 Hoechst (Invitrogen) in order to measure the antibody penetration as a guide for optimising incubation steps. Endogenous fluorescence of GFP and tdTomato was present in the samples used.

The resulting, immunolabeled sample was now expanded through immersion in an expansion buffer. Expansion by PBS solution led to an expansion factor of 1.5, while DI water results in approximately a 4-fold isotropic expansion when compared to the original sample. In order to confirm the expansion factors and measures of homogeneity. The expansion factor was first estimated by measuring each axis of the sample pre- and post-expansion and then a more precise value is measured through imaging by identifying common features in pre- and post-expansion images to quantify the scale in which the features have moved away from each other.

6.5 Imaging modalities

Analysis of samples conducted both pre- and post-expansion was conducted in order to assess the effects of the expansion on the sample. To this aim, two systems were implemented to appropriately image the sample in its given state.

A custom-built light-sheet microscope, described in detail in Part 3 of this thesis work, accommodates an expanded mouse brain of orders up to expansion factor 5. In brief, the system features dual-sided illumination forming a light sheet at the centre of a large imaging chamber through which the sample moves through via motorised translation stages mounted above the optical table (L-509.40SD00 Precision linear stage, Physik Instrumente). The custom-built chamber ensured adequate space for the large sample to be moved in each direction in order to acquire the expanded brain at full-expansion capacity. The light sheet was generated using a dual-axis galvanometric mirror (Thorlabs GVS202), serving also to focus the light sheet where the illumination beam waist is aligned with the working distance of the objective, the illumination-detection plane. Attributing a 4f system in a telescope configuration, the illumination path was raised in order to reach the required illumination entrance height of the imaging chamber. Adequate laser beams were implemented (details corresponding to secondary antibodies and targets) that were

expanded and collimated in order to achieve the desired beam waist after traversing the optical path to the sample chamber. Utilising a long working distance objective (Olympus XLFLUOR, 4x, 0.28 NA, WD 29mm), fluorescence emission was detected from the illuminated plane in the sample, following which it was filtered using adequate band-pass filters (check filter and check secondary antibodies to include and subsequently focused by a tube lens (details) to reach the sensor of an sCMOS camera (Hamamatsu Photonics, Orca Flash 4.0, Japan). Running in light-sheet mode, confocal line detection was implemented.

Pre-expanded samples were imaged in a second custom-built confocal light-sheet microscope designed to image cleared mouse brains of varying refractive index matching solution, scheme of optical set-up shown in figure 6.5 and described in full details in (Müllenbroich et al., 2015). Concisely, the dual-sided illumination and detection featuring two sCMOS cameras, can be used to implement double-channel illumination, thus acquiring two features at the same time. Four laser wavelengths create the four possible illumination channels, which are each expanded from the sources, collimated and aligned along the optical path. An acousto-optical tunable filter (AOTFnC- 400.650- TN, AA Opto-Electronic, France) was implemented in order to adjust the power of each laser line delivered to the sample. The digitally-scanned light sheet was formed using a galvanometric mirror (6220H, Cambridge Technology, United States), proceeding a 4f system and the illumination objective lens (Plan Fluor EPI, 10x, 0.3 NA, WD 17.5mm, Nikon, Japan). The light sheet is formed at the centre of a custom-built imaging chamber able to hold and drain the varying refractive-index matching solutions. The sample is mounted above and able to be translated through the light sheet using motorised stages (C-863.11, M-112, M-116 Physik Instrumente, Germany), allowing each segmentation to be illuminated. The specialised immersion objective (XLPLN10XSVMP, 10x, 0.6NA, WD 8 MM, Olympus, Japan) was built into the imaging chamber through which fluorescence emission was collected. The emission was appropriately filtered using bandpass-filters (Semrock FF01-609/54, FF01-676/37 check which was used for our samples and give details on secondary) before being focused by a tube lens (focal length 180 mm) on to the sensor of an sCMOS camera (Hamamatsu Photonics, Orca Flash 4.0, Japan. Confocal line detection was used as the camera ran in light-sheet mode.

In the plane of x and y, optical resolution was measured at 1.35 µm and 8.6 µm in the axial, z-axis. Image stacks are acquired in a grid-form where each stack is partially overlapping in order to be aligned and stitched using ZetaStitcher (https://lensbiophotonics.github.io/ZetaStitcher/)

Both systems were controlled by a customised software, SPIMlab, details of which can be found in Chapter 8.6 of this thesis, written in LabVIEW (National Instruments, United States).

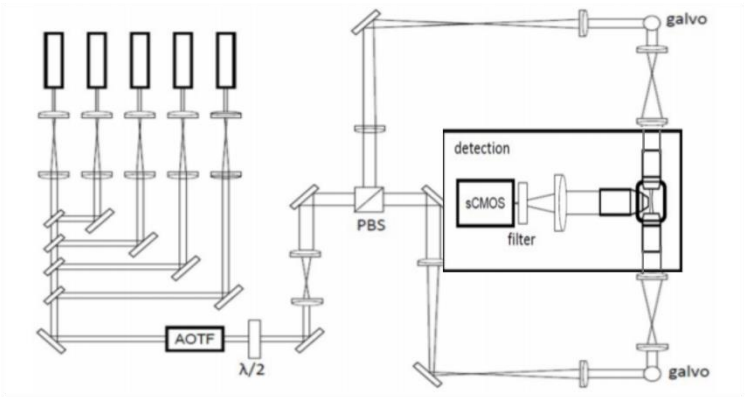

Figure 6.5 Schematic representation of the custom-made light-sheet microscope with dual-sided illumination.

Five laser lines are multiplexed into a shared beam after being expanded to the same beam diameter. An AOTF (acousto-optical tunable filter) is used to control laser channel propagation as well as regulation of power. The double-sided light-sheet illumination is generated by rapid scanning of the beams by galvanometric mirrors placed in the excitation arm of the two identical paths featuring selected input polarisation using a half-wave plate (λ/2) in combination with a polarisation beam splitter. The inset highlights the detection path where a specialised, direct immersion objective is implemented for high-RI media and an sCMOS in a wide-field configuration.
Adapted from (Müllenbroich et al., 2015)

Chapter 7 Expansion Microscopy results

7.1 Permeabilisation

eMAP (Epitope-preserving Magnified Analysis of the Proteome) protocol optimised and adapted for large samples

Expansion microscopy protocols are revolutionary in the world of biological imaging, increasing resolution beyond the capabilities of the imaging platform. The eMAP protocol was particularly interesting since immunolabeling is able to be performed post-clearing, retaining an environment with more opportunities of labelling since the clearing process isn't harsh enough to destroy many proteins. As it stands, the protocol is problematic since thick tissue volumes are not able to be uniformly fluorescently labelled. I wanted to improve the protocol, developing a modified and robust version for large tissue volumes and up to the entire mouse brain, something that until now wasn't achievable.

Initial trials revealed unsuccessful immunolabeling where antibody penetration failed to penetrate to depths beyond the superficial layer to the surface. I considered that some molecules, particularly antibody molecules, are too large to penetrate the cellular membranes and, therefore, are not able to detect intracellular proteins deeper in the sample. Hence, a permeabilisation step was investigated to facilitate this passage; permeabilisation facilitates this passage, allowing molecules to reach the centre of the sample and, thus, improving incubation times.

When working with large samples, time efficiency remains a key goal and hence the different buffers and concentrations were investigated to optimise this step. A whole mouse brain was divided into four equal quarters to maintain the thickness of a diffusion gradient in a standard, large sample. CHAPS was initially tested as suggested in a 2020 paper due to the small micelles that improve deep tissue penetration in both depth and

speed (S. Zhao et al., 2020). I employed the use of varying-concentrated PBST in this investigation since I aimed to produce a protocol featuring standard laboratory detergents when possible.

The samples were first incubated in the permeabilisation buffer of varying concentrations, from 1 – 10%, for 24 hours. One set of samples were left at room temperature and the others at 37°C. Once done, the samples were incubated in blue ink overnight in order to have a comprehensive understanding to which depth the diffusion liquid arrives at in this time period. Referring to the images below, the quarter of brain samples were then halved in order to see the centre of the tissue volume. What was cleared was that the buffer of highest concentration (10%) at 37°C achieved the deepest and most homogenous penetration through the sample volume.

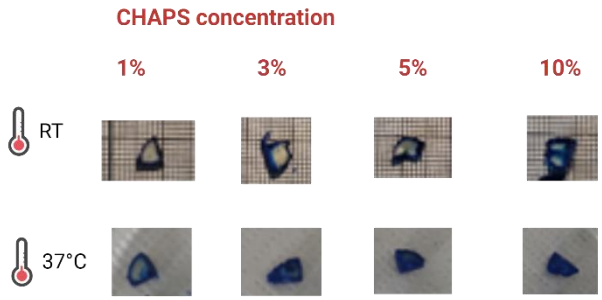

Figure 7.1 Varying concentrations of CHAPS buffer followed by incubation with blue ink to test sample penetration.

One the left the samples were incubated at room temperature while on the right, the samples were incubated at 37°C. The higher temperature samples showed greater penetration and therefore more successful permeabilisation effects with the higher concentrations penetrating the full sample.

Expansion Microscopy (ExM) scaled and optimised for large samples

The initial protocol had implemented the use of a permeabilisation step yet initial trials failed to render the sample transparent, even with increased incubation time. I observed sample deteriorating and had concluded that the polymer network had not been formed in the centre of the tissue volume. Supposing that the monomer and gelling solution had

not been able to penetrate deep enough into the sample, I focused on adjusting the permeabilisation step.

Following the results from the investigation into the concentration of the expansion buffer with respect to diffusion distance over a fixed period of time, I decided to implement a higher-concentration permeabilisation buffer rather than further increase the incubation time.

From here, the protocol remained as before with subsequent incubation steps of 48 hours for ¼ samples which effectively cleared the samples beyond the superficial layers.

In optimising permeabilisation, the sample is able to be penetrated more effectively in the following steps allowing for effective incubation times.

7.2 Effects of permeabilisation step on immunolabeling

eMAP (Epitope-preserving Magnified Analysis of the Proteome) protocol optimised and adapted for large samples

Labelling of features deep inside large volumes of tissue had been consistently problematic with the original eMAP protocol. Antibodies reached only to shallow layers inside the tissue volume with large quantities remaining on the surface layers, seemingly unable to further penetrate. The goal of this research was to achieve full labelling throughout a fully expanded brain and obtain a robust and reliable methodology able to reliably be replicated.

I worked on the premise that larger samples needed to be thoroughly permeabilised in order to facilitate the passage of antibodies through the entire thickness. Permeabilisation effectively punctures the cell membrane, allowing entry through the cell membrane in order for primary antibodies to reach the intracellular membranes. The importance of this added step is reflected in the results obtained through the imaging of these samples using light sheet fluorescence microscopy both pre-expansion and post expansion.

Mouse brains were each prepared equally using the modified eMAP protocol. The investigation variable being the permeabilisation step, other steps served as control variables. Each sample was half of a mouse brain of a transgenic line where neurons endogenously express tdTomato. Fixed tissue was incubated in the permeabilisation

buffer, 5x PBST, for 24 hours, 48 hours or no time at all. The samples were imaged pre-expansion with RI-matching solution TDE 68%.

Considering the cerebellum of these half brains, the distinguishing features and the dense neuronal projection populations make this an ideal brain region to draw comparisons. In figure 7.2 slices are compared from an optical section close to the surface of the brain and that deeper into the sample, a section deeper in the axial directions; the contrast has been set equally between the comparative images. What's clear is that, without the permeabilisation step, the signal fails to penetrate beyond the surface of the sample as reflected in the axial slice closer to the surface. Once moving towards the centre of the tissue volume, signal intensity reduces significantly with minimal staining of the axons. Taking a reslice of the axial stack, the signal can also be evaluated from another axis. Here, the attenuation of the fluorescence is distinctly limited to the borders.

When evaluating the effects of the permeabilisation incubation time between 24-hour permeabilisation and 48-hour permeabilisation, there is little significant difference between the samples. Each displays a strong signal that penetrates similarly through the sample, revealing the dense axonal projections. When considering deeper axial segmentations, as well as the resliced through the axial axis, signal reduces at particular depth giving rise to further investigations of antibody incubation times and concentrations, since standard parameters were used as a control in this study.

What can be said is that the permeabilisation step is crucial in this protocol when applied to large tissue volumes as the tissue is rendered from a state of minimal-to-no fluorescently labelled features to a remarkable display of thorough labelling. Since one expects to lose signal by factors of x64 when considering a x4 expansion factor, pre-expansion signal should be strong in order to evaluate the viability of labelling prior to undergoing expansion.

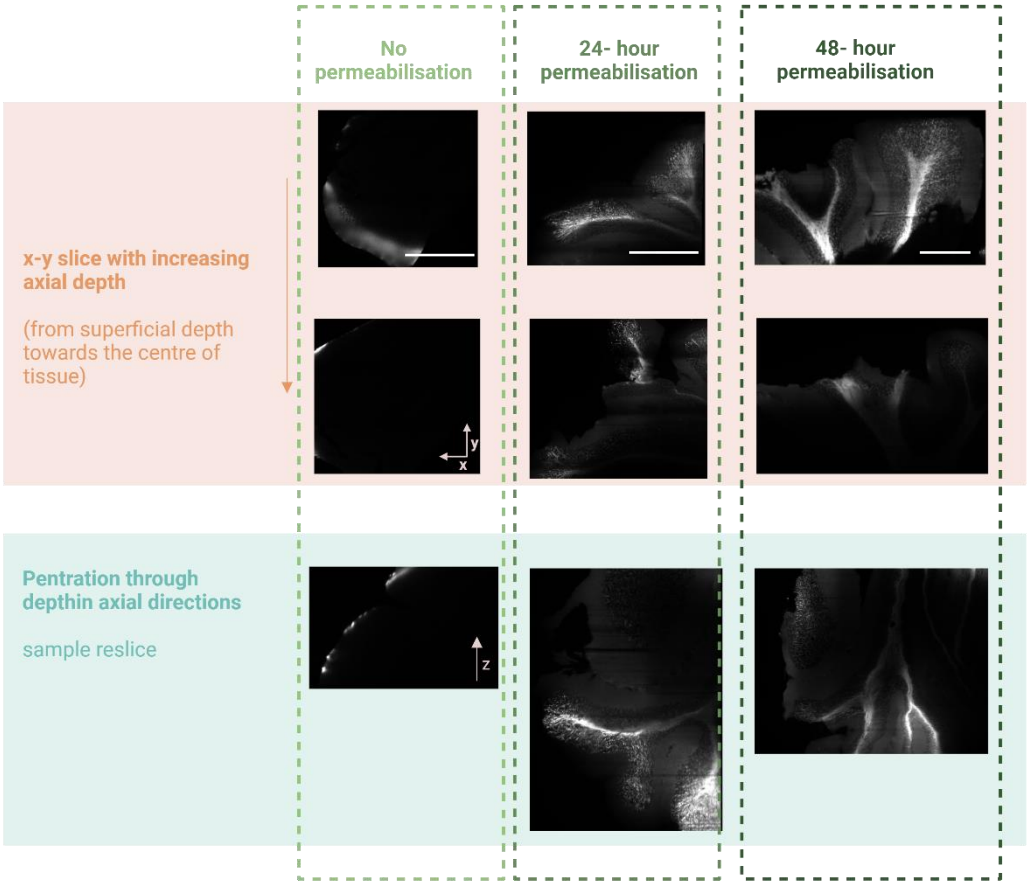

Figure 7.2 Comparative immunolabeling resulting from experimental permeabilisation steps.

In orange, the images show two optical segments in the same sample, one closer to the surface and the second towards the centre of the sample. With contrast set equal in all images, the sample without permeabilisation displays significantly less signal in which features are not able to be recognised. In green, each image shows a cross-sectional cut through the sample showing the axial diffusion of the fluorescent signal. Again, it is remarkably clear here that the permeabilisation step aids the diffusion of biomolecules through the tissue-gel hybrid in order to bind to the target. Scale bar = 100 µm. The samples were imaged pre-expansion.

7.3 Efficient clearing of sample and removal of the clearing solution

eMAP (Epitope-preserving Magnified Analysis of the Proteome) protocol optimised and adapted for large samples

Pre-expanded samples have a slight opaqueness to them that becomes more evident when removed from the denaturing solution and held towards the light in which a degree of scattering can be observed. This effect is not present, however when the sample is expanded and doesn't contribute to scattering of illumination light or successful antibody staining.

Successful antibody staining relies on the full clearing of the sample avoiding opaque regions affecting imaging quality. A useful measure is to analyse the sample over a black background, or milli-metered paper, which renders opaque regions visible. Demonstrated in figure 7.3.1, 2mm cleared samples in a 6-well plate against a black background used to determine the transparency of the tissue.

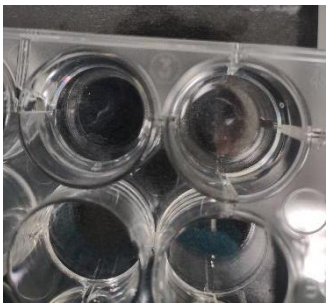

Figure 7.3.1. 2mm-thick mouse brain tissue slices controlled against a black background to render un-cleared features to be visible.

As can be seen in the top two well plates, small opaque regions exist in the slices and therefore longer incubation is needed in the denaturing solution.

Samples with opaque regions prevent successful labelling since large molecules, like antibodies, fail to permeate through the dense tissue. The crucial nature of effective clearing was demonstrated on thick slices, 2mm, which were prematurely removed from clearing. The samples were then incubated with nuclear staining (Hoechst) in order to visualise the point at which the staining reached. The intensity profile of fluorescent was measured along the axis from the surface of the sample through to the centre and subsequently normalised for comparison as presented in figure 7.3.2. The samples were then incubated for several more days until total transparency and thoroughly washed again before a second round of nuclear staining and the sample measurements were taken from the acquired images.

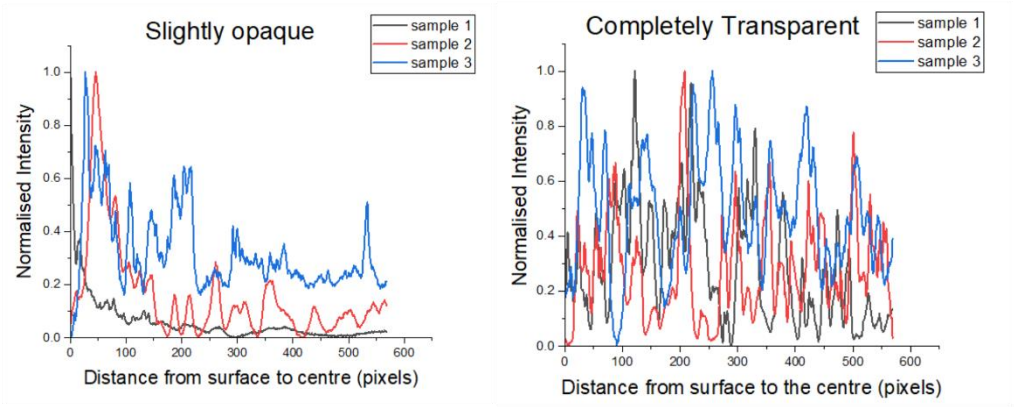

Figure 7.3.2 Three 2mm-thick brain samples imaged at two points during the denaturing process.

The first graph represents the data taken from the samples with slightly opaque regions present in the tissue, after 10-12 days of incubation with the denaturing solution, which reflects an exponential decrease in fluorescent signal as the penetration depth increases. Moreover, the second graph reflects the data taken with 5 days extra clearing in which the fluorescence is able to almost linearly label the targets throughout the tissue volume.

7.4 Expansion factor

Estimated expansion factor

eMAP protocol optimised and adapted for large samples

A preliminary expansion factor was able to be measured by taking the measurements, length and width, of the samples before starting the protocol and after, following expansion. This also served the design purpose of the customised optical system, discussed in part 3, which would be capable of measuring fully expanded mouse brains. In doing this, sample mounting was also considered in order to avoid cutting or slicing the tissue. The system must be capable of reaching the expanded distances that aren't usually feasible in commercial and even customised set ups.

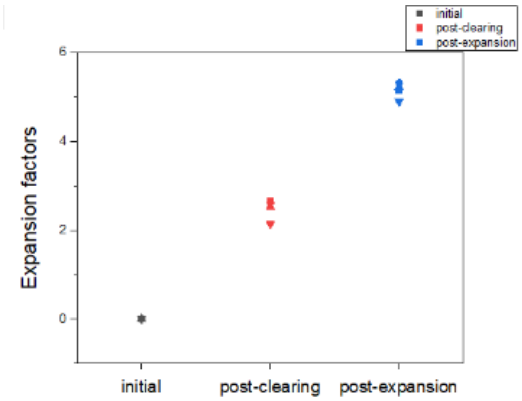

Figure 7.4. Preliminary data of expansion factors throughout experimental procedure.

4 samples of ½ brain and full brains were measured throughout the protocol in order to be used as a reference in building the light sheet microscope (Part 3) capable of imaging a whole expanded brain.

The results, shown in figure 7.4, provided grounds for sample preparation and mounting during the protocol. Since the sample sees an expansion during the clearing steps of factor x2.54 ±0.27, standard deviation, and therefore considerations must be taken in choosing the incubation equipment. Using a Falcon conical tube, a full brain was able to clear and with room to grow. An estimated expansion factor of x5.34 ±0.3, standard deviation, was therefore used in designing the optical system. The table below provides the data used to calculate these expansion factors.

Sample	**Initial**		**Post-clearing**			**Post-expansion**		
	Length (mm)	**Width (mm)**	**Length (mm)**	**Width (mm)**	**Expansion factor**	**Length (mm)**	**Width (mm)**	**Expansion factor (mm)**
1	15.3	5.8	36	18	2.73	73	37	5.58
2	15.4	6	37	17	2.62	74	37	5.49
3	15.4	5.9	36	18	2.69	72	36	5.39
4	15.2	12.25	34	25	2.14	72	62	4.9
				Average	2.54		**Average**	5.34
				Standard deviation	0.27		**Standard deviation**	0.3

7.5 Distortion Analysis

eMAP protocol optimised and adapted for large samples

Chung et al prove that the original eMAP protocol produces homogeneous and linear expansion, sustaining the architecture of the molecular network without server distortion. Here, I compare acquired data of the same samples in pre- and post- expansion states to assess if distortion is minimal with the modifications I have made to the protocol.

Figure 7.4 displays image data taken from the same samples that have been imaged in RI-matching solution 68% in a non-expansive state and those that have been imaged in DI-water following expansion on the respective light-sheet microscopes. I highlight the characteristic features of the cerebellum that remain consistent in both states, attaining to the principle of homogeneity and linearity of the expansion in each dimension.

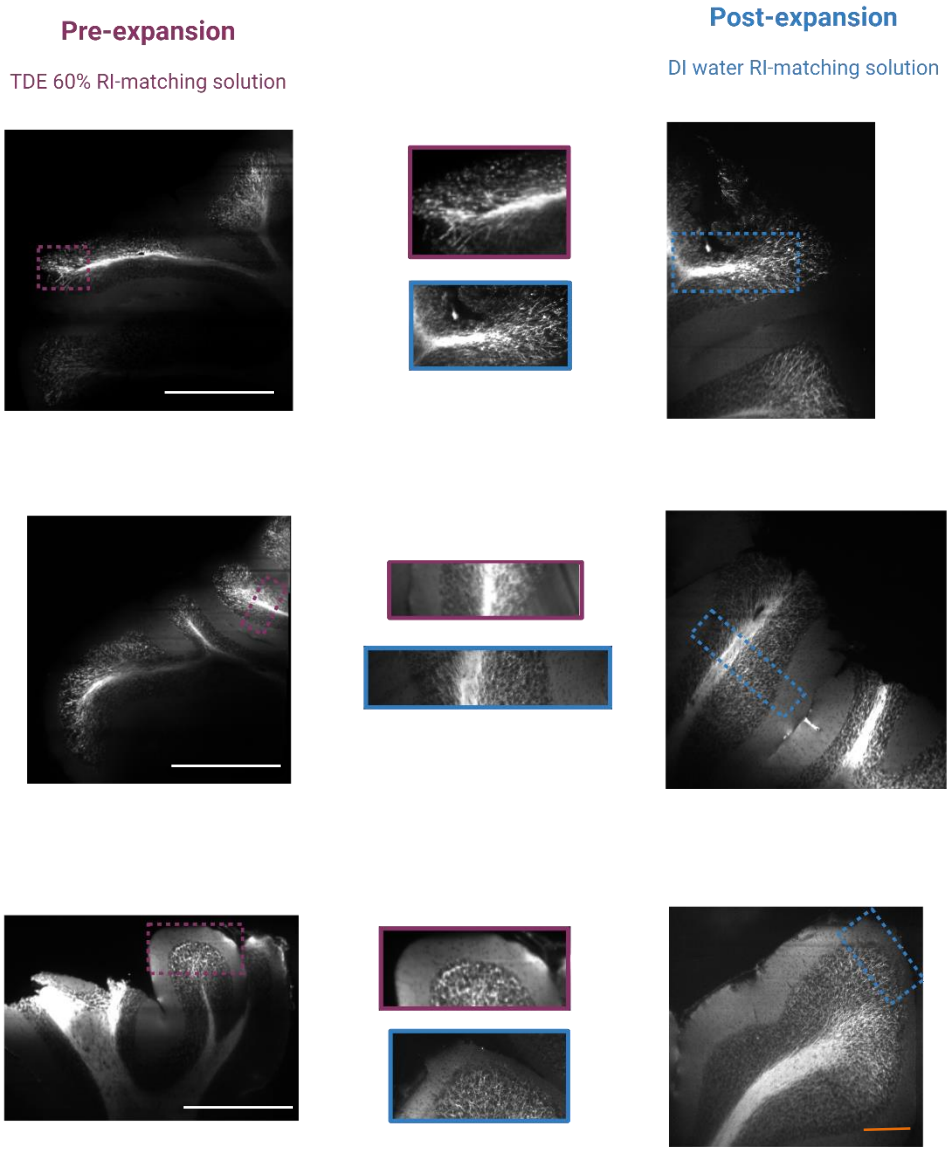

Figure 7.4 Pre- and Post- expansion image data of the cerebellum in order to assess distortion

Key features from the pre-expanded brain (magenta) are compared to those of the post-expanded brain (blue) maintaining its structural identity through the withheld structures in both data sets. Neuronal morphology appears to be undisturbed during the expansion process, remaining in their respective spatial positions. White scale bar = 100 µm, orange scale bar = 1 mm expanded.

7.6 Antibody affinity to hydrogel in eMAP protocol optimised and adapted for large samples

Preliminary data showed that some types of common antibodies used in immunolabeling had a tendency to cluster in any remaining gel left on the sample surfaces. Acquired images show strong signals located at the surfaces of the tissue volume with little signal in the deeper central parts. Despite varying incubation times and antibody ratios, the same effect was seen.

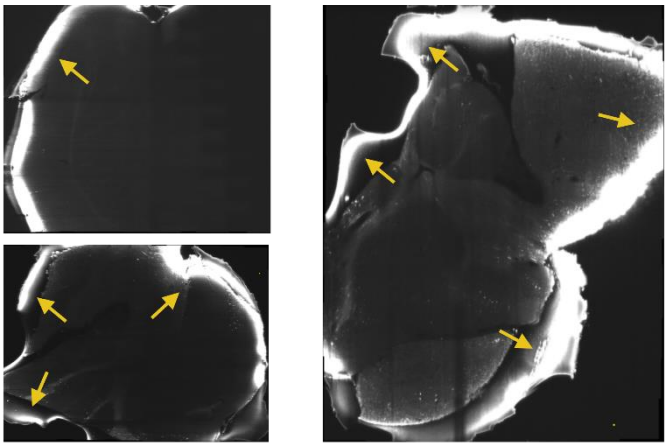

Figure 7.6.1 Slices of mouse brain tissue on which some gel remains attached

The images indicate a great build up in fluorescent signal, seemingly trapping the antibodies in the regions where the gel is still present. Very little signal is shown in the tissue itself with much saturation remaining on the borders inside the gel.

What was noticed was that this effect tended to be more prominent in samples in which some gel remained outside suggesting that the antibodies had an affinity to the hydrogel and so remained there more readily than proceeding towards the sample. In support of this, it was also found that the gel itself had differing characteristics that its gel-tissue counterpart suggesting that the pore size maybe not be equal. It could be possible that the antibodies can less easily penetrate through the gel alone. The gel alone was able to be expanded to a much greater volume than when polymerised with biological tissue.

To test this 2 mm-thick slices of hydrogel were prepared following the same protocol as the tissue-hybrid counterpart. One of the slices was incubated primarily with secondary antibodies while the second slice was incubated with both primary and secondary antibodies. All concentrations were performed at 1:500 at 37°C as performed in the standard protocol. Figure f displays images taken of the gel slices, showing clearly that in the case of the primary and secondary antibody, the signal remains close to the border unable to penetrate into the sample. Despite undergoing several washes prior to imaging, and before secondary antibody incubation, the primary antibody appears to be hindered and trapped inside the matrix. Meanwhile, the slice that is incubated solely with secondary antibodies appears to have no antibody present following several washes indicating that the antibodies have left the gel after finding no target to bind to.

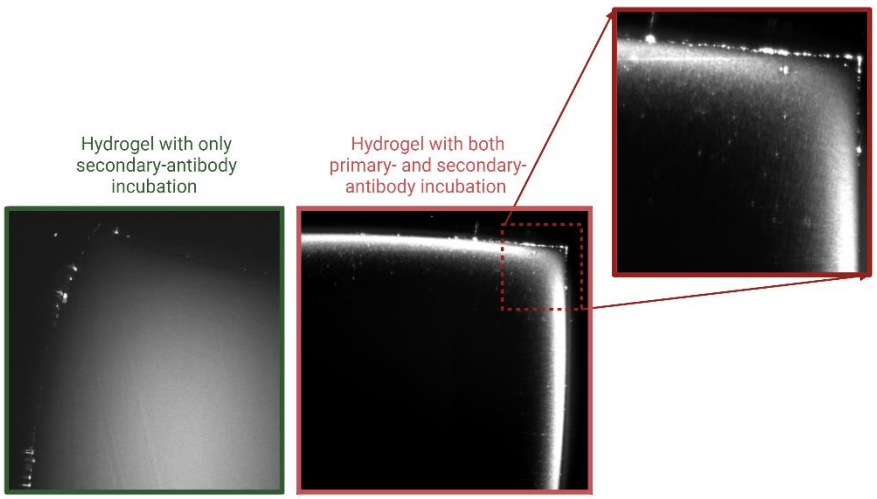

Figure 7.6.2 Comparative images of eMAP hydrogel when subject to immunolabeling without tissue embedding.

The image on the left having been incubated with only secondary antibodies shows a sample with very little signal with simply the illuminated gel. One the other hand the image on the right depicts a heavily fluorescent border indicating the antibodies entered and were unable to pass through. This indicated that the antibodies, namely primary antibodies, have a tendency to remain in the eMAP hydrogel gel which isn't seen in the hydrogel-tissue hybrid.

Enhancing the efficiency of labelling in both penetrative and temporal terms, caution must be taken at each step to remove as much gel as possible from the sample prior to beginning with immunolabeling. In expanded samples, the tissue-gel hybrid appears more rigid than that of the gel alone gravitating to the easy removal of the gel. A caution should always be taken to ensure that the material removed is indeed only composed of gel, recognising the difference between gel and the gel-tissue hybrid becomes increasingly challenging as the protocol progresses. From my experience, I recognised that gel tends to be slightly softer with a disposition to detach from the tissue-gel hybrid.

Attaining to the fact that immunolabeling can be done even after the clearing process, there exists more opportunities to remove as much gel as possible before incubation with antibodies.

7.7 Comparison of techniques for large samples

Depending on the nature of the application in question, each of the two expansion microscopy protocols hold merit and respective shortcomings.

Endogenous fluorescence has been observed in endogenous, localised ChR2 (up to ¼ mouse brain) and tdTomato (2mm slice mouse brain) samples using the modified ExM protocol. Figure 7.7 displays images in which endogenous fluorescence is viewed following clearing and expansion to a factor of 1.7 in PBS. The nuclear staining provides a guide in which the incubation times can be tested however endogenous fluorescence should always be present and visible in transparent samples. Using the adapted eMAP protocol, endogenous fluorescence isn't present in the final sample potentially due the longevity of incubation at higher temperature causing endogenous signal to be quenched.

Figure 7.7. Endogenous localised ChR2 (red) in a cleared and nuclear stained (grey scale) ¼ brain sample at 1.7 expansion factor 4x magnification.

Endogenous, localised ChR2 at the centre of the ¼ brain tissue volume, in sagittal orientation, surrounded by nuclear staining which needed enhanced incubation times.

While both samples are rendered completely delicate and therefore must be handled with the utmost care, modified eMAP samples tend to be much more manageable and rigid than those of ExM. Even at the larger volumes reached, the sample is able to be positioned easily in the chamber, positioned with agarose gel as a support when necessary (see part 3). Dissimilarly, ExM samples at large volumes begin to rapidly lose structural identity when removed from the incubation buffer; a characteristic particularly difficult for imaging. Sample mounting in a cuvette is optimal in both cases since large samples are tedious to mount onto coverslips which is necessary in some commercial imaging systems.

From data collected in this study, large samples of ½ mouse brain used in the eMAP protocol take around 18-25 days to undergo total clearing and have been tested on samples of various sizes in order to adequately scale the protocol. Conversely, smaller samples of ¼ mouse brain cleared using the adapted ExM protocol take around 4-5 weeks The samples, however, were less numerous than in the eMAP study and the modified ExM is in the process of optimising the digestion buffer for larger samples.

On the other hand, preparation time prior to clearing sees ExM being temporally more efficient. A ¼ mouse brain sample requires 1 week of sample preparation (permeabilisation, linking, monomer, gelation) before digestion can begin while modified eMAP takes around 11 – 14 days although the successful results of the permeabilisation step suggests the hydrogel incubation step prior to polymerisation could be optimised depending on the sample itself. These factors are to be further optimised.

	Modified eMAP	Modified ExM
Scalability	**Scalable through to entire mouse brain**	**Scaled to ¼ brain samples**
Clearing time	**2-3 weeks for ¼ brain**	**4-5 weeks for ¼ brain**
Endogenous fluorescence	**No**	**Yes**
Sample handling	**Delicate but maintains structural integrity. Sample can be mounted into a cuvette.**	**Extremely delicate, especially when removed from the incubation buffer.**

7.8 Biological applications

Expansion Microscopy, combined with an efficient and reliable labelling strategy, for full mouse organs and large tissue samples provides the grounds for many research areas that require an understanding of tissue anatomy and feature morphology across a full system without the need of advanced imaging techniques. The exploitation of the available epitopes, reducing the masking and destruction of the chemical composition, enables efficient labelling in turn producing strong signals throughout the volume.

Until now, the task of scaling expansion microscopy to large tissue volumes had been problematic and current protocols aren't easily replicable or require sophisticated labelling strategies not often available to the average lab. In this work, I successfully present an expansion microscopy protocol employable for the full brain accommodating to standard laboratory equipment and reagents. Although I present proof of technique on mouse brain tissue, specifically in the cerebellum region, this technique is not limited to this. The advantages of enhanced resolution in the sample for organ-wide imaging in cost-effective manner can revolutionise the study of connectivity and functions.

Part 3 Construction of the Light Sheet Fluorescent Microscope for Expansion Microscopy / Large Volume Samples (Ex-LSFM)

Chapter 8 Optical development and sample mounting

The expanded mouse brain is the biological target that this microscope was designed around since it serves as an extremely useful model for the mapping of the human brain and subsequent relevant diseases of the central nervous system (CNS). With this in mind, the design considered the dimensions of the biological targets, the volume of tissue to be imaged and mounting of the sample during acquisition.

8.1 Cuvette design

Preliminary expansion trials of the entire mouse brain produced an average expansion factor of x 5.3 ±0.3 (standard deviation). Data to support this can be found in Part 2, chapter 7.4 of this thesis.

The average dimensions of the mouse brain along each axis are 15.3 mm (rosto-caudal axis), 12.25 mm (medio-lateral axis) and 8.5mm (dorso-ventral axis) (de Vries, Siegle, & Koch, 2023). To this end, the average mouse brain at full expansion has dimensions of 79 ± 2.6 mm x 64 ± 2 mm x 44 ± 1.4 mm.

Since the expansion factors vary, the cuvette must consider samples that deviate from the average values. With this in mind, the cuvette was designed with dimensions 84 mm (*y*) x 70 mm (*x*) x 50 mm (*z*), orientations in figure 8.1.1, and their respective axis for imaging, supported by 3mm-thick walls, shown in figure 8.1.2. The length along the y-axis exceeds the sample measurements to account for easy mounting and to easily attach to microscope stages.

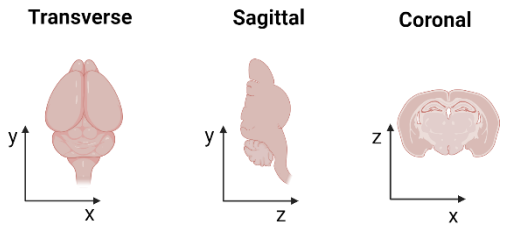

Figure 8.1.1 Orientation of full mouse brain in cuvette with respect to imaging.

The x and y coordinates form the dimensions of each optical slice while z aligns with the axial depth with respect to imaging and camera orientation.

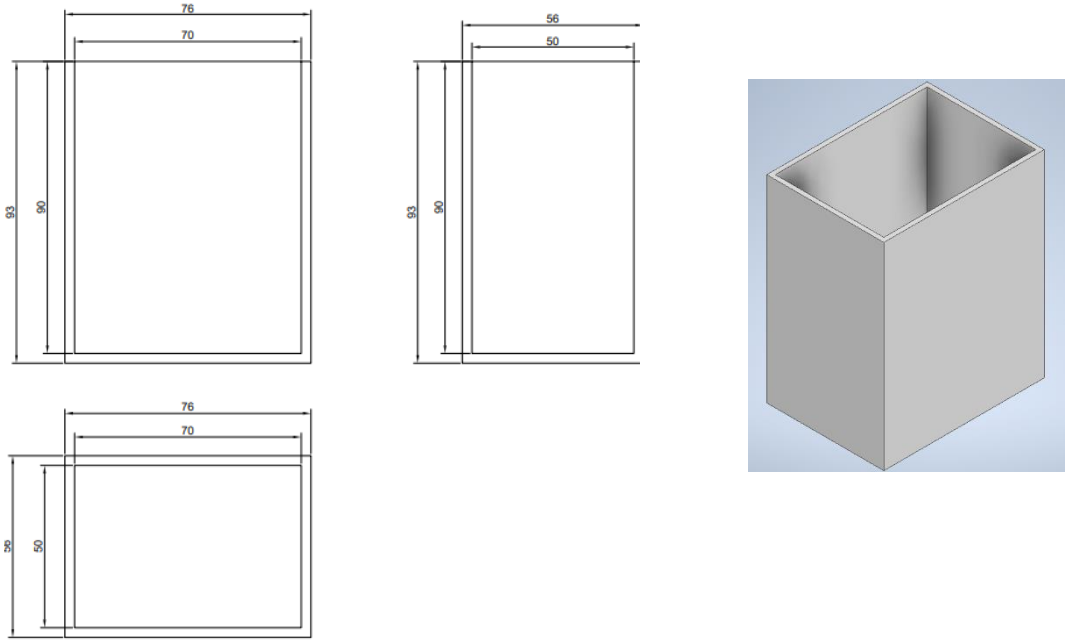

Figure 8.1.2, 2D and 3D cuvette design.

2D design featuring dimensions of cuvette as well as wall thickness appropriate for housing a fully expanded mouse brain.

The material of the cuvette was an experimented factor. Initially, the idea was to use a material with a matching RI as water in order to minimise any diffraction when light moved from the sample, to the water that it was immersed in and also passing through the cuvette walls. The refractive index of water is 1.33 for visible light at room temperature; indeed, the value the sample will attain at full expansion when submerged in water. A promising material is perfluoropolyether (PFPE) which can be customised to achieve a refractive index in the range of that of water.

Initial trials to polymerise this material began with a suitable thermal initiator to thermo-cure the material. Curation in a thermal reactor took place at 120°C. In doing this, a customised mould was created to support the desired structure while curation took place. The design of this mould is shown in figure 8.1.3.

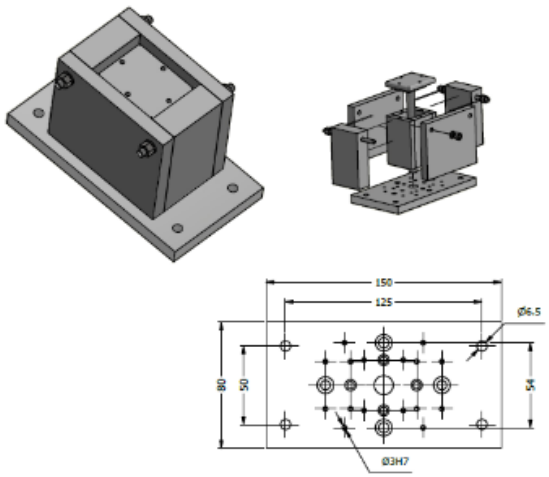

Figure 8.1.3. Initial design for a cuvette mould during curation in a thermal oven.

Material was poured into the mould before being curated and solidifying. The mould supported the final, desired shape while the material underwent curation.

Once completely cured, the material was left to cool down before being removed. Unfortunately, the high temperatures produced in the thermal reactor triggered a reaction by the thermal initiator, producing a characteristic yellow tinge in the curated product. Furthermore, the structure also cracked and separated, again a consequence of the high temperature. Given the dynamics of the mould, there was likely temperature - inhomogeneity within the structure during the curation process resulting in a non-uniform process.

To face this challenge, a new strategy was implemented in producing each face of the cuvette individually in a stable environment. A photo-initiator reagent was used in place of the thermal-initiator. A solution of PFPE with a photo-initiator was produced of thickness 1mm and 2mm in order to test if the solution could be photo-polymerised and possess appropriate qualities for the prospective cuvette. The rigidity of the material was an important factor since delicate samples, for example mouse brains prepared with Expansion microscopy, needed to be well supported during sample mounting and acquisitions.

The solution was placed in a mould under ultraviolet light, sealed in a container with an influx of nitrogen; this wasn't able to be done in a degassing chamber since the process of degassing distorted the liquid before nitrogen influx could begin. The flux of nitrogen in a sealed container caused air movement that interacted with the sample leading to uneven surfaces in the final product; swirls could be seen on the surfaces causing uneven thickness in the material and bumpy surfaces. A primary goal is to reduce scattering and diffraction for the photon path which would ultimately be increased with a cuvette without optically-flat surfaces and varying densities.

A simpler method was eventually decided upon in order to produce the cuvette. Recalling the goal of designing a system in which standard lab, cost-effective equipment could be used, the chemical compound, and synthetic polymer, poly (methyl methacrylate) [commercially known as plexiglass] was used. Each face of the cuvette was cut from a standard 3mm-thick piece with a refractive index of 1.49 and subsequently sealed to produce the final structure. Indeed, this commercially and readily available material can be used in designing cuvettes of varying dimensions.

8.2 Chamber design

Dimensions of the sample too governed the dimensions of the chamber, which the optics would eventually build around, from the central to the light source. The sample, held within the cuvette, would be mounted from above by stages raised over the illumination path, directly above the sample chamber, see figure 8.4.1. By entering from above, the stages could easily have space to move the relatively long distances, several centimetres, without

disturbing the illumination or detection pathways. Moving through the light sheet beam waist, the centralised field of view would remain static, while each point of the sample reached the imaging plane. The chamber width, length and depth therefore had to accommodate this flexibility in which each point of the cuvette can comfortably access the field of view. The x- and y-axis must be of at least double the length of that of the cuvette since the light sheet would be centralised in those planed, allowing for the imaging of the extremes in that respect. The z-axis was subject to the conditions of the detection objective. Indeed, finding a working distance (WD) to adhere to the results of a 5x expansion factors falls outside of the general range of most liquid medium immersion objectives. After reviewing several options, a long WD objective of 29 mm was selected and so the z-axis could be modified around this parameter. This WD is long enough to reach the centre of the cuvette but doesn't accommodate the full penetration in order to image the deepest voxels depicted in figure 8.2.1. What this meant was that the sample must be eventually rotated after imaging half of the cuvette followed by the imaging of the second half of the cuvette. Indeed, smaller samples can be adequately mounted, or imaged using a narrower cuvette in which rotation isn't necessary to image the entire sample. Windows, through which the illumination and detection arms could reach the sample, were incorporated. A few mms were also added to axis to avoid the touching of the cuvette walls to the chamber walls, reducing the effects of induced motion or disturbance to the system during acquisitions

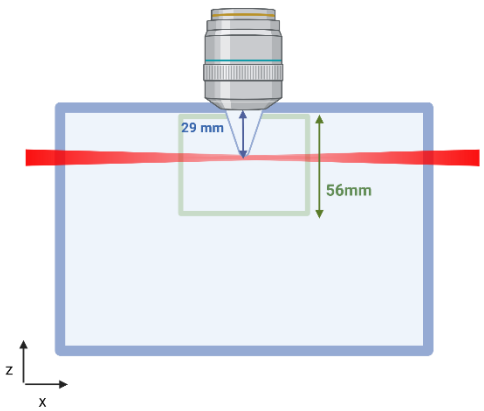

Figure 8.2 1 Schematic display of cuvette depth and objective working distance in z.

Sample must be rotated in order to facilitate the imaging of the second half of the cuvette in the z-axis since the working distance of the detection objective reaches only half of the cuvette.

The final dimensions of the chamber were therefore 114 mm x 159 mm x 192 mm interiorly and 120 mm x 165 mm x 195 mm comprising the 3mm-thick walls and the top face remaining open as shown in the 2D sketch and 3D CAD design in figure 8.2.2.

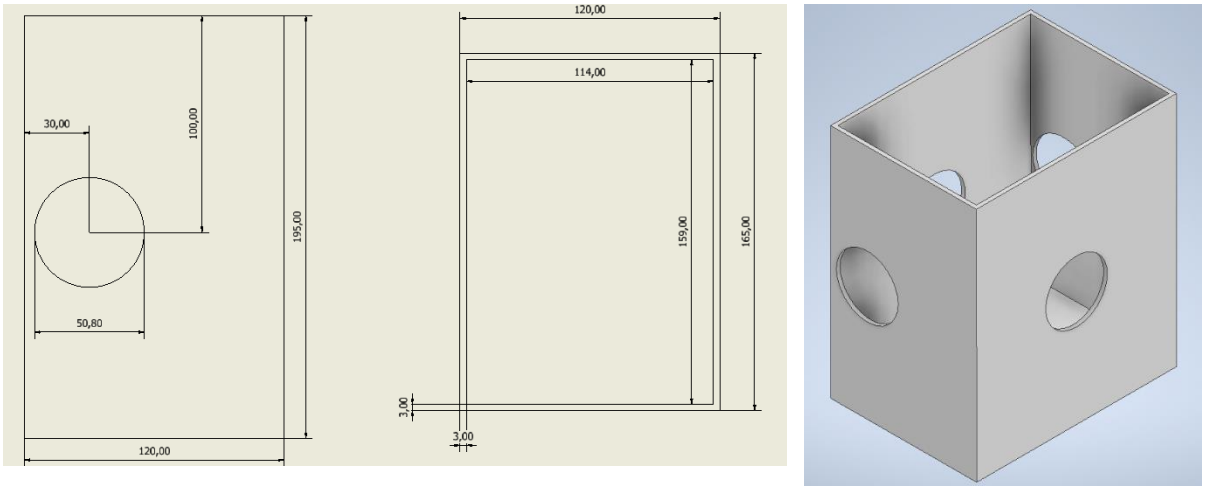

Figure 8.2.2. 2D design and 3D sketch of the chamber.

The aluminium housing accommodates the moving cuvette and facilitates the entrance of the illumination and detection paths meeting at the imaging plane, where the camera field of view and beam waist is also located.

For cleaning purposes, the chamber must be able to be removed easily. To this end, the detection objectives remain unattached to the chamber, entering via the entrance holes which were sealed with glass cover slips. To seal the two materials, silicon was used as an adhesive since it doesn't react decidedly with either aluminium or water. The diameter of these entrance holes matched that of the scan lens in order to maximise usable light sheet amplitude. Forming the system to stabilise and immobilise the chamber, a simple custom adapter was created to attach the chamber and stabilise it, using, screws, to a fixed rail (Thorlabs XT95SD-250) and a rail carrier (Thorlabs XT95RC4/M), shown schematically in figure 8. 2.3.

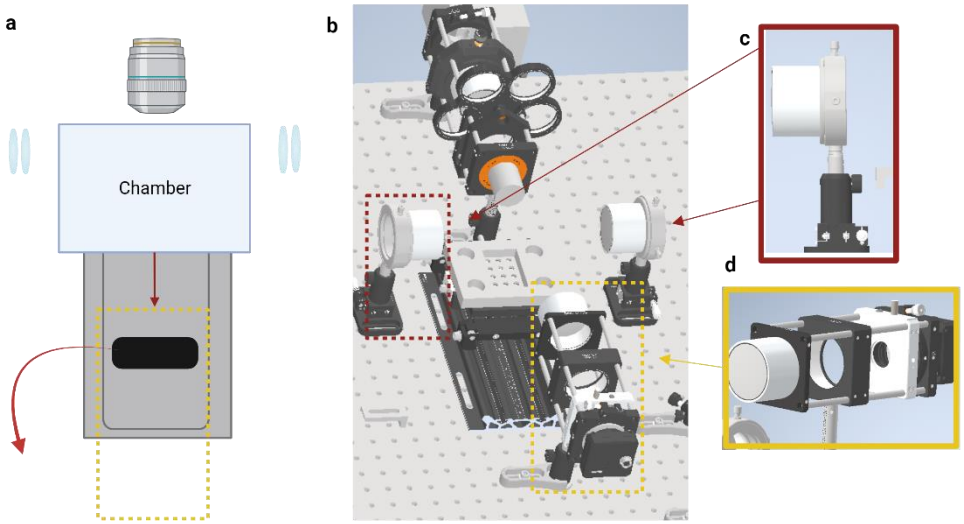

Figure 8.2.3. Illumination and detection objectives mounted around the mounting rail and carriage on which the imaging chamber is placed and able to be removed from the set up.

Image (a) shows the set-up of all objectives, two for illumination and two for detection discussed further on, around the chamber. For purposes of clarity the supporting stages, mounted above the chamber aren't shown. Due to the obstruction of these stages from above, the sample must be removed laterally. To account for this, the scan lenses must be able to be adjusted and moveable of several mms to allow the secure removable of the chamber. Shown in image (b), these scan lenses are mounted on manual translational stages (Thorlabs MS1S/M) to facilitate this removal. The second detection arm shown in inset (c) is also mounted on a single post mount allowing the rotation of the cage system, supporting the detection arm, to allow full use of translation of the chamber along the mounting rail.

Due to the effects of background light reducing the optimisation of fluorescence detection and reducing the signal-to-noise-ratio (SNR), the chamber had to be made of a material that could both conceal the sample from the light and be of a material with little reactivity to water. Aluminium therefore was selected due to its low reactivity with pure water, its opaque nature and the ability to be moulded into robust shapes. The 2D and 3D sketches were used to customise the chamber design to be totally watertight once the detection and illumination entrances were sealed.

8.3 Sample mounting

Large, cleared samples are delicate in nature and require delicate mounting. Since biological tissue is irregular in nature with fluctuating thickness throughout, the sample must be mounted in order to acquire images in its natural and static state. The frangibility causes an unsupported system to float and move if not supported adequately in the cuvette. A cuvette of similar dimensions is first selected and then supported using agarose gel 1% can be used to prop the tissue towards the cuvette, while not interfering with the illumination direction in order to stabilise the structure when immersed in water.

Once prepared, the cuvette can be mounted in the optical system via a connection to the translational stages. Translational stages in x, y and z directions are positioned above the sample chamber, as shown in 8.3 (a) below, with a mounting system that suspends the sample from above allowing the user to comfortably connect the cuvette before guiding it to the light sheet, as depicted in figure 8.3 (c) before.

The cuvette and translational stage are securely connected via a customised connector composed of a generic post mount and post mount holder that are secured to the translation stage above. The post, when removed from the attached post holder, attaches to a second piece with screw threads through which the cuvette can be attached. The cuvette features holes in order to allow the screws to be fixed as shown in image (b) in the figure below.

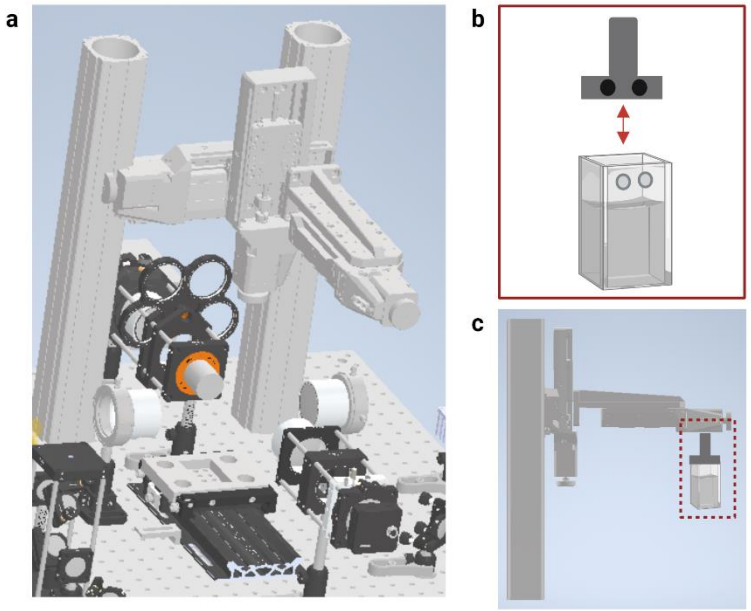

Figure 8.3. Sample mounting on the ExM-LSFM

Image (a) shows the positioning of the translation stages that are mounted via posts in order to be arranged on top of the imaging chamber. Here the sample can be lowered into the light sheet, positioned at the point in which each illumination and detection objective share a focal plane. Image (b) represents a simplified scheme through which the sample is mounted. The cuvette features holes through which a screw can enter to be screwed into the threaded holes in a piece that sits at the entrance of the cuvette. This is then attached to a generic optics post and subsequently fixed into a standard optic post mount that is securely fitted to the stage, shown in image (c).

8.4 Illumination

Below, in figure 8.4.1, is a full schematic of the optics included in illumination path way, pinholes irises are not represented.

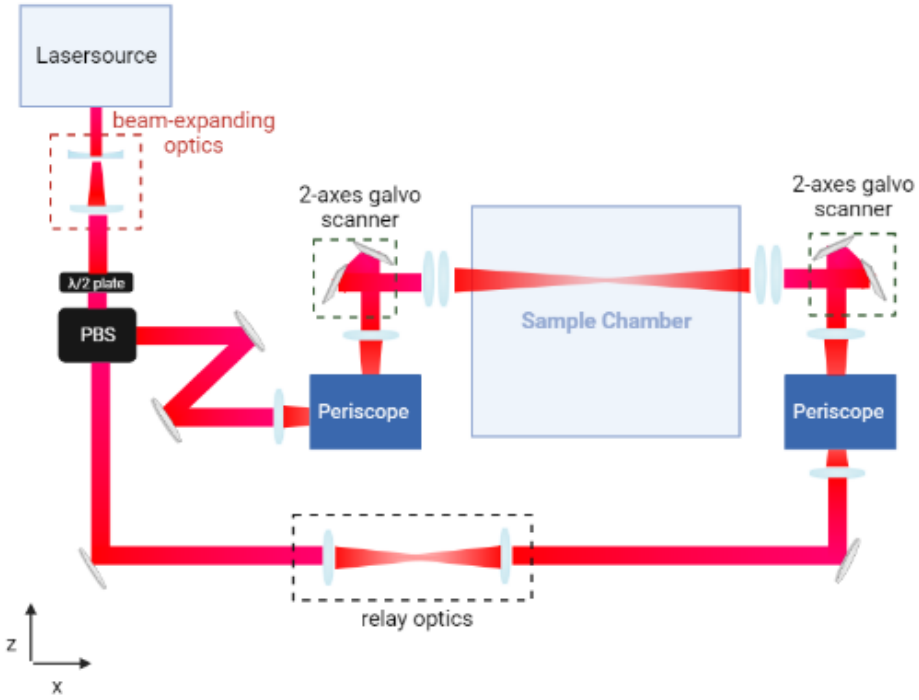

Figure 8.4.1. Schematic representation of the illumination optics

From the laser source, two light sheets are produced which meet at the centre of the sample chamber, customised for the imaging of large, expanded tissue samples. The respective pathways illuminate the sample with equal beam-characteristics due to the design of each path.

The process of designing the illumination system was based around the sample and the mounting. The first consideration was the dimensions of the sample chamber where the beams had to be guided to, reaching the entrance height to illuminate the sample. The second consideration was the desired axial resolution, determined by the beam waist that is produced by the illumination optics. When selecting the appropriate lenses and objectives, the characteristics had to adhere to the desired output, for example beam thickness and Rayleigh length, and physical restraints, for example the entrance height of the imaging chamber.

Optimising the homogeneity of the illumination light deep in the sample, the design features dual-sided light sheet illumination in that two opposing light sheets penetrate the

sample from opposite directions which remain orthogonal to the detection objective. Not only would this be an elegant application for enhancing the uniformity of the illumination of features within the sample, it also aids in illuminating samples with scattering properties or defects causing light to be absorbed in the illumination path causing shadowing effects.

The thickness of the light sheet is achieved through the illumination optics. The initial beam thickness can be modified from the source using a beam expanding/contracting system. Beam expanding optics utilises a classical telescope system positioned in a Keplerian arrangement in which the focal lengths of both lenses are positive and are separated by a distance of their combined focal lengths and the magnification of the beam is a product of the ratio between the lenses. An alternative and more compact design is the Galilean telescope set up, shown in figure 8.4.2, which employs one lens with a positive focal length and a second with a negative focal length which means there is no shared focal point between the lenses. Instead the combined focal lengths, characterising the distance between the lenses, leads to a value that creates a closer distance between then lenses than the Keplerian design. This design also outputs an upright image so in general, a correction lens is not necessary which is not the case for the Keplerian design. Once the initial beam diameter has been established, the light-sheet thickness relies on the NA of the lens projecting the beam into the sample, the convergence angle (θ), which generates the form of the light-sheet: often a scan lens. The strength of this lens determines how much the lens will converge and therefore establishes the parameters of the Rayleigh length, half of the confocal parameter, which initiates the distance where the beam is said to have a relatively constant thickness and therefore the functional field of view (FOV).

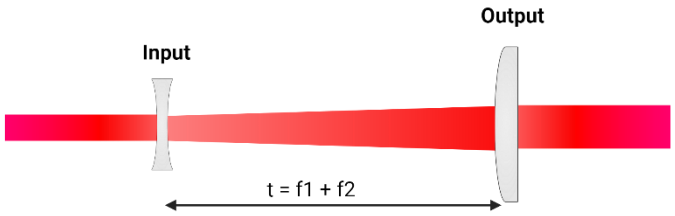

Figure 8.4.2 – Galilean telescope design

Two lenses, one of concave design and the other of convex design, create a compact beam expanding system where the ratio is defined as the ratio between the respective focal lengths if positioned apart by their combined focal length.

A Galilean design was opted for in order to minimise the space taken up by the beam expanding system in which an expansion factor of 2 was produced using a 100mm convex lens and a -50mm concave lens. From the laser source (Coherent Sapphire LPX,), the expansion factor was implemented to work towards achieving the desired beam waist and subsequent axial resolution.

Two opposing beams depicted, for representation only, in red and orange unite at the centre of the imaging chamber in which the beam waists overlap to form a relatively uniform light sheet across the chamber width. Due to the increase in photons and opposing directions, the beam waist features a near homogeneous intensity throughout the confocal parameter, see figure 8.4.3.

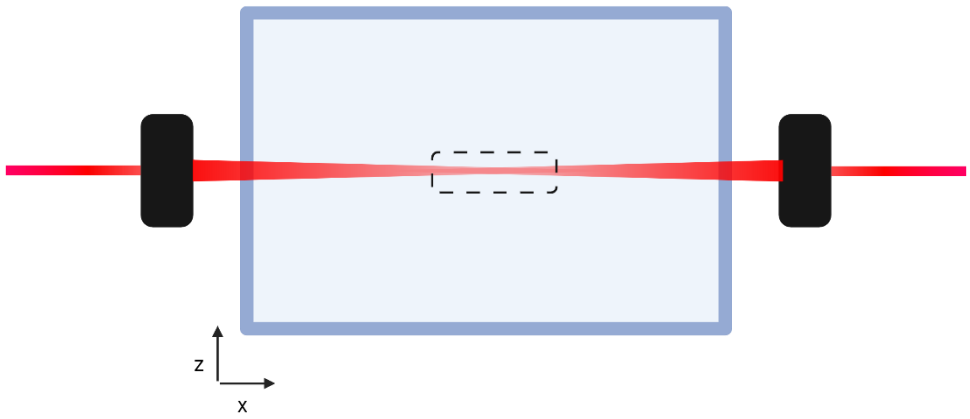

Figure 8.4.3. Dual-sided illumination

Beam waists are overlapped at the centre of the imaging chamber from opposing directions, featuring a confocal parameter of near homogeneous intensity.

Forming the two illumination arms, the expanded beam splits into two individual beam paths. A half-wave plate and polarising beam splitter was the selected modality for creating the two illumination paths from a single beam.

Half wave plates, also referred to as retarders, are devices which serve to alter the polarisation of a laser beam. They are made of a thin layer of birefringent material oriented at a specific angle to the optical axis which induces a phase shift between two polarisation

components. There are two principal axes, fast and slow, which exhibit different RI causing this difference in velocity.

Birefringence is an optical property possessed by certain optically anisotropic materials in which the refractive index depends on the polarisation of light in addition to the direction of propagation. This phenomenon causes an incident light ray to be split into two sub-rays proceeding along different paths; namely, the ordinary ray and extraordinary ray. Birefringence can be quantified in a material by the maximum difference in RI possible. First described in 1669, Danish scientist Rasmus Bartholin noticed this effect in calcite crystals and was later further described in terms of polarisation in the 19th century by Augustin-Jean Fresnel. This came about due to the understanding of the field components of a light wave (Bartholin, 1670).

Polarising beam splitters serve to directionally divide a laser beam in two by means of the different states of polarisation. They are constructed typically of two prisms or plates that hold a thin layer of birefringent material in between which triggers the divide of the incident ray by means of their respective polarisation difference.

Combining a polarising beam splitter with a half-wave plate creates a system that functions as a variable ratio beam-splitter. The surfaces in both components are equipped with anti-reflective (AR) coating over the desired wave range, in this case visible light. The half wave plate is placed first, serving to change the polarisation direction of the incident laser beam followed by the polarising beam splitter that reflects s-polarised light in one direction, usually perpendicularly, yet allowing the transmission of p-polarised light. The ratio by which the beam is divided depends on the intensity ratio between the s- and p- polarisation which can be modified by simply rotating the wave plate from 0° to 45°. The ratio is governed by the rotation of the retarder; when aligned with the input vertical polarisation plane, total reflection occurs when the beam reaches the polarising beam splitter while, when rotated to its maximum at 45° to the input polarisation plane, the ray experiences complete transmission through the beam splitter. Furthermore, the intensity ratio can be modulated between the two beams. In an optical design such as this one, the relative length of the two illumination arms is different, see figure 8.4.1 of full illumination optical path, meaning the longer-travelling beam is likely to lose more intensity along its propagation since beams tend to diverge over distance ultimately decreasing in energy flux per unit area. Indeed, the selected ratio and hence orientation of the half-wave plate was tuned to produce equal power output at the sample plane from both directions.

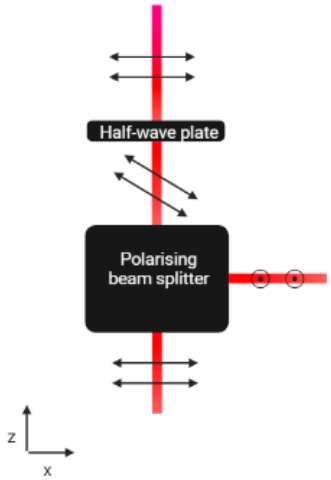

Figure 8.4.4 Formation of two beam paths from one input beam.

p-polarisation (circle) and s-polarisation (flat arrows) as one is transmitted and the other is reflected.

As aforementioned, the laser path must reach the entrance to the imaging chamber that is positioned at 136.5 mm, with an opening diameter of 50.8mm, above the optical table due to the sheer volume of the sample which is mounted on its longest axis in the y-direction. The height of the beam exiting its source is 69mm from the optical table therefore the optics must be raised by 67.5 mm to be able to illuminate the sample. In reaching this location, a 4f system was included essentially serving as relay lenses to effectively maintain a collimated laser path while navigating the laser to a higher plane. The architecture of a 4f optical system is based on Fourier optics in which two lenses are separated by their combined focal lengths. The point at which the two focal lengths meet is the location of the Fourier plane in which the Fourier transform of the input beam is placed to be output. The ratio of the focal lengths characterises the magnification induced by the system by –f2/f1 (Sharma, 2006). A -1 magnification, namely a 1:1 relay, is achieved when both focal lengths are equal. Considering the final beam diameter that should be present at the converging lens at the end of the illumination path (i.e. converging to the beam waist in the imaging plane), the system has to employ focal lengths that mechanically achieve this diameter, 100mm and 125mm respectively. These focal lengths were employed to enhance the compactness of the optical path while adhering to the desired beam waist.

The 4f system was designed in the form of a periscope, shown in figure 8.4.5, in which an incoming lens is driven orthogonally upwards to be then driven perpendicularly to follow a path parallel to the optical table effectively accomplishing the rise of the optical path height. The Fourier plane is located where the two focal lengths meet between the two lenses, strategically positioned on one of the steering mirrors. Imperatively placed to allow

easy alignment, the mirror is mounted with 2 adjusters to flexibly tilt the surface guiding the beam. From entering the system, the beam had a vertical height of 62.5 mm to travel as well as a respective distance to reach the succeeding and preceding lenses.

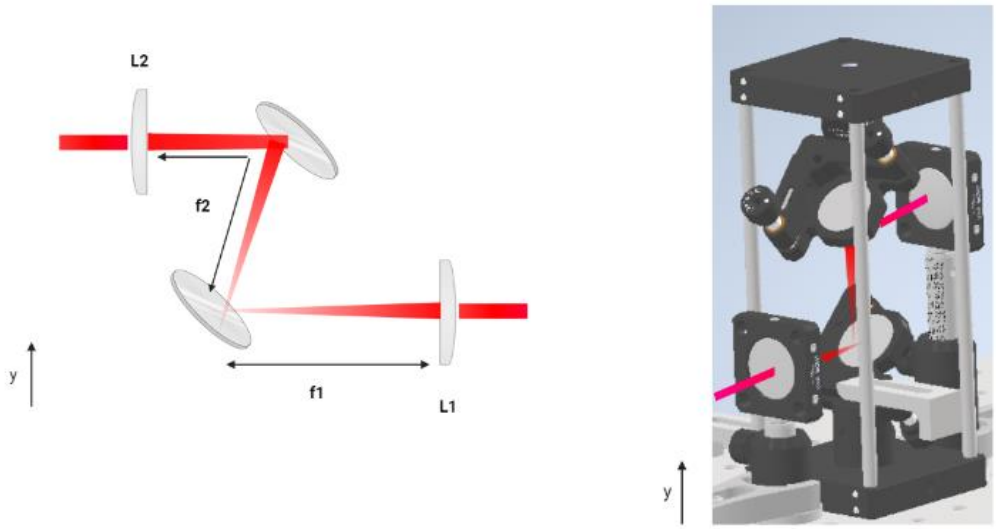

Figure 8.4.5. Periscope system.

The 4F system is arranged in a periscope design to divert the beam vertically, raising the beam path height. The intermediate Fourier plane is positioned on one of the mirrors in order to add a degree of freedom in steering the beam path.

For the longer illumination arm, 1:1 relay optics were implemented to maintain a collimated beam over a distance while creating no magnification effects since both illumination paths strive to have the same resultant beam waist. Both lenses were of 50 mm focal lengths and see separated by 100 mm adhering to the requisites for no change in magnification in which the principle is shown below in figure 8.4.6.

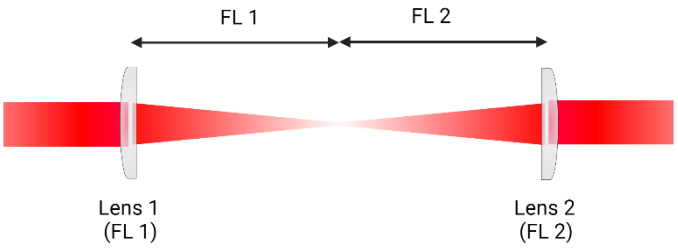

Figure 8.4.6. 1:1 relay lens system

Principle of design in which the lens is re-collimated and without any resultant magnification.

The light sheet in this setup is formed by a galvo-scanning mirror and combined with a rolling shutter on sCMOS camera (ORCA-Flash4.0 V3 Digital CMOS camera) in order to minimise background noise and artefacts. For the purpose of alignment precision, a two-axes galvanometric mirror was used in that the higher mirror, shown below in the image, produces the virtual light sheet via digitally scanning the laser beam while together with the first lower mirror the alignment is adjusted via tilting of the mirrors. Indeed, this extra degree of freedom helps to align the two illumination arms accurately, minimising the risk of increasing the beam waist through imprecise alignment and ultimately the axial resolution. These adjustments also help to correct the focus when imaging a sample. The degree of misalignment was increased due to the fact that the 2-axes galvo-systems had to be mirror versions of each other. The galvo-system (Thorlabs GVS202) is made in a housing mounted from below which directs the beam specifically in one direction and therefore was unable to be inverted and mounted in a way in which the system would be a reflected version of the original. A customised mount was therefore made to replicate the original but of the opposite hand. Due to the slight discrepancies in the design, the angular orientation of both mirrors was askew yet could be corrected computationally driven by an analogue output signal produced via a data acquisition board (National Instruments PCIe-6738). The PCIe-6738 data acquisition board is a high-density, high-speed analogue output device, capable of controlling the output waveform of 32 channels. An in-house programme was written to modulate the signal and to steer the mirrors in the correct tilt-orientation in order to adequately align the two beams coming from both galvo-systems.

Figure 8.4.7. 2-axes galvanometric mirror system.

The two systems are mirror versions of each other, one mount made in house, serving to form the dual-sided light sheet. A customised mirror mount had to be produced in order to change the hand of the standard commercial piece shown. The optical path is raised vertically by 5mm from the first mirror to the second mirror.

Once aligned at entrance height towards the imaging plane, the beam is digitally scanned through a two achromatic doublet lenses (Thorlabs AC508-100-A) functioning as a scan lens system, seen in figure l, albeit without the characteristics benefits of a flat focal plane for a deflected beam however the implementation of two achromatic doublets enhances the sharpness of the convergence with less vignetting with respect to the use of a single achromatic doublet as well as minimising chromatic aberrations for use of a range of excitation wavelengths. From here, this system will be referred to as the 'scanning' lens. Mounted in XY translational mounts (Thorlabs LM2XY/M), perpendicular travel to the optical axis allows the slight adjustment of the tilt of the beam propagation, a feature useful for dual-axis alignment. In addition to this, the mirrors were mounted on a small translational stage (Thorlabs MS1S/M) should it be necessary to extend the distance at which the beam waist needed to be positioned, or simply to move the scan lens closer to the imaging chamber, retracting it when the sample chamber is removed for cleaning. The one axis translation is actuated by a micrometre easing the movement towards other components where close proximity is necessary.

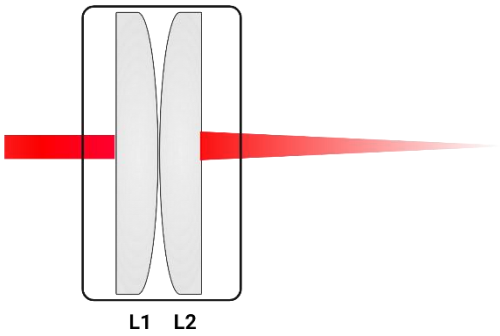

Figure 8.4.8. two achromatic doublet lenses in contact

Serving to converge the beam to its beam waist, the use of two lenses allows the adjustment of the effective focal distance while optimising the effects of chromatic aberrations.

Due to the nature of the sample, a long focal length was required to converge the light sheet towards the beam waist that should sit centrally in the sample chamber. This distance had to be 82.5 mm from the 'scan lens' entrance in the chamber considering the additional distance from the effective centre of the 'scan lens' in which the focal length is measured. Since this distance lies outside the range of standard scan lenses, this combination was designed to optimise the focal length. Utilising the improved achromatic qualities of combining two achromatic doublet lens, the Ploessl eyepiece design (Kidger & Society of Photo-optical Instrumentation, 2002), a combination was selectively chosen in order to create a long focal length lens using the equation below where f_{net} is the overall effective focal length, $f1$ is the focal length of the first lens and $f2$ is the focal length of the second lens (Sharma, 2006). To this end the two lenses selected featuring focal lengths of 200mm and 150mm respectively, achieve an effective focal length of ~85.7mm in air. Due to the slower light speed in water than air, the light becomes refracted; ray tracing approximations in theoretically calculating focal lengths with refraction employed paraxial approximations since a small angle is made to the optical axis. This enhances the length of the converging ray, resulting in a longer focal distance on the beam's path from air to water where the focal point is formed.

$$\frac{1}{f_{net}} = \frac{f_1 f_2}{f_1 + f_2} - \left(\frac{d}{f_1 f_2}\right)$$

Our goal was to achieve microscale resolution when combined with expansion microscopy, described in part 2, that achieved an expansion factor of around 5-fold.

At the source, the beam (488 nm) is emitted with a diameter of 0.7mm. As per the schematics of the illumination arm, the beam diameter undergoes expansion following the beam expander of magnification x2. From here, with a diameter of 1.4mm, relay optics are used to minimise divergence throughout the optical path.

Reaching the 4f periscope system of focal lengths 100mm and 125mm respectively, the beam undergoes a second magnification of x1.25 resulting in a beam diameter of 1.75mm. Using the following relations, the theoretical beam waist could be calculated (Olarte et al., 2018).

$$w_0 = \frac{2f\lambda}{\pi D}$$

$$R_{axial} = 2w_0$$

Where w_0 represents the beam waist, f represents the focal length of the illumination lens, D represents the diameter and λ represents the wavelength. Thus, the theoretical beam waist of the system is 15.2µm, producing an axial resolution of 30.4µm. When considering the sample has already undergone an expansion factor of 5. The effective resolution of the tissue is theoretical-6µm.

Guiding and directing the beam path around the imaging chamber is provided by kinematic mirrors mounted via three adjusters (Thorlabs KS1), facilitating alignment across the three axes by ±4° of angular adjustment. The precision mounts enable a reduction in drift over long periods by lock nuts. Since the optical path must be tailored from the sample outwards, the beam walk can be done from the laser source towards the sample. Two successive mirrors enable the appropriate degrees of freedom to create a compact and easily correctable optical path, accessible to the user. Generally, the mirror placed first in the beam path is largely responsible for the positions of the laser beam whereas the second mirror serves mostly to adjust the angle in the tilt of the laser path yet both mirrors contribute to the overall positioning and tilt of the laser path.

In order to coordinate the alignment of the output beam whilst doing the beam walk, precision pinholes were implemented. They typically are arranged in two successive

positions where the first serves for positioning the beam at the correct height while the second contributes in making sure the beam isn't travelling at an angle and is parallel to the optical table.

8.5 Detection

High resolution detection

Since this set-up is primarily designed for imaging thick samples, a long working distance objective had to be included to be able to image adequate axial depth. An objective of working distance 29mm in air, extending up to an extra 5 mm in water, (Olympus XLFLUOR4X/340, 0.28 NA, x4 magnification) was used with infinity correction

An infinity objective is an objective that collimates light to a tube lens when then re-focuses the light towards the sensor. While the light is collimated, other elements, such as filters and mirrors, can be placed in the beam path without disturbing the magnification or light quality therefore optimising the use of the space known as the 'infinity space', shown in figure 8.5.1. Infinity-corrected objectives are each of a fixed tube lens focal length, depending on the brand, which governs the focal length of the tube lens in order to have zero magnification effect or to implement magnification in the detection path.

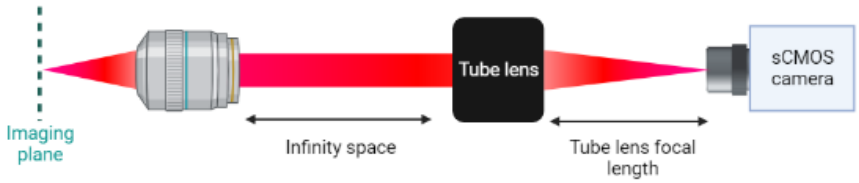

Figure 8.5.1 Infinity-corrected objective

The tube lens offers flexibility in changing the magnification and therefore field of field of the detection optics if mounted in a flexible manner such as a cage system.

Maintaining the ability to modify the optics, the tube lens is mounted into a cage system providing the flexibility to change the tube lens of the system to alter the effective magnification. This is calculated using the following (Thorlabs):

$$Effective\ magnification = Design\ magnification\ x\ \frac{focal\ length_{\ tube\ lens}}{focal\ length_{\ design\ tube\ lens}}$$

Tube lens combination	**Tube lens effective focal length**	**Effective focal length with infinity corrected objective** **- 4x magnification** **- 180mm design tube length**
2 x achromatic lens f = 180mm No distance	90mm	2x
2 x achromatic lens f = 150mm Distance = 130mm	132.35mm	3x
2 x achromatic lens f = 180mm Distance = 120mm	135mm	5x

sCMOS with rolling shutter

The scientific CMOS is able to acquire in rolling shutter and global shutter mode. This can be selected by the user for optimising image quality. For expanded samples, much signal is lost during the expansion process and therefore a high exposure time is favoured in obtaining signal from each possible spatial coordinate in the sample.

sCMOS (scientific complementary metal-oxide semiconductors) are a sub-sensor of CMOS image sensors which are widely implemented in observation scientific instruments for multi-pixel detection. They are able to run in two modalities of electronic shutters, 'global shutter' or 'rolling shutter' depicted in figure 8.5.2. The choice between the two allows the user to control exposure time and, consequently the volume of photos detected by the sensor. The pixels that receive the photons quantises this into electrons to output a digital signal value.

The entire sensor remains open in global shutter mode and therefore able to collect a greater quantity of photons. The rolling shutter, however, opens individual lines with a time lag which then generates the final image with a reduced amount of photons. A camera with 2048 rows (2048 x 2048 sCMOS camera) opens the first row at 0 seconds and 2.048ms later will open the final row if there is a 10µs exposure time for each row; this is known as the time frame. For moving samples, this 'delay' in time can be problematic since a sample can move in between this moment.

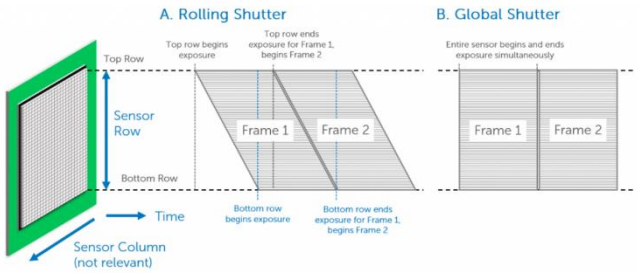

Figure 8.5.2 Modalities for the readout timing of a sCMOS camera.

The x axis represents the time of acquisition while y represents the readout. The rolling shutter begin by only opening the top row of the acquisition and continuing this way, rolling down to the last row, continuing in this way. Conversely, the rolling shutter opens each row of the sensor at the same time and continues this way for the entire acquisition.
Adapted from *Photometrics*
From https://www.photometrics.com/learn/advanced-imaging/rolling-vs-global-shutter

Strategically choosing a sufficiently small exposure time results in a line-shaped confocal region of open sensor lines that functions as a moving detector when synchronised with the illumination beam and the open detector lines. Termed line-scanning confocal detection, this elegant approach can be easily implemented without other mechanical devices to achieve enhanced optical confocality perpendicularly to the direction of the rolling shutter (Baumgart & Kubitscheck, 2012). This, in turn, achieves greater contrast and SNR in the images.

Low resolution detection

Large samples at high resolution require incredible amounts of data (include values here between high resolution 10-micron step size and low resolution 200-micron step size). A second detection arm was implemented to serve as a guide in order to take a full sample acquisition at low resolution in order to determine the areas in which fluorescent signal was located and then proceed with the higher resolution detection for the specific area.

Indeed, the concept of hierarchy imaging is very useful when working with large tissue volumes since data management can be problematic. Optimising the useful data acquired is feasible when the location of the signal is known. The acquisition can be structured in order to store data from pre-defined voxels.

The design of this detection arm is very simple. Two achromatic lenses, of focal lengths 200 mm and 200 mm respectively, combined to form the objective lens with an effective focal length of 100 mm through which the photons are collected, the equation of which is below (Sharma, 2006).

$$\frac{1}{f_{net}} = \frac{f_1 f_2}{f_1 + f_2}$$

This had to be long enough so that an object in the imaging plane would be relayed on to the sensor with no effective magnification. At the furthest distance from the imaging plane, the focal length was selected to be half of the necessary distance, ~84mm from chamber entrance to the focal plane as depicted in figure 8.5.3.

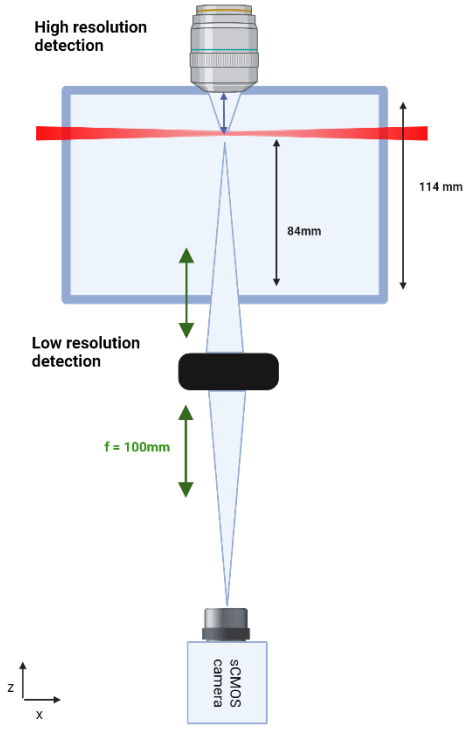

Figure 8.5.3 Low resolution detection arm.

Two combined double achromatic lenses were used as a lens to collect photons in a plane at a distance of double the effective focal length, each focal length represented by a green arrow. The scientific CMOS sensor is therefore located at the same distance in order to cause no effective magnification. Since this is purpose of this detection arm is to produce a quick, low resolution and low data acquisition, maintaining a zero expansion factor is necessary. A filter mount directly precedes the camera in order to selectively filter out unwanted fluorescence.

Figure 8.5.3 shows the general scheme of the detection arm through which no magnification is implemented through equal positioning lengths between the sensor (Alkeria CO12S-M CMOS) and the imaging plane to the lens through which detected photons are collected. This system is mounted as a cage system so that alignment and spatial positioning remains fixed and can be easily covered to shelter from the background. Finally, a filter mount is placed directly in front of the sensor entrance in order to selectively detect photons of known wavelengths.

8.6 Control software

Galvanometric mirror alignment software

Facilitating alignment ease, a multiple-analogue output pin DAQmx board was used to control the galvanometric mirrors electronically via c-programming commands, utilising National Instruments library, by a custom made programme. The programme features the ability to adjust the tilt of each individual mirror via amplitude adjustment of the analogue

output signal. Since a single output channel is dedicated to each mirror, individual commands can be modified to have full autonomy in aligning each of the four mirrors. All composed in one task, the software is simple to use, with a coherent user interface.

Microscope control, data acquisition and post-processing

Complete microscope control of all components in coherent modality is conducted using SPIMlab software (https://github.com/lens-biophotonics/SPIMlab), a data acquisition and control software for LSM. The software allows the user to modify resolution through control of electrical components as well as selecting the parameters to acquire since some biological samples require precision alignment and selectively imaging dimensions. The software acquires voxels of user-defined volumes.

Voxels of data acquired are then processed using ZetaStitcher (https://github.com/lens-biophotonics/ZetaStitcher), a tool that is designed to stitch large volumetric images from LSM. Voxels are stitched together to achieve a 3D volume of the sample.

Chapter 9 Results

9.1 Characterising the effective magnification of the system

As aforementioned, the magnification of the detection system can be modified through the implementation of different tube lens focal lengths. When conducting the acquisitions for calibrating the system, the theoretical magnification was x2.

In measuring the effective magnification, a sample was selected with distinguishable features and traced throughout displacement of known physical values in the sample dimensions in the x and y plane, an example of this feature displacement is shown in figure 9.1. This can also be done using fluorescent beads. To this end, the stages are programmed to move in suitable step sizes and this is trusted to be accurate since each position can be physically controlled through manual analysis.

Each position of displacement in the sample plane has a corresponding position on the camera sensor of known pixel size (6.5µm) and therefore the factor by which these positions differ from each plane represents the factor of expansion. If the stage is moved by 1 mm but the position on the sensor moves by 2mm, the factor of difference and therefore the expansion factor is x2. This method was repeated using various features in multiple samples with x and y movement and an average magnification value resulted as x1.9 ±0.09.

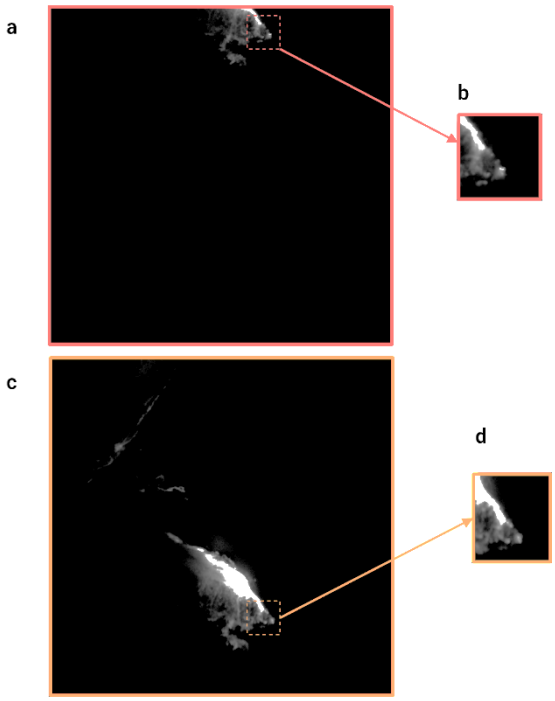

Figure 9.1 Feature displacement at two extremes of the field of view.

Images (a) and (c) show the field of view when a feature in a sample is moved from one y-extreme to another. Between these two positions, smaller steps are taken in y to precisley trance the sample to increase the precisition. Meanwhile the physical movement noted alongside the pixel shift used to calibrate the effective magnification. Insets (b) and (c) show close ups of the feature to visualise the structure as its moves through the y-plane.

Δx on sensor (pixels)	Δx on sensor (mm)	Δx physically (mm)	Magnification factor
1508	9.8	5	1.96
1474	9.58	5	1.92
1307	8.5	5	1.7

Δy on sensor (pixels)	Δy on sensor (mm)	Δy physically (mm)	Magnification factor
1424	9.26	5	1.85
1434	9.32	5	1.86
1428	8.28	5	1.86

9.2 Characterising the beam waist and axial resolution

Both illumination arms were measured individually to have precise characterisation. Often, totally transparent materials can be imaged with a single illumination arm since scattering is at a minimum and to avoid bleaching during long acquisitions.

A single frame was taken of each beam waist as shown in figure 9.2 (a) as part of figure s below. Images are taken in a solution of Fluorescein (5%) in order to maximise signal. The intensity profile along the beam thickness is analysed, figure 9.2 (b) in order to produce the Gaussian profile curves of the beam's intensity. Indeed, the most intense portion of the curve represents the beam waist in which the photons are condensed. Knowing the pixel size on the camera (6.5µm on a 2048x2048 sensor) and the effective magnification of the detection system (x1.88968), allows the conversation of the beam width to the sample plane, the true thickness values a given in the graphs in figure 9.2 (c).

From this data, the full-width half-maximum (FWHM) values were calculated to be 26 µm and 22.5 µm for the left and right illumination beams respectively. The following equation from Gaussian beam propagation relations was therefore used to calculate the resulting beam waist (Müllenbroich et al., 2015).

$$2w_0 = \frac{FWHM}{\sqrt{2ln2}}$$

Practical measurements indicate subsequent beam waists of 11 µm by the left illumination arm and 9.6 µm by the right illumination arm. Therefore, the measured axial resolution of the system falls in orders of 20 µm

When employing samples at maximum expansion of~x5 using the modified eMAP protocol as described in Part 2, the effective resolution of the system moves to the order of~4µm. Many detailed structures in biological tissue, such as dendrites, somas and axonal projections, are in the order of several micrometres, allowing the system to resolve and acquire the fine detail in axonal morphology and projection extending through the entire mouse brain.

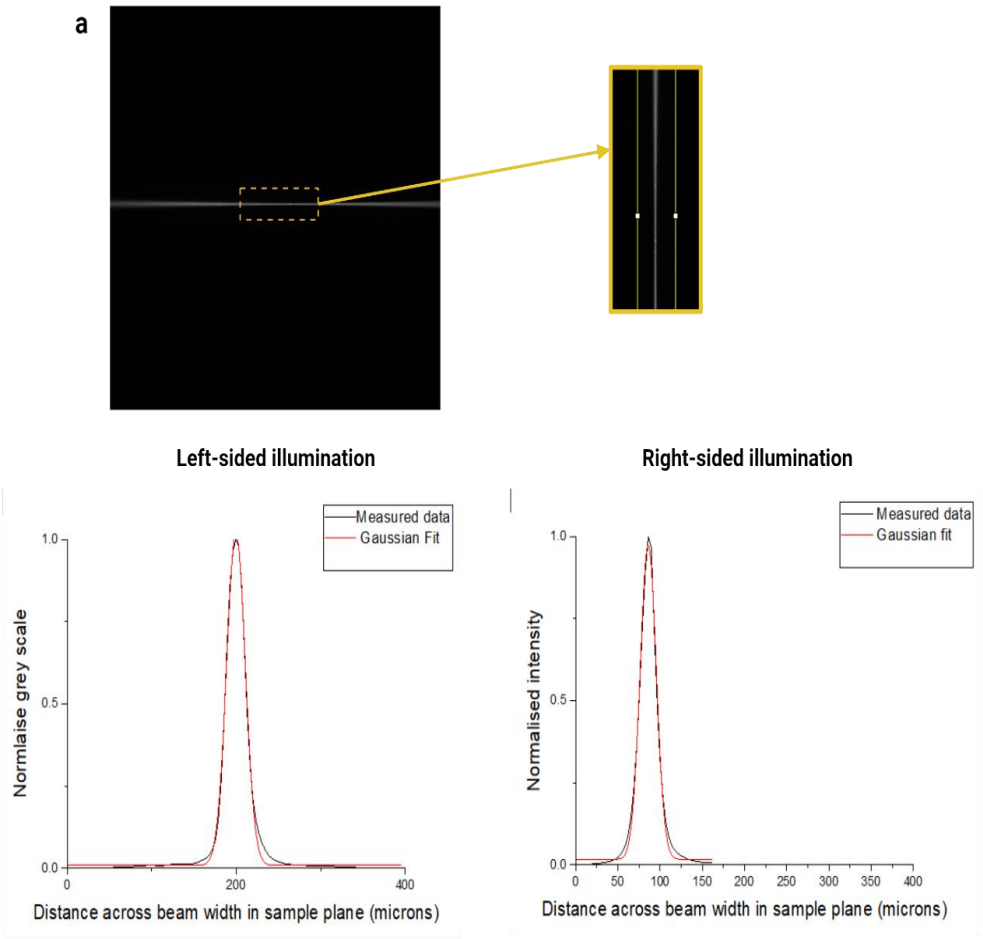

Figure 9.2 Beam waist measurements for characterising axial resolution

Inset (a) displays the frame of the field of view of a non-scanning beam used to form the light sheet. An intensity profile is taken along this region (b) in order to produce Gaussian fits of the intensity profile for beam waist calculations (c).

9.3 Point spread function and lateral resolution

In order to quantify the further resolution of the system, the point spread function was taken in the lateral and axial directions. Ultimately, a light sheet with a larger thickness than that of the axial point spread function governs the overall axial resolution.

eMAP hydrogel was prepared using standard procedure diluted with fluorescent beads of diameter 200 nm (TetraSpeck microsphere, fluorescent blue/green/orange/dark red) at concentration 1:5000. Since the refractive index of most expansion microscopy gels and tissue-gel hybrids is that of water (1.33) this provided an optimum solution to obtain an accurate result.

Multiple intensity profiles of the beads were taken in the x and y axis, forming the lateral plane, see figure 9.3. Using the full-width half-maximum method, the average was taken from various bead positions in the gel with a standard deviation provided among the data. In the lateral plane, the point spread function resulted as 9.95 ±2.7. Furthermore, when combined with the expansion factor (~x5) of the protocol describes in this thesis, the effect resolution in the order of 2μm.

Lateral PSF	
Fluorescent bead	FWHM
1	11.48
2	6.23
3	7.46
4	12.7
5	8.02
6	6.82
7	12.8
8	9.69
9	13.71
10	10.6

Average FWHM	9.95
Standard deviation	2.71

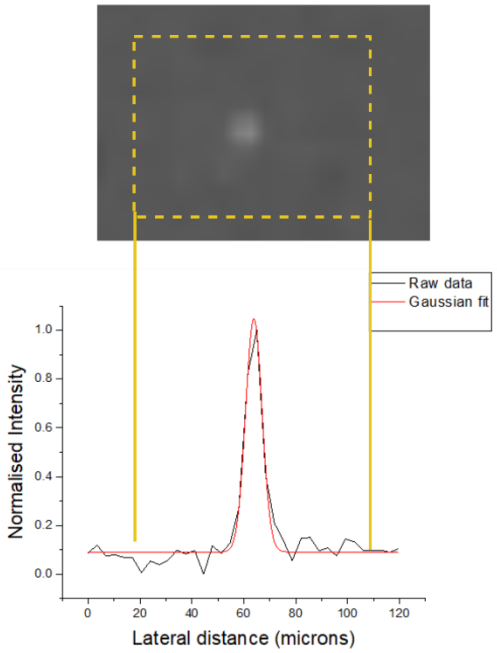

Figure 9.3 Full-width at half maximum values calculated from the data of 10 fluorescent beads

The intensity profile as a function of spatial distance of fluorescent beads was taken in the sample plane in order to calculate the intensity profile, fitted to a Gaussian profile. From here the FWHM could be found in order to approximate the lateral PSF.

9.4 Application to biological samples

The combination of the expansion microscopy technique I developed in this research, together with the custom-built light sheet microscope delivers an effective resolution of around 2 µm laterally and 4 µm axially. Together, these novel tools can be used to explore fine anatomy within biological samples since both the expansion microscopy and light-sheet microscope can be easily replicated efficiently in terms of cost and availability.

In proof of principle, I prepared samples and acquired image data of the fluorescently-labelled anatomy. Data presented in the results of Part 2 had also been acquired on this optical set up which was noted.

Here, I apply the technique to a whole brain sample labelled with a viral injection of fluorescent marker, tdTomato expressed in the soma. The expanded brain was imaged as a whole, where the injection displays a high degree of fluorescent signal. In figure 9.4, I highlight regions, inset a, where optical segments of neuronal trajectories are labelled in the sample, with adjusted contrast for visibility since the injection sight saturates other stained regions in the sample. Inset b of the figure demonstrates the contrast in signal as the highest signal is situated around the injection site.

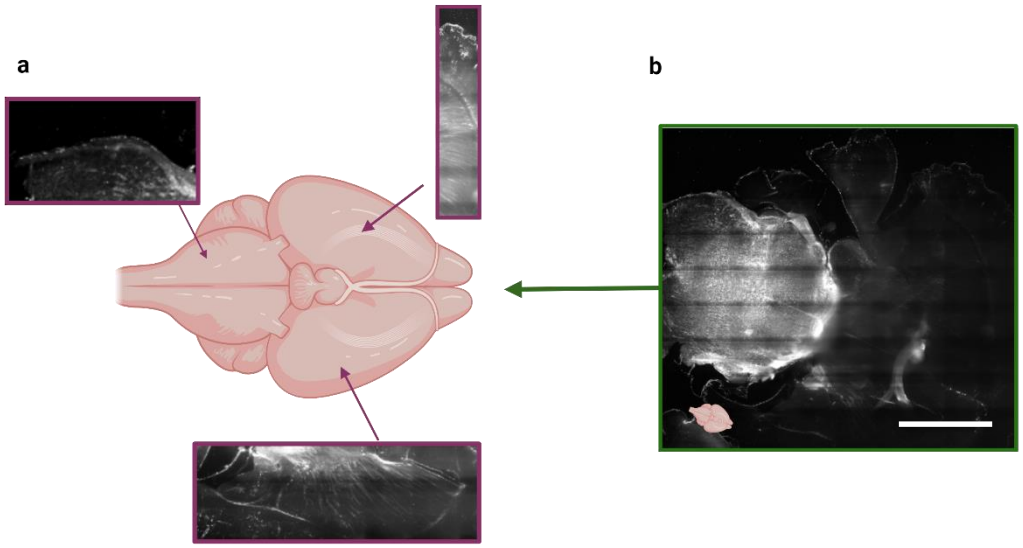

Figure 9.4 Full, intact brain scan of a mousse brain expanded using the modified eMAP protocol and imaged on the customised light-sheet microscope

Features, neuronal projections and morphology, were able to be visualised within the tissue volume. Segments of different optical slices are shown in the magenta boxes as the contrast is modified for better visualisation. An image of an optical slice is also shown (green) with the orientation where the fluorescent signal can be seen most intensely at the injection site. Scale bar = 1mm.

Part 4 Optimising and maintaining a customised Light Sheet Fluorescence Microscope for routine imaging

Chapter 10 Experimental setup of routine analysis of human brain tissue

During my PhD I also worked on optimising and maintaining a dual-sided inverted light sheet microscope that was routinely used to perform analysis of human brain tissue for large-scale imaging of full brain regions. In the following paragraphs I will present the ways in which I troubleshoot issues arising in the optical setup, how to diagnose them and ultimately improve image quality.

With the goal in mind of brain mapping, this set-up has been applied in combination with the tissue clearing technique to image large tissue volumes of human brain tissue sectioned via physical sectioning into slices.

The features of this optical sectioning provided a means to optimise the protocol SHORT, a protocol developed with the aim of successfully clearing post-mortem human brain tissue. The protocol could be tested with its compatibility with multiple antibodies through multiplexing and four-channel imaging with the LSFM described. Multiplexing and an adequate imaging system provided images with optimal characterisation of composition in the tissue through the processing of the four individual channels.

Together with the success of the labelling and clearing protocol and the resolution capabilities of the LSFM, a comprehensive cell census of the human brain tissue was gathered to form a proteomic analysis.

10.1 Customised dual-sided inverted light sheet fluorescence microscope

A customised light sheet microscope previously used for routine imaging of fixed and cleared slices of biological tissue, particularly the mouse brain, labelled using

immunofluorescence techniques using a range of fluorescent markers. To this aim the design features multiple excitation wavelengths 405nm, 488 nm, 561 nm and 638nm (Cobalt 06 series).

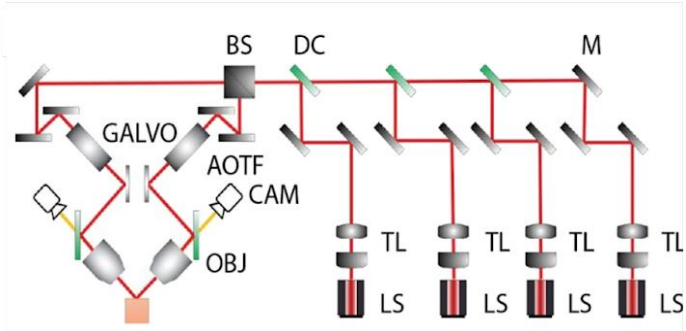

Figure 10.1.1 Schematic of the light-sheet microscope apparatus

Light source (LS), telescope (TL), mirror (m), dichroic mirror (DC), beam splitter (BS), acousto-optical tunable filter (AOTF), galvanometric mirror (GALVO), camera (CAM) and objective (OBJ).
Adapted from (Costantini et al., 2023)

The illumination optics, schematically represented in figure 10.1.1, begins with the four laser sources followed by individual beam expanders in order to obtain the same beam diameter for each channel. Forming one optical path, the lasers are directed to meet where one laser line is produced of the four individual lasers. Here, the laser path is guided to an acousto-optical tunable filter (AOTF), a device computationally controlled that effectively tuned the wavelength output and filtering those which aren't desired in order to enable a user-selected illumination wavelength. AOTF provides enhanced spectral control in which the user is able to modulate both the wavelength and intensity governing the illumination pathway without manual alterations. The foundation of this design is of an acousto-optic modulator yet, rather than power modulation, the wavelength is controlled via applied radio frequencies.

The AOTF is placed in the illumination path where 2 or more laser beams attenuate. If a sinusoidal input signal of fixed frequency is applied to the modulating device, only a small

range of optical frequencies are able to pass through diffraction as they fulfil a phase matching condition for both optical and acoustic waves. This change in acoustic frequency causes an alteration in the diffraction properties of the AOTF facilitating the tuning of wavelength.

To fulfil the operational principle, AOTF devices are typically made using specialised birefringent crystals, typically tellurium dioxide or quartz anisotropic crystal, selected due to their interaction with acoustic waves. A piezoelectric transducer bonds to this crystal which generates a high-frequency acoustic, vibrational wave that travels through the crystal which occurs as a response to the application of an oscillating radio frequency. Serving as a transmission diffraction grating, the induced acoustic wave periodically redistributes the refractive indexes through the crystal which consequently deviate some of the incident light into a first-order beam. The wavelength diffracted through the crystal is modified through the change of the frequency that comes from the transducer. In terms of relative intensity, the power (amplitude) of the signal determines this.

The benefit of this is to maintain a readily aligned system and to remotely control the imaging parameters without physically modifying the optical pathway, the excitation wavelength being remotely selected through the control software. The output beam then meets a galvanometric mirror that drives a digitally scanned beam.

Here, the illumination path joins the inverted section that serves also as the detection pathway. The inverted dual illumination-detection pathway is raised on a tilt of 45° from the optical table. As the beam enters this section of the illumination pathway a dichroic mirror, see image a, facilitates the reflection of the illumination path way towards the illumination objective (LaVision Biotec 12x NA 0.53, with a dipping cap for aqueous buffers 1.42 – 1.48) and thus projected on to the sample in the form of a digitally scanned light sheet. Once exciting the fluorescent markers in the sample, the emitted emission photons are collected by the second illumination-detection arm, orthogonally mounted to the illumination plane, 45° from the optical table. Once reaching the dichroic mirror, the emission photos are able to pass through and reach the detector (Hamamatsu Orca flash 4.0). In the infinity space, between the objective tube lens a motorised filter wheel (Thorlabs FW102C) is placed allowing remote control of the detection filter since the system is built to detect photons of four different emission spectra therefore strong bandwidth filters are necessary in the case that a sample is labelled with multiple filters.

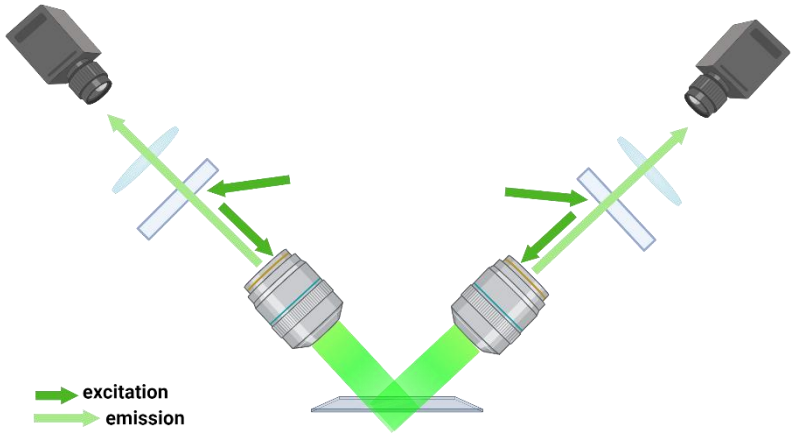

Figure 10.1.2 Dual-purpose illumination and detection arm schematic.

Illumination light, previously scanned by a galvanometric mirror prior to reaching this section of the illumination pathway, is reflected towards the sample by a dichroic mirror through projection through an illumination objective. The emitted light from the sample is then collected by the objective where the now red-shifted emission wavelength transmits through the dichroic mirror before reaching the camera. The system allows one to simultaneously illuminate the sample with 2 wavelengths where one objective serves to illuminate and the second serves to detect. The opposite is therefore employed for the second illumination channel.

Optimisation of system characteristics is often at the forefront of design. Having the dual-armed illumination-detection allows the user to simultaneously image in two different excitation channels, each of the two objectives illuminating at different wavelengths while the emitted photons are collected by the second respective detection arm increasing acquisition time by a factor of two. A single sample can therefore be prepared using multiplexing in which four channels are utilised; one for each wavelength channel features in the LSFM. Reducing both the imaging time, the property of dual-channel imaging allows the four channels to be acquired during the time required for two.

The sample is mounted at a 45° angle from the light sheet in a sample chamber that lies parallel to the optical table due the samples being thin, flat slices of tissue; the chamber is

filled with refractive index matching solution. An imaging chamber is able to hold samples mounted in standard-sized cover slips which is then filled with the refractive index matching solution appropriate for the sample in question; various clearing techniques are suited to various solutions. The objectives are able to enter into the imaging chamber from above towards the sample plane, enhanced by the dipping cap selected for the medium, reducing any refraction effects. Each objective is mounted on a motorised stage (Physik Instrumente L-series) through which the user can position the objective to appropriately fit the working distance of the objective to the imaging plane where the sample is. Similarly, the sample chamber is mounted on three stages able to translate the sample through each of the three dimensions, respectively x, y and z. Each of these degrees of freedom enhances the ability to align the working distance of the objective to the desired sample plane providing an increased range in the dynamical variety of biological samples that can be imaged. The modification of the objective tube lens, the field of view can be adjusted in order to accommodate thicker tissue slices by de-magnifying the detection system and therefore increasing the field of view.

Due to the untraditional nature of the light sheet-to-sample orientation, the light sheet penetrates through the sample at an angle of 45° and therefore illuminates diagonally through the thickness of the slice, see figure b. As the entire thickness of the slice is visible in a single field of view frame, increased axial spatial information is gained while moving only through x and y during acquisitions, see image 10.1.3. Traditional light sheet microscopes are generally limited in the axial resolution, typically featuring greater lateral resolution. In addressing this limitation, this configuration provides increased spatial information towards isotropic resolutions.

SPIMlab software is also used here, see Part 3, as the acquisition software as well as Zetastitcher in order to process the images. Each voxel must be transformed in order to be subsequently stitched to create maximum intensity projections of the entire slice of tissue. The sample is moved through the x-axis through which a row is acquired, the sample is then moved through the y-axis where each row starts from. The processing software first creates TIFF images of the fused axial data as shown in figure 10.1.3 (b) of figure b. Since the reference system, with respect to the microscope, is different from that of the samples prepared in the lab, the images must be transformed. The image stacks are acquired at a 45° whereas the end result generates an image seemingly acquired orthogonally. Thus, displaying the features through the thickness in higher resolution. Figure 10.1.3 (c) provides

an image of the entire sample as a maximum intensity projection as a collective of the axial information.

The voxel-size resolution is 0.55 x 0.55 x 3.3 μm^3 that, after post-processing, results in an isotropic resolution of 3.3 μm^3. This resolution provides the grounds to resolve neuronal subtypes as well as the morphological features of the soma in the respective subpopulations.

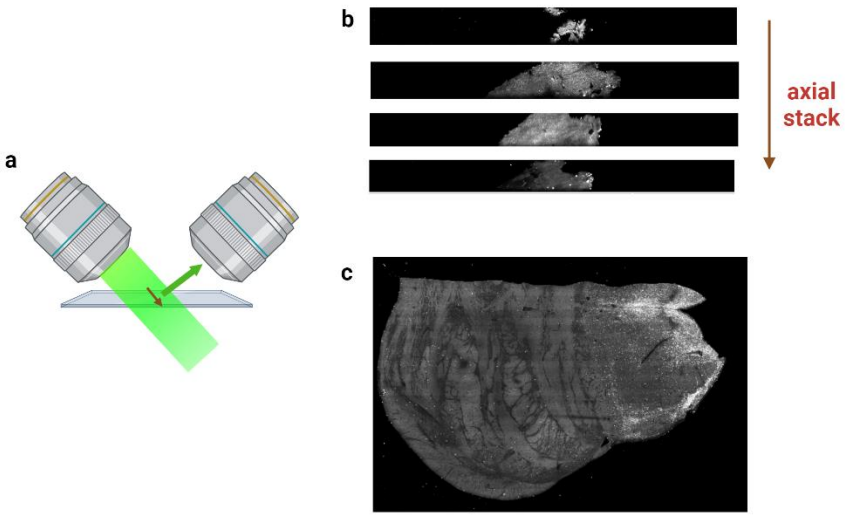

Figure 10.1.3 Image acquisition through to final processed image.

Due to the nature of the configuration, axial information of the final image is given through a singular field of view. The red arrow shown in inset (a) and (b) represent the direction of this axial information through the thickness of the sample. The initial processing steps create rows of the image through which one can scroll through the axial projection as shown through the red arrow. These projections are finally stitched together to form a maximum intensity projection image of the entire tissue volume as shown in figure x of a slice taken from human brain stem tissue.

Finally, the system is able to be remotely controlled therefore samples are pre-mounted in an imaging chamber. Until now, 2 samples are able to enter at one time. The user must simply establish the dimensions of the samples within the realms of the stage locations which can then be inserted into the software for the microscope control. This allows one

to effectively limit the data field to where the sample actually is located, as well as having flexibility through initiating acquisitions remotely.

10.2 Sample preparation

The four-channel microscope is purpose built for multi-channel imaging. The biological aim therefore is to achieve molecular specificity in multi channels in order to draw as much spatial information as possible from each sample. Combining four different fluorescent biomarkers allows one to investigate the geometrical composition of four different features in the tissue. In achieving this molecular specificity, an advanced tissue protocol, SHORT (Pesce et al., 2022) is employed to clear aged human tissue, samples notoriously challenging due to high levels of auto fluorescence. SHORT (SWITCH-H_2O_2- antigen Retrieval TDE) is a refined tissue clearing procedure implementing standard histological treatments such as conventional TDE buffers along with the preservation of tissue ultrastructure employed by the SWITCH protocols (Costantini et al., 2015). The protocol is characterised by its ability to use multiple molecules to label cleared biological tissue for multiple rounds. The fixed tissue is initially bleached in order to quench any autofluorescence before clearing and labelling.

Four different markers can be used with the SHORT preparation technique with each target able to be visualised through the four wavelength channels of the microscope. Once each channel has been acquired, the four images of the sample tissue can be merged, assigning an identifying colour to each channel to represent the geometrical spatial information of the specific neuronal marker. The final image therefore contains a detailed map of the architectural composition of the neuronal types within the tissue as shown below in figure 10.2.

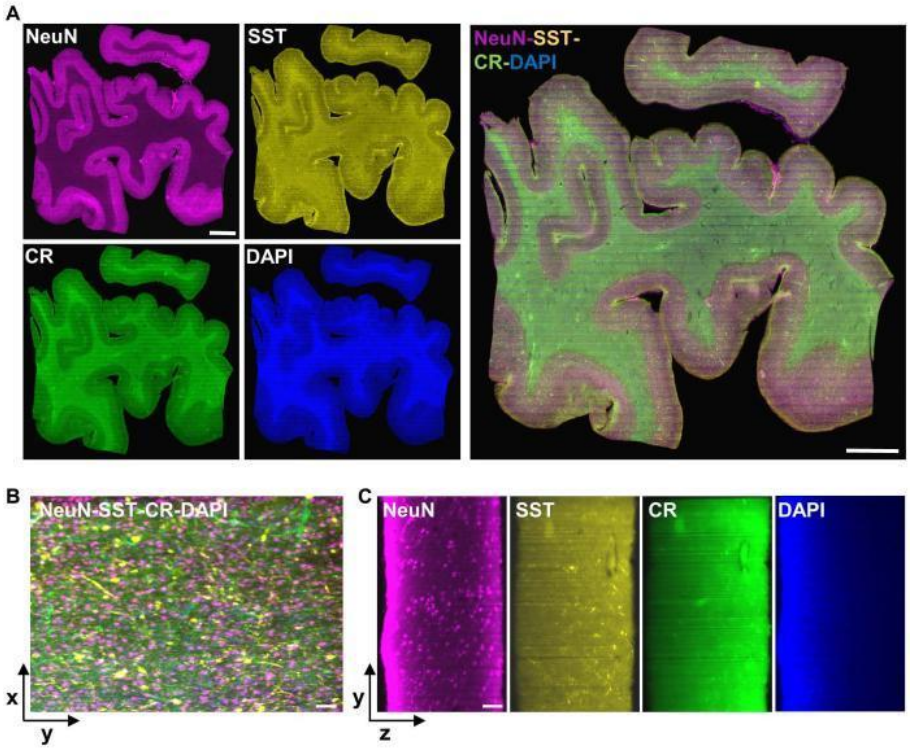

Figure 10.2. Images of a single slice following the SHORT protocol and imaged using the four-channel dual-inverted LSFM.

The representative images of a 500-um thick slab of human brain Broca's area show how the combination of the clearing and labelling technique, together with an advanced light sheet microscope can produce detailed post-processed images of the anatomy of the tissue target. Inset (a) shows the acquired, processed images taken for each channel corresponding to three neuronal markers (NeuN, Somatostatin, Calretenin) and nuclear marker (DAPI) serving as a guide. The subpopulation of interneurons are overlapped to form detailed images serving as architectural maps of the volumes in inset (b) and (d). The raw images shown in inset (c) demonstrate the uniformity of the penetrative capacities the labelling through immunochemistry while signal is diminished slightly through thickness, shown here as the z-axes.

Image taken from a recently approved article produced by this research group: Di Meo, D., Ramazzotti, J., Scardigli, M., Cheli, F., Pesce, L., **Brady, N**., Mazzamuto, G., Costantini, I., Pavone, F. S. Optical Clearing and Labeling for Light-sheet Fluorescence Microscopy in Large-scale Human Brain Imaging. *J. Vis. Exp.* (Pending Publication), e65960, In-press (2023).

10.3 Optimisations and troubleshooting during large-scale, long-duration acquisitions

This advanced optical set-up can be employed in the data and imaging acquisition of large samples, sectioned into slices (up to 500-um of thickness) and imaged individually. Since the volumetric dimension of the human brain, the acquisition sessions can run for multiple weeks at a time with 5 days of imaging where the night time and weekends are dedicated to processing the large data.

Continuous monitoring of data is essential during long-duration imaging. To be discussed are possible implications occurring due to a system in full-operative mode for long time periods. If issues go unnoticed, the consequence is that precious samples must be re-acquired, in turn increasing the likelihood of bleaching and reduced signal. In reference to this particular system, if all four channels are used, an error in a single channel's image requires the re-imaging of all four channels since the images must be taken with exactly the same coordinates to achieve overlapping images, in terms of shape and dimensions, in all four channels. Indeed, slight discrepancies can occur in a handled sample, during mounting and remounting in-between acquisitions. Furthermore, given that the optical system is mounted on an inverted breadboard, modest arbitrary shifts can occur, requiring the re-adjustment and re-alignment. In this case, all images should be completely taken or in the case of being incomplete, the four channels should be acquired again.

The remainder of this chapter will provide details of the steps that were taken during my doctorate to optimise parameters to benefit the data acquisition parts of this pipeline in terms of image quality as well as parameters to enhance post-processing through the optical system. Moreover, presented are indicative methods to identify the source affecting image quality and therefore troubleshoot issues as they arrive. Heavy use of any system requires particular maintenance and understanding of the individual components.

Preparing the system for long, stable and continuous imaging sessions

In maintaining and enhancing system parameters, each component should be assessed. If utilising the four-channel feature, the stronger illumination arm can be defined and subsequently implemented. To understand this and measure, components in the optical path were considered. Following individual beam expansion, the lasers are then aligned to the same optical path where they reach a beam-splitting cube serving to form two identical illumination arms. Indeed, a beam-splitting cube (Thorlabs BSW10R) capable of 50:50

division of the beam through transmission and reflectance in the appropriate range had been implemented. In review of the supplier transmission and reflectance transmission curves, displayed in figure 10.3.1, one can comprehend the superior direction of power and verify this through measurements using a power metre.

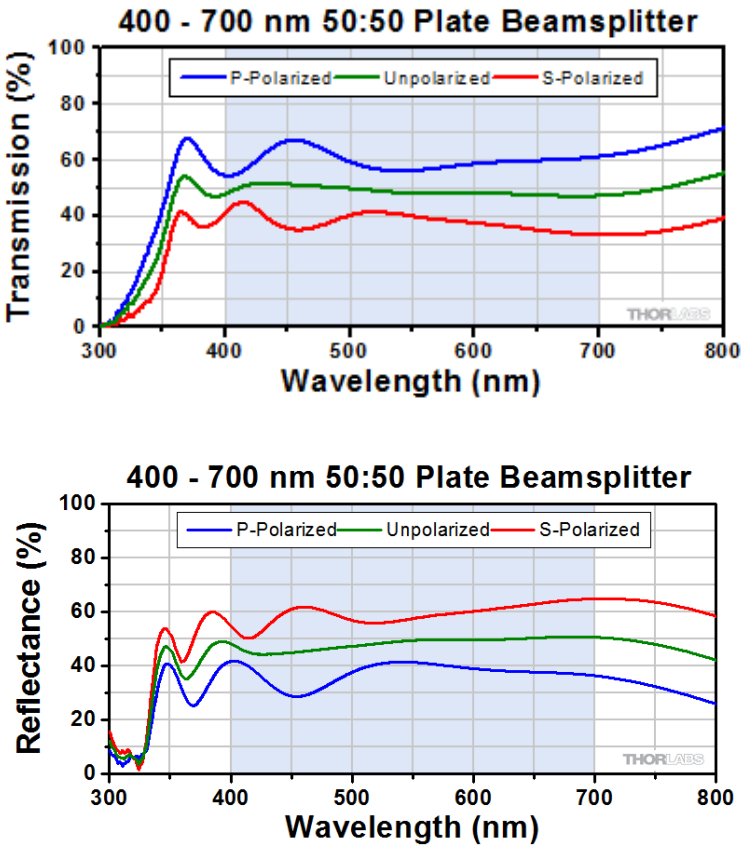

Figure 10.3.1. Transmission curved for 50:50 beam splitter (Thorlabs BSW10R).

The beam splitter is characterised for wavelengths of 400 – 700 nm, the range of the four illumination channels used in the set-up. Each wavelength has a slightly better power transmission in the reflected or transmitted directions. This characteristic can be exploited in choosing a 'stronger' illumination arm for each channel in order to gain better signal for the same label of power from the source.

Adapter from *Thorlabs*

From https://www.thorlabs.com/newgrouppage9.cfm?objectgroup_id=4807&pn=BSW10R

Selecting the path through which most power attenuates prevents the user from unnecessarily increasing the initial power, preserving the longevity of each laser source. Considering 488 nm on interacting with the beam-splitter with unpolarised light, less than 50% is reflected while slightly over 50% is transmitted meaning the sample would receive more signal from the illumination arm constructed of the transmitter power than that of the reflected light. This would therefore be selected as the stronger, more optimal illumination arm.

In reviewing the results of polarised light with transmission and reflectance, the power reaching the sample can be further optimised by strategically focusing polarised light on to the beam-splitter, characterising the wavelengths for each polarisation arm; two p-polarised channels for optimal transmission and 2 s-polarised channels for optimal reflectance. However, in cases where the same channel is used for both illumination lines, unpolarised light adheres most to 50:50 transmissions: reflectance.

Prior to starting acquisitions, a task remotely controlled, parameters for each channel can be optimised to achieve the highest image quality possible with the system. Since the AOTF serves to transmit the desired illumination channel, the positioning of the galvanometric mirror used to generate the light sheet can be configured. The offset serves to adjust the tilt of the laser beam of the light sheet so that it is effectively located in the detection plane, overlapping in parallel to the field of view in the sample plane while the delay enables the user to effectively align the scanning motion with the rolling This has been found to vary slightly from laser to laser. The amplitude of the galvanometric scanner also aids in achieving a light sheet over dimensions large enough to cover the field of view.

Figure 10.3.2 provides two samples, both human brain tissue, where the first slice is images without channel-specific optimisation parameters and the second slice is images using parameters defined for the specific illumination channel. Figure 10.3.2 (a) shows both images in their entirety after post-processing in which the first image creates the effects of stripes, artefacts characterised by lack of illumination homogeneity in the field of view. When enlarged, figure 10.3.2 (b), these stripings are significantly reduced due to managing the parameters to create a uniform field of view.

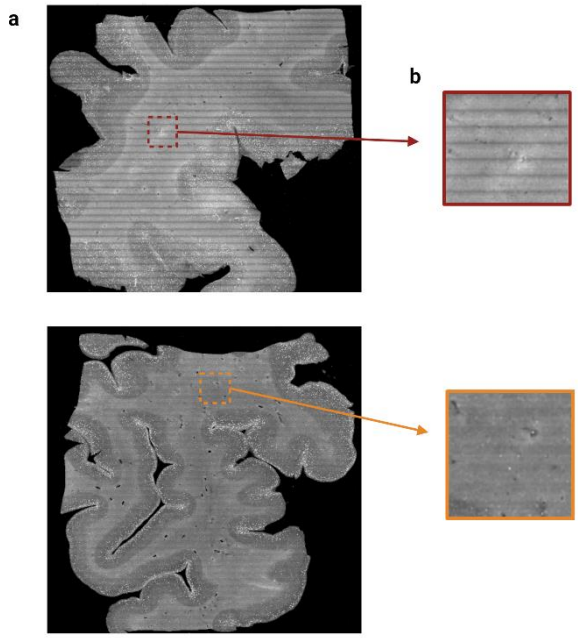

Figure 10.3.2 Two tissue slices, the top images with general imaging parameters for all channels, while the second image is generated from channel-specific parameters

Due to the slightly differing characteristics between the imaging channels, optimising the galvanometric parameters for each specific channel can generate more homogenous illumination across the field of view, in-focus samples features and in turn, higher image quality.

When these stripping effects are consistent in each acquired row, it can be determined that this effect is consistent in each tile rather than a physical artefact in the sample or imaging optics causing shadowing effects. Shadowing effects create much more sporadic artefacts in the images.

Binning

Long-term imaging requires the optimisation of image quality but also temporally in terms of acquisition and processing time. Large amounts of data are consequently acquired and processed giving rise to sophisticated data management strategies.

A way in which to reduce the acquired data and in turn, the imaging and processing time, through the imaging system is to employ the use of pixel binning on the camera. This is the process in which adjacent pixels are grouped in an image with the intensity being averaged after read out. A great benefit of this is that data is reduced by the factor of the binning where the time necessary to image is also reduced. The smaller accumulated data is therefore processed with much ease, easing the loads also on the storage system. To this end, the signal-to-noise ratio is improved as the read noise contributes to each larger binned pixel; for examples in a 2x2 bin, the larger binned pixel is comprised of four pixels and so the signal-to-noise ratio in improved by a factor of four since the result is 4:1, signal: noise. In effect, the camera is able to detect weak signals, increasing the sensitivity. A consequential drawback is that spatial information is lost since the average signal is taken over a larger area, losing geometrical specificity.

In the search to minimise data contribution via the imaging system, the effects of binning were explored. The spatial information lost in this technique had to be subtle in that essential spatial information wasn't lost, hence not meeting the goal of the data acquisition. The camera (Hamamatsu Orca flash 4.0) has 3 binning modalities; no binning, 2x2 binning and 4x4 binning. Acquiring the same part of the same sample exposed to each binning modalities allowed the comparison of the effects to be made, to assess the trade-off between reducing time and reducing spatial information. The images were taken over several rows with equal exposure times (0.55ms), laser channel (561 nm) and laser power (5mW). Figure f shows an example of the binning effects in one sample post-processing. What was found was that important features, needing to be identified in this study, were still able to be resolved at 2x2 binning since the scale of features existed beyond the dimensions of the binned larger pixel (super pixel) and by Nyquist theory, multiple details spread over many 'super pixels', the features can be clearly represented and resolved.

Each biological target has different features, most importantly the target fluorescently marked. This binning strategy must be tested to ensure features can be spatially resolved at high binning modalities. For this sample, a human brain stem with calretinin stained with a fluorophore at 561 nm excitation was used and through analysis, the binning at 2x2 was selected in order to maintain the necessary spatial information but also increasing the data acquired by a factor of 4.

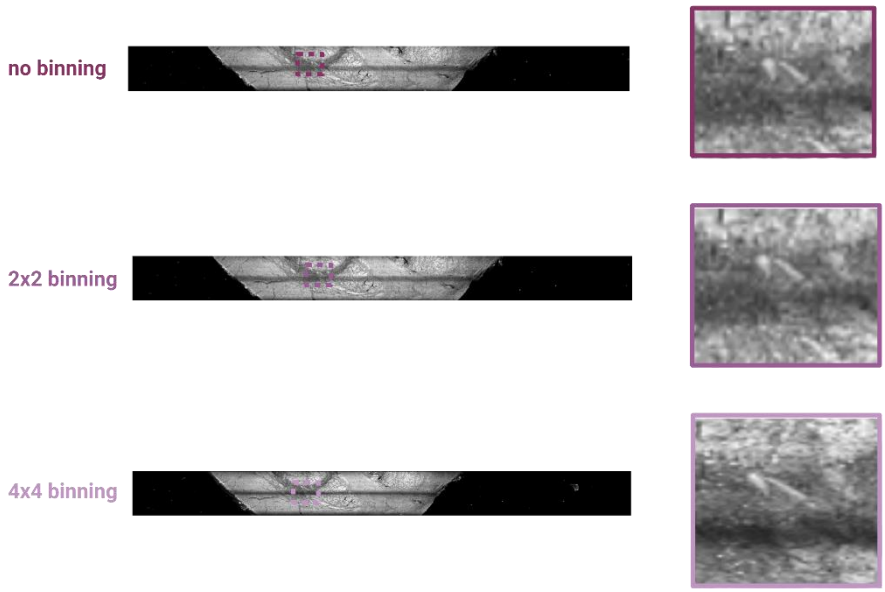

Figure 10.3.3 Representative images of binning effects in a sample.

The human brain stem slice was sequentially imaged and processed at varying binning modalities in order to assess the effects on the resultant images. When magnified, we are able to determine which 3 modality maintains the resolving ability of fine features. Increased binning reduces the imaging time, processing time and volume of data acquired is benefitted substantially with respect to no binning at all.

Sample mounting

Artefacts generated in the images that are random in nature indicate the presence of unwanted objects within or on the sample itself. Indeed, if the feature is visible across all four samples, it can be deduced that the consistency indicates its presence in the sample or on a lens within the detection optics.

Samples mounted between coverslip can sometimes be done in a way that traps small air bubbles that go unnoticed by the human eye. During imaging, these bubbles cause light to scatter and therefore not reach the fill trajectory of the beam waist and confocal parameter. Resulting are images with shadows and blurred features due to the

heterogeneous nature of refractive index since air features a refractive index lower than most cleared tissue (Müllenbroich et al., 2018).

Expanding on this, dust particles can also become logged in the imaging chamber, subsequently floating down to the surface of the coverslip, casting shadows as the light is absorbed. Moreover, the polishing of the coverslips can also see remnants of dust or tissue fixed to the cover slip. A final possibility is that dust is present within the optics itself, causing photon scattering before reaching the detector, this effect would be seen consistently between each sample and in each channel unless specific to an emission filter.

To diagnose the cause of the artefacts, the consistent or inconsistent nature is analysed. Figure r shows a representative image of a human brainstem tissue slab. The first image in figure 10.3.4 (a) displays an artefact that seemed to be inconsistent with expectations of the tissue composition. The coverslip, containing the slab, was therefore removed and re-polished. Upon re-imaging, the second image figure 10.3.4 (b) produced a similar artefact located in a different part of the sample indicating that this didn't arise from within the sample itself. An artefact of such nature, tends to arise from the material used to polish the coverslips, paying close attention to removing all remnants prior to mounting into the mounting chamber. In order to avoid tis further, the refractive index-matching solution inside the chamber should be regularly changed to eliminate chances of dust falling inside and reaching the coverslip. In combination with the SHORT protocol, 91% glycerol solution is used as a refractive index-matching solution. After 1-2 days, the solution tends to separate creating a non-uniform dilution throughout the chamber, therefore changing the refractive index with depth. Naturally, this is reflected in the images as the sample fails to be brought into focus. To speed up the preparation of the matching solution a stirring plate was introduced in the procedure in order to homogenise the glycerol and the water avoiding the production of air bubbles inside the sample.

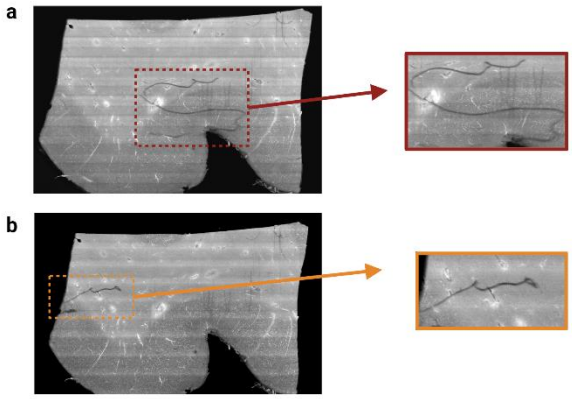

Figure 10.3.4 Physical artefacts present on the coverslip.

The same sample is images and re-polished to determine whether the polishing material has tendencies to catch to the coverslip leaving small remnants that absorb the light, ultimately affecting the final image.

Electronic malfunctioning

Malfunctioning electronic devices are incorporated in most advanced optical systems each with its own limited lifetime. Since these devices are frequently used during long-period acquisitions, these lifetimes need to be considered as possible causes to disturbed image quality.

During a particular period of acquisition, the intensity appeared to randomly fluctuate throughout the tissue on review of the post-processed image as seen from figure 10.3.5 (a) in figure g. Of the same tissue slice, these fluctuations were not present, figure 10.3.5 (b), revealing an issue solely in the 405nm channel. To further investigate this, images were acquired with the same channel and post-processing images reviewed which indicated the same sporadic fluctuations within the sample, figure 10.3.5 (c). The lack of consistency gives rise to the idea that this is caused by something independent of the sample; shadows caused by absorption by sample features would be consistent in each channel.

To troubleshoot, the power of the laser was monitored over the same period necessary for a single acquisition of one channel (~3-4.5 hours). This was done for both illumination arms to determine if this occurred in parallel indicating the issues caused by the light source. The

fluctuations were mirrored in both illumination arms in which the power often fell from that of which it was programmed to be indicating a malfunctioning laser force. In resolving this problem, we found that the laser was much more stable at higher powers however this encourages photobleaching if reaching the sample. To reduce the laser power, reaching the sample, a band-pass filter was added to the laser path between the source and target.

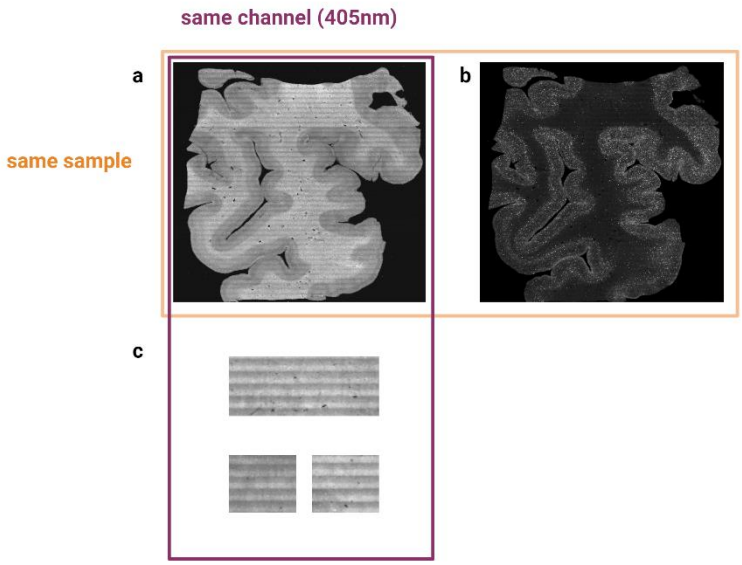

Image 10.3.5 Fluctuations in illumination intensity within a single sample.

Channel 405nm displayed varying intensities during random points in a tissue slice, inset (a), that weren't present in other channels of the same slice, for example 638nm as shown in inset (b). This was reflected in other tissues of the same channel where this inconsistent shadowing effect was produced, inset (c).

Another important aspect to obtain good images is the fact that all electro-mechanic components need to work properly. Indeed, accordingly, the electronic translational stages are trusted to move in such a way that the input values correspond to the physical values. When this isn't the case, imaging parameters are not true to those input in the processing software causing disturbed images.

A malfunctioning stage can disfigure images as those represented in figure 10.3.6. Images, such as those in figure 10.3.6 (a), were produced post-processing. The random nature of such images allowed one to rule-out the apparent issue in the software, giving rise to the theory that this disfigurement occurred during the acquisition process. Raw data of each row was analysed where the distortion was also seen in some but not other, figure 10.3.6 (b). The stage was then analysed alone, monitoring its translation over a time period through which step sizes occurred over different displacements. The malfunctioning was then diagnosed and the stage in order to solve the problem.

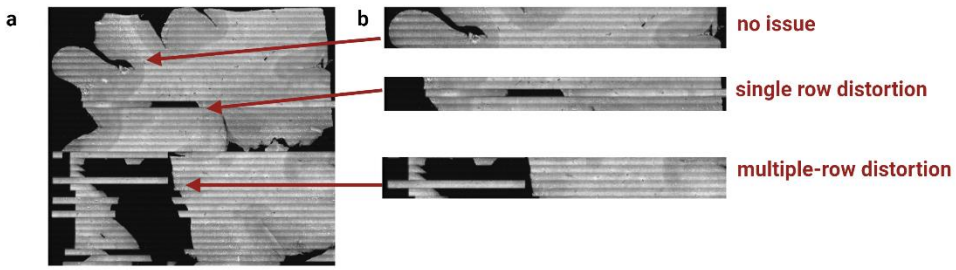

Figure 10.3.6 Tissue showing disfigurement in varying rows of the post-processed data

Despite some rows being as expected, raw data was analysed reflecting this random disfigurement in the corresponding rows, shown first in inset (a) and broken down in sub-row portions in inset (b) which ruled out the possibility of issues in the software. Upon further investigation, the translational stage was diagnosed to be malfunctioning.

Chapter 11 Experimental applications

This pipeline is not limited to the use of human brain tissue and mouse brain tissue as previously used. The principle requirements of the optical set-up are limited only by the sample form. Fluorescent imaging relies on optically transparent materials where, for mounting purposes, samples must be mounted in coverslips to be mounted and brought into the imaging plane; a working distance of 8.5 - 10.9mm depending on the incubation media.

The pipeline was applied to image human tissue in which the micrometre resolution of the system was able to effectively resolve marked features as well as determining how well the features in this range are fluorescently-marked as shown in the figure 11 (b). The post-

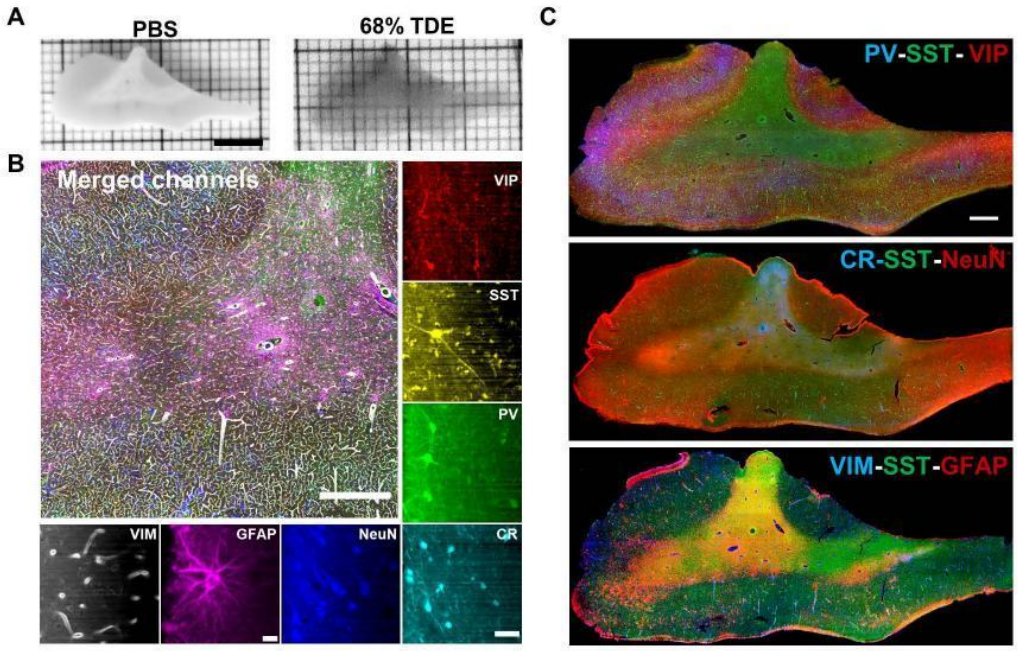

processing techniques allow the multiple channels to be overlapped to produce an image, inset c, that contains the spatial information acquired in the four channels combined.

Figure 11 Labelled human brain tissue of 500µm thickness using SHORT protocol and imaged at micrometre resolution with the customised LSFM.

Inset (a) shows the change in tissue transparency pre- and post- treatment where which both the white and grey matter undergo labelling of Vasoactive Intestinal Peptide (VIP), Somatostatin (SST), Parvalbumin (VP), Calretinin (CR), Neuronal Nuclear antigen (NeuN), Glial Fibrillary Acidic Protein (GFAP), and Vimentin (VIM). The high resolution images shown in inset (b) at a resolution of 0.55 x 0.55 x 3.3 µm were produced with the customised LSFM. Finally, maximum intensity projections of the combined data were produced of the three rounds of immunostaining; round 1 saw PV, SST and VP, round 2 CR, SST and NeuN and finally round 3 with VIM-SST-GFAP.

Image taken from a recently approved article produced by this research group: Di Meo, D., Ramazzotti, J., Scardigli, M., Cheli, F., Pesce, L., **Brady, N**., Mazzamuto, G., Costantini, I., Pavone, F. S. Optical Clearing and Labeling for Light-sheet Fluorescence Microscopy in Large-scale Human Brain Imaging. *J. Vis. Exp.* (Pending Publication), e65960, In-press (2023).

Part 5 Conclusion

Discussion

Full brain mapping of neuronal projections is a substantial challenge across the multi-disciplinary areas that contribute to this ever-developing field. Combined efforts by researchers continue to develop improved pipelines consisting of reliable sample preparation techniques, advanced imaging systems and sophisticated data managing software. Understanding the architecture of the brain is considerably one of the greatest scientific developments of our time as this knowledge opens doors to a plethora of further research in brain functionality, diseases in the central nervous system and developmental biology since each of these research lines requires concrete knowledge of the building blocks through which mechanisms occur.

The study of the central nervous system is a complex investigation due the intricate nature of this organ. Consequently, and accordingly, acquiring the data requires costly tools and modalities for efficient data management of the vast data generated that must undergo subsequent quality-control before analysis. However, not every lab has the facilities, personnel or financial capabilities to take on such a daunting task. Recent times has seen the data sets openly made public, sharing generated and analysed data that can aid in further studies as reference models in the new discovered of brain functionality where comparisons can be drawn upon, corroborate emerging protocols and computational models, as well as aiding in the hypothesis of new research lines through the analyses of existing data. The Allen Brain Observatory, of the Allen Institute, has become a benchmark within neuroscience where survey data sets are shared in a comprehensive way (de Vries et al., 2023). Other general repositories such as Figshare (https://figshare.com/) and G-Node Infrastructure (https://gin.g-node.org/), specific to neuroscience, are other modalities for researchers to publicise and share their data.

Since its founding, the Allen Institute has made open data one of its core principles. Specifically, it has become known for generating and sharing *survey* datasets within the field of neuroscience, taking inspiration from domains such as astronomy where such surveys are common.

Until now, many efforts have been made in contributing to the optimisation of various steps forming a pipeline for neuronal mapping. Since the novel development of a tissue clearing technique in the early 1900s by Werner Spalteholz, other techniques followed suit in enhancing structural integrity post-clearing, scalability to tissue volumes and the compatibility with immunochemistry. Nowadays, various reliable techniques can be

employed and selected to be most suited to the target tissue, be it aged human tissue that is notoriously difficult to clear due to its strong auto fluorescence properties and complex composition or residual blood left within tissue before fixation. Reliable tissue labelling strategies, using immunochemistry, have also aided greatly in curating detailed images; the establishment of the chemical synthesis of fluorophores to bioactive reagents provided new grounds in visualising features with great signal and therefore detail. Indeed, rendering tissue transparent has served in maintaining a tissue block whole without physical sectioning (Ueda, Ertürk, et al., 2020), appropriately applied to neuronal circuits expanding over thick sections (Mano et al., 2018). Enhancing the resolution even further by combining these techniques with expansion protocols (Parra-Damas & Saura, 2020) yet these protocols, until now, have been limited to relatively thick slices of around 2mm. From this standpoint in sample preparation, robust protocols are lacking in scalability and reliable replicability. One the one hand, great immunochemistry of tissue labelling can be achieved with thin slices of biological tissue, yet on the other hand the success in limited in the thickness of the sample giving rise to compromised structural preservation of the tissue, tedious preparation and mounting of many individual slices increasing the workload as well as the necessity of mounting and unmounting the samples in an optical set up when a large volume is investigated. To address the scalability of these techniques, technologies to label dense and large tissue samples were designed such as stochastic elecro-transport that requires the construction of a specialised device that drives electro-mobile molecules used for labelling into the tissue via rotating electric fields (S. Y. Kim et al., 2015). An evident drawback of this technique is that it isn't accessible or employable in many research centres due to the requirement of the device.

When considering the required resolution for axon tracing in order to distinguish the full morphology, this has been dependent on the capabilities of the optical system itself and processing techniques. Expansion microscopy techniques have been able to boost the resolution in an image in the sample preparation alone with an expansion factor manageable through expansion buffers or increased through iterative techniques. On the contrary to this favourable optimised factor, a new challenge arises as an effect of the expansion factor; large samples are increasingly difficult to mount and image since conventional light sheet microscopes have yet to be scaled to be capable of imaging tissue volumes to this scale. Other customised light sheet microscopes use vibratomes to physically cut each slice during imaging in order to bring each point of the sample into the illumination and detection imaging plane since objective working distances tend not to extend across an entire expanded mouse brain volume (Zhang et al., 2021).

Expansion microscopy, however, is a ground-breaking technique that supports improved resolution in all dimensions if optimised correctly to the tissue in question. Using standard laboratory equipment, labelling fully intact mouse brains in combination with expansion microscopy is a tedious task which can be time-consuming to optimise, adapt and achieve uniformly.

In this thesis, a technique to successfully label and expand thick slices through to the full mouse brain has been developed using standard laboratory devices and techniques. A light sheet fluorescent microscope has also been designed and constructed using cost-effective equipment in order to facilitate the imaging of tissues as big as the full, expanded mouse brain in order to accomplish data acquisition and imaging without compromising the spatial information preserved in the sample. Furthermore, this pipeline limits the workload in tedious preparing individual slices at each point in the pipeline when large tissue blocks are investigated. The purpose is to produce a technique cable of replication across many labs with the aim of providing the grounds for further research towards the goal of understanding the structural functionality of the brain. Indeed, a collective effort in accumulating useful data by the scientific community accelerates the advancements in this field in which participation should be feasible in many laboratories.

Starting at sample preparation strategies, a literature review and trial of existing protocols enable the selection of techniques compatible with scalability and immunochemistry. Characterised by harsh clearing strategies, signal tends to be lost during this stage as well as being due to the expansion factor. A strong attribute in the original eMAP protocol was the ability to perform labelling post-clearing which limits the factors that could potentially diminish the fluorescent signal. Initial trials revealed the complexities in performing immunolabeling at this level with shallow penetration often seen following rescaled antibody incubation time. When referencing reagents in a review of literature, clearing reagent SDS is known to prevent unsuccessful antibody binding if remaining in the sample and therefore attention should be taken in cleaning the sample post-clearing and pre-staining (Klimas et al., 2023). To this aim, long tissue washing sessions were conducted with PBST as well the use of C12E10, an ionic solvent capable of clearing SDS in short periods. Both steps were tested and implemented in order to provide options in the protocol depending on availability of reagents in a standard lab.

Despite steps taken to clear any remaining chemicals that prevent antibody binding, the attention drew to the permeability of the sample itself since antibody penetration remained a non-uniform factor. In facing this, permeabilisation strategies were tested and

further optimised to the scale of the sample and employed in the final protocol. Since each step in sample preparation and immunolabeling is time consuming, optimisations require long periods before receiving data. To this aim, it is recommended to prepare many samples with various concentrations and incubation times at the same starting point when optimising each step of the protocol for the tissue in question.

The observed outcomes and analysed data in this study showed the importance of complete clearing in a sample and the necessity to effectively wash the tissue following denaturation. This dramatically affects the signal intensity through the diffusion distance when working with the large volumes. Critically, the antibody labelling is substantially improved for fully permeabilised tissues, essential for samples greater than 1mm. Despite some signal seen from the sample, labelling unpermeabilised tissue with expansion microscopy achieves inhomogeneous results and weak signal with lots of features left unbound to fluorescent antibodies. In keeping in mind time efficiency, this step was optimised to take as little time as necessary. Two permeabilisation buffers are recommended, CHAPS 10% and PBS x5, to grant the protocol the flexibility of choosing the most accessible reagent where possible. A third option allows the permeabilisation to begin slowly from fixation, should the sample not be used immediately. The acquired images of strong labelling, with adequate permeabilisation steps, show that signal is greatly improved, inferring that the chances of antibody-antigen binding are increased as well as producing reduced incubation time throughout the entire protocol. This protocol can be further developed since the results of full-permeabilisation suggests that other steps in the procedure could be reduced.

A robust protocol requires an equally robust imaging system. The Ex-LSFM is designed to be easily replicated without the need of specialist devices. With the goal of axonal tracing at the forefront, the dimensions were incorporated in the design in resolution capabilities. The importance of this is that the full pipeline can subsequently be achieved in acquiring spatial data of pre-selected and pre-stained neuronal circuits. What's more is that the design leaves room for further optimisations with ease.

Despite the limited long-working distance objectives available, the Ploessl lens arrangement provides an elegant solution. The trade-off between sophisticated features of illumination objectives, the ability to maintain the intact samples allows for further rounds of testing, multiple rounds of labelling and full use of the data available from one sample. The concept of hierarchical imaging becomes useful here, once regions of interest are identified, the user has the firm knowledge to selectively cut areas of known labelled

anatomy for higher-resolution imaging should that be necessary. Selected features in this pipeline were chosen in order to optimise sample use and flexibility; multiple labelling rounds, post expansion as well as flexible magnification and resolution in the detection arms of the microscope to achieve resolved images of the tissue or for fast, low-resolution images in order to indicate the regions containing labelled features in attaining the spatial data.

The LSFM microscope itself is adaptable to modifying the beam waist through the respective beam expanding systems in the illumination optical path. Multiple illumination wavelengths can be added to the system through dichroic mirrors and combined alignment, supported by the filter wheel located in the infinity space in the high-resolution detection arm and the filter mount in the low-resolution detection arm. Achromatic aberration is tackled through the combination of achromatic doublets for focusing the laser beam. The second modification is the magnification of the detection arms, combinations are discussed for recommended magnifications in Part 3 in which one has flexibility in the magnification of the system, considering the drawback of increased imaging time and data with increased magnification.

In conclusion, LSFM with the enhancement of expansion microscopy offers a unique approach to enhance resolution reducing the need for specialised optical and imaging techniques. To further meet this goal of rendering this approach feasible to the average lab, this pipeline offers a technique with all the benefits of high resolution but at a cost-effective price. Providing a general basis for sample preparation and optical design, each step is highly adaptable with recommendations of the critical steps to consider when optimised for specific biological tissues. The benefits of utilising the full expansion factor provides single-unit micrometre resolution in the sample when imaging. The goal was to achieve imaging of labelled features within a large tissue sample that was accomplished through the imaging of a full and half mouse brains where densely labelled neuron populations in the cerebellum of a tdTomato-labelled mouse brain were imaged. Observed is the delicate neuronal projections spanning across this brain region through strong signals throughout the sample volume. By leveraging this combination of novel methodology combined with feasible, custom-built imaging devices, researchers are able to visualise detailed cellular structures spanning over the entire organ, holding unequivocal value in the pursuit of brain mapping, comprehensively understanding the organisation of its associated architecture. Neuronal circuitry is often not limited to small regions of the brain,

<1mm, therefore this novel combination allows researchers a glimpse into the neuronal trajectories uninterrupted.

To date, the state of the system demonstrates the accessibility into the visualisation of neuronal projections in the whole expanded mouse brain, tested for its feasibility of a variety of large tissue volumes. However, this work serves as a basis in which advancements can be built upon in terms of optical design as well as protocol compatibility using more biological sample types and more biomarkers. While the large-scale approach is useful, the increase in its compatibility enhances its widespread applications. Although time-consuming, optimising the expansion protocol to other samples and biological reagents holds incredible scope for the further investigation of biological processes, notably the tremendous degree with which tissue is rendered transparent, even in large volumes.

Part 4 of this thesis discusses the need for system optimisations, maintenance and diagnostics of a customised LSFM set-up used for long-period imaging of human brain slices contributing to brain mapping. Achieving full comprehensive data of larger tissue volumes, physically sectioned into slices in labour-intensive and long duration, requiring optical systems to continuously function over long periods. The quality of these images rely on fully-functioning optical systems, optimised for image quality.

Precious samples of human tissue should be exposed to illumination for as little time as necessary in order to avoid photo-bleaching or sample damage. To this end, the need to re-acquire data must be kept to a minimum, reducing also the duration of the imaging sessions.

Features of the system are optimised in order to achieve high image quality in a state most optimal for the imaging system, reducing the pressure in the long-term. Techniques that allow the user to precisely align the light sheet to the sample plane and imaging plane must be utilised in taking full advantage of the system. For multi-channel imaging, characterising the stronger illumination arm corresponding to each wavelength enables the user to select the appropriate illumination combination while each laser source requires slightly less pressure, beneficial for long term durability. Despite requiring more attention to details, the benefits of multi-channel imaging allow the user to extract more information from a sample in one imaging session. The user-defined parameters of each light sheet, beam waist location and the tilt of the light sheet, work to achieve high image quality across the multiple channels.

Recognising artefacts caused by defaults in the electrical equipment, potentially occurring over long-time heavy usage, is also critical in system-maintenance. Support through image analysis and appropriate, subsequent tests, this work details procedures to identify the cause. To this aim, post-processed images are immediately inspected during these periods in order to troubleshoot before continuing.

In short, imaging of thin slices from large tissue blocks requires lengthy imaging session that can put pressure on optical systems. The need to maintain the component functionality is critical in avoiding the need to re-acquire delicate images should issues occur during the process. Understanding the use for each feature in an advanced set-up allows the user to achieve the highest image quality possible. User-modifiable parameters essentially allow the fine adjustment to the system for intricate discrepancies, for example the focus for each wavelength when a sample is labelled with multiple probes.

To conclude, LSFM combined with robust sample preparation techniques has revolutionised the world of brain mapping. The plethora of adaptations and combinations elevate the possibilities of extracting spatial information of the anatomical neuronal structures in the mammalian brain. Various techniques can be employed to achieve single-unit micrometre resolution to meet the needs of the application. While many trade-offs exist, innumerable modifications can be made to suit the application and desired outcome.

Future outlook

The work in the thesis consisted of the development of a reliable sample preparation and imaging pipe line with the benefits of the multiple rounds of testing in a single sample following the procedure of initial preparations, immunolabeling, tissue expanding and imaging. Indeed, the cost-effective nature of this procedure endorses its replicability in other labs as well its ability to be further optimised and modified to suit varying biological applications bridging the gap between achievable resolution and limited budgets.

With the target of an expanded mouse brain at the centre of design, this system is not limited to this application since other organs and tissue complexes are of these dimensions. The expansion protocol is yet to be tested on other organ tissue and a complementary route to explore going forward. Employing expansion microscopy with competent imaging systems enables the exploration of other full organs of these dimensions. Spatial relationships and morphological interactions across the scale of a full organ provide essential information in developing the understanding of biological function. The ability to map the complete organisation uninterrupted is fundamental in capturing system-level compositions. Sub-sampling through the physical section of the sample is an unideal approach due to complex data management and post-processing techniques and added risk of sample damage and error. This platform along with improved resolution provided in the sample itself, is a simple and effective way in fulfilling this holistic approach in a cost-effective and simplified way.

Until now, GFP and tdTomato have been established as compatible with the modified eMAP protocol. In going forward, the compatibility of other antibodies should be tested to widen the application and explore other neuronal circuits. In parallel, a promising improvement of this pipeline is to subject a sample to multiplexing with multiple probes simultaneously. Thus, the detection arms could be modified to support the simultaneous acquisition of two wavelength channels. In avoiding cross-talk, the two illumination arms would be separated as the sample moves through two independent light sheets in which narrow-bandwidth optical filters would serve in collecting only the desired photons to the respective illumination arm. The sample would then be rotated 180° for imaging of the second half. A motorised, rotational translational stage should be implemented to allow easy user control.

Arguably, the critical limiting factor remains the working distance of the detection objective, restricting the axial distance of the system yet adequate manipulation and

creative optical configurations, stage positioning and sample mounting makes the light sheet microscope a versatile tool in large-scale imaging. To this point a sample with a maximum volumetric composition of 84 mm x 70 mm x 50 mm (294 cm^3) can be acquired in its entirety. Mouse organs fall within the dimensions of that of the brain and as a result, could be readily imaged in the Ex-LSFM developed. Looking forward, the wide scale applications of this innovative combination holds tremendous potential in large-scale data accumulation since doors are opened to wider participation.

Continuing the development of PFPE as a cuvette material would take steps forward in improving imaging quality. Maintaining media with the same refractive index reduces the refractive effects, improving the transmission percentage, characterised at 92% for commercial Plexiglas used currently.

For improved axial resolution, to achieve an effective resolution when combined with expansion microscopy of that closer to a dendrite,~<2µm, the resulting beam waist should be reduced. Although this work primarily focuses on resolving brain features, this technique holds resolution abilities capable of cellular resolution across other tissue types.

Increased resolution generates, particularly across large volumes, has the potential to generate torrents worth of data. The large data sets contain resourceful information that needs to be adequately collected, managed, processed, reviewed and shared. In striving towards the goal of higher resolution, this consideration must also be affronted. An alternative approach that we will integrate into this project is 'intelligent' imaging. What this means is that the imaging system would be capable of identifying fluorescent signals in the sample, for example the signal from neuronal projections, and therefore proceeding to trace this signal, only imaging points in which the signal exists. This would place limitations on the data field, effectively tracing the neuronal morphology, or that of other features in biological tissue. Successively, the data acquired would be of high quality, containing only the spatial information of the targeted infrastructure. A technique in mind would be to use appropriate intensity thresholds to identify fluorescence followed by the analyses of adjacent tiles in order to directionally proceed with the image acquisition.

To summarise, the work in this thesis provides a pipeline supporting the study of anatomical composition in fixed tissues. The knowledge applied at this level forms the basis of understanding the architectural system-level structures and functionality that are relevant in many other fields of biological sciences. Cognitive development and its subsequent decline due to disease have seen structural changes in some neuronal

structures. With the right tools, as developed in this thesis, the link between structural anatomy and measured functionality can be investigated, bridging more the gap between the geometrical arrangement of the brain and the corresponding and consequential behavioural impact. Contributions of research at all levels is immeasurable, particularly when unlocking doors for application in human disease. Indeed, without accessible tools, limitations are put on the research itself and the researchers; the goal of this work was to help bridge the gap between what is accessible and not.

References

Ahrens, M. B., Orger, M. B., Robson, D. N., Li, J. M., & Keller, P. J. (2013). Whole-brain functional imaging at cellular resolution using light-sheet microscopy. *Nature Methods, 10*(5), 413-420. doi:10.1038/nmeth.2434

Al-Hasani, R., McCall, J. G., Shin, G., Gomez, A. M., Schmitz, G. P., Bernardi, J. M., . . . Bruchas, M. R. (2015). Distinct Subpopulations of Nucleus Accumbens Dynorphin Neurons Drive Aversion and Reward. *Neuron, 87*(5), 1063-1077. doi:10.1016/j.neuron.2015.08.019

Albert-Smet, I., Marcos-Vidal, A., Vaquero, J. J., Desco, M., Muñoz-Barrutia, A., & Ripoll, J. (2019). Applications of Light-Sheet Microscopy in Microdevices. *Front Neuroanat, 13*. doi:10.3389/fnana.2019.00001

Arias, A., Manubens-Gil, L., & Dierssen, M. (2022). Fluorescent transgenic mouse models for whole-brain imaging in health and disease. *Front Mol Neurosci, 15*, 958222. doi:10.3389/fnmol.2022.958222

Austin, C. P., Battey, J. F., Bradley, A., Bucan, M., Capecchi, M., Collins, F. S., . . . Zambrowicz, B. (2004). The knockout mouse project. *Nat Genet, 36*(9), 921-924. doi:10.1038/ng0904-921

Azaripour, A., Lagerweij, T., Scharfbillig, C., Jadczak, A. E., Willershausen, B., & Van Noorden, C. J. (2016). A survey of clearing techniques for 3D imaging of tissues with special reference to connective tissue. *Prog Histochem Cytochem, 51*(2), 9-23. doi:10.1016/j.proghi.2016.04.001

Bargmann, C. I., & Marder, E. (2013). From the connectome to brain function. *Nat Methods, 10*(6), 483-490. doi:10.1038/nmeth.2451

Bargmann, C. I., & Marder, E. (2013). From the connectome to brain function. *Nature Methods, 10*(6), 483-490. doi:10.1038/nmeth.2451

Bartholin, E. (1670). An Accompt of Sundry Experiments Made and Communicated by That Learn'd Mathematician, Dr. Erasmus Bartholin, upon a Chrystal-Like Body, Sent to Him Out of Island. *Philosophical Transactions (1665-1678), 5*, 2039-2048.

Bartlett, J. S., & Samulski, R. J. (1998). Fluorescent viral vectors: a new technique for the pharmacological analysis of gene therapy. *Nat Med, 4*(5), 635-637. doi:10.1038/nm0598-635

Bashkatov, A. N., Berezin, K. V., Dvoretskiy, K. N., Chernavina, M. L., Genina, E. A., Genin, V. D., . . . Tuchin, V. V. (2018). Measurement of tissue optical properties in the context of tissue optical clearing. *J Biomed Opt, 23*(9), 1-31. doi:10.1117/1.Jbo.23.9.091416

Baumgart, E., & Kubitscheck, U. (2012). Scanned light sheet microscopy with confocal slit detection. *Optics Express, 20*(19), 21805-21814. doi:10.1364/OE.20.021805

Becirovic, E., Böhm, S., Nguyen, O. N. P., Riedmayr, L. M., Hammelmann, V., Schön, C., . . . Michalakis, S. (2016). AAV Vectors for FRET-Based Analysis of Protein-Protein Interactions in Photoreceptor Outer Segments. *Frontiers in Neuroscience, 10*. doi:10.3389/fnins.2016.00356

Beghin, A., Grenci, G., Sahni, G., Guo, S., Rajendiran, H., Delaire, T., . . . Viasnoff, V. (2022). Automated high-speed 3D imaging of organoid cultures with multi-scale phenotypic quantification. *Nat Methods, 19*(7), 881-892. doi:10.1038/s41592-022-01508-0

Chalfie, M., Tu, Y., Euskirchen, G., Ward, W. W., & Prasher, D. C. (1994). Green fluorescent protein as a marker for gene expression. *Science, 263*(5148), 802-805. doi:10.1126/science.8303295

Chang, J.-B., Chen, F., Yoon, Y.-G., Jung, E. E., Babcock, H., Kang, J. S., . . . Boyden, E. S. (2017). Iterative expansion microscopy. *Nature Methods, 14*(6), 593-599. doi:10.1038/nmeth.4261

Chen, B. C., Legant, W. R., Wang, K., Shao, L., Milkie, D. E., Davidson, M. W., . . . Betzig, E. (2014). Lattice light-sheet microscopy: imaging molecules to embryos at high spatiotemporal resolution. *Science, 346*(6208), 1257998. doi:10.1126/science.1257998

Chen, F., Tillberg, P. W., & Boyden, E. S. (2015). Optical imaging. Expansion microscopy. *Science, 347*(6221), 543-548. doi:10.1126/science.1260088

Chen, H., Huang, T., Yang, Y., Yao, X., Huo, Y., Wang, Y., . . . Guo, Z. V. (2021). Sparse imaging and reconstruction tomography for high-speed high-resolution whole-brain imaging. *Cell Reports Methods, 1*(6), 100089. doi:https://doi.org/10.1016/j.crmeth.2021.100089

Chozinski, T. J., Halpern, A. R., Okawa, H., Kim, H. J., Tremel, G. J., Wong, R. O., & Vaughan, J. C. (2016). Expansion microscopy with conventional antibodies and fluorescent proteins. *Nat Methods, 13*(6), 485-488. doi:10.1038/nmeth.3833

Chrambach, A. (1985). *The practice of quantitative gel electrophoresis*. In Advanced methods in the biological sciences. Retrieved from http://books.google.com/books?id=Dna3AAAAIAAJ

Chung, K., & Deisseroth, K. (2013). CLARITY for mapping the nervous system. *Nat Methods, 10*(6), 508-513. doi:10.1038/nmeth.2481

Collins, F. S., & Fink, L. (1995). The Human Genome Project. *Alcohol Health Res World, 19*(3), 190-195.

Costantini, I., Ghobril, J.-P., Di Giovanna, A. P., Mascaro, A. L. A., Silvestri, L., Müllenbroich, M. C., . . . Pavone, F. S. (2015). A versatile clearing agent for multi-modal brain imaging. *Scientific Reports, 5*(1), 9808. doi:10.1038/srep09808

Costantini, I., Morgan, L., Yang, J., Balbastre, Y., Varadarajan, D., Pesce, L., . . . Hof, P. R. (2023). A cellular resolution atlas of Broca's area. *Science Advances, 9*(41), eadg3844. doi:doi:10.1126/sciadv.adg3844

Croce, A. C., & Bottiroli, G. (2014). Autofluorescence spectroscopy and imaging: a tool for biomedical research and diagnosis. *Eur J Histochem, 58*(4), 2461. doi:10.4081/ejh.2014.2461

Daetwyler, S., & Huisken, J. (2016). Fast Fluorescence Microscopy with Light Sheets. *Biol Bull, 231*(1), 14-25. doi:10.1086/689588

Davenport, D., Nicol, J. A. C., & Russell, F. S. (1955). Luminescence in Hydromedusae. *Proceedings of the Royal Society of London. Series B - Biological Sciences, 144*(916), 399-411. doi:doi:10.1098/rspb.1955.0066

de Vries, S. E. J., Siegle, J. H., & Koch, C. (2023). Sharing neurophysiology data from the Allen Brain Observatory. *Elife, 12*. doi:10.7554/eLife.85550

DeFelipe, J. (2015). The anatomical problem posed by brain complexity and size: a potential solution. *Front Neuroanat, 9*, 104. doi:10.3389/fnana.2015.00104

Denk, W., Strickler, J. H., & Webb, W. W. (1990). Two-Photon Laser Scanning Fluorescence Microscopy. *Science, 248*(4951), 73-76. doi:doi:10.1126/science.2321027

Douw, L., Nissen, I. A., Fitzsimmons, S. M. D. D., Santos, F. A. N., Hillebrand, A., Straaten, E. C. W. v., . . . Goriounova, N. A. (2021). Neuronal morphology and physiology, functional brain networks and memory in temporal lobe epilepsy. *bioRxiv*, 2021.2001.2031.428369. doi:10.1101/2021.01.31.428369

Durnin, J., Miceli, J., Jr., & Eberly, J. H. (1987). Diffraction-free beams. *Phys Rev Lett, 58*(15), 1499-1501. doi:10.1103/PhysRevLett.58.1499

Ertürk, A., Becker, K., Jährling, N., Mauch, C. P., Hojer, C. D., Egen, J. G., . . . Dodt, H.-U. (2012). Three-dimensional imaging of solvent-cleared organs using 3DISCO. *Nature Protocols, 7*(11), 1983-1995. doi:10.1038/nprot.2012.119

Foster, D. S., Nguyen, A. T., Chinta, M., Salhotra, A., Jones, R. E., Mascharak, S., . . . Longaker, M. T. (2019). A Clearing Technique to Enhance Endogenous Fluorophores in Skin and Soft Tissue. *Scientific Reports, 9*(1), 15791. doi:10.1038/s41598-019-50359-x

Freifeld, L., Odstrcil, I., Förster, D., Ramirez, A., Gagnon, J. A., Randlett, O., . . . Boyden, E. S. (2017). Expansion microscopy of zebrafish for neuroscience and developmental biology studies. *Proc Natl Acad Sci U S A, 114*(50), E10799-e10808. doi:10.1073/pnas.1706281114

Germond, A., Fujita, H., Ichimura, T., & Watanabe, T. M. (2016). Design and development of genetically encoded fluorescent sensors to monitor intracellular chemical and physical parameters. *Biophysical reviews, 8*(2), 121-138. doi:10.1007/s12551-016-0195-9

Gu, S., Xing, C., Han, J., Tso, M. O., & Hong, J. (2009). Differentiation of rabbit bone marrow mesenchymal stem cells into corneal epithelial cells in vivo and ex vivo. *Mol Vis, 15*, 99-107.

Guenthner, C. J., Miyamichi, K., Yang, H. H., Heller, H. C., & Luo, L. (2013). Permanent genetic access to transiently active neurons via TRAP: targeted recombination in active populations. *Neuron, 78*(5), 773-784. doi:10.1016/j.neuron.2013.03.025

Haass-Koffler, C. L., Naeemuddin, M., & Bartlett, S. E. (2012). An analytical tool that quantifies cellular morphology changes from three-dimensional fluorescence images. *J Vis Exp*(66), e4233. doi:10.3791/4233

Hama, H., Kurokawa, H., Kawano, H., Ando, R., Shimogori, T., Noda, H., . . . Miyawaki, A. (2011). Scale: a chemical approach for fluorescence imaging and reconstruction of transparent mouse brain. *Nat Neurosci, 14*(11), 1481-1488. doi:10.1038/nn.2928

Haslehurst, P., Yang, Z., Dholakia, K., & Emptage, N. (2018). Fast volume-scanning light sheet microscopy reveals transient neuronal events. *Biomed Opt Express, 9*(5), 2154-2167. doi:10.1364/boe.9.002154

Hickey, J. W., Neumann, E. K., Radtke, A. J., Camarillo, J. M., Beuschel, R. T., Albanese, A., . . . Saka, S. K. (2022). Spatial mapping of protein composition and tissue organization: a primer for multiplexed antibody-based imaging. *Nature Methods, 19*(3), 284-295. doi:10.1038/s41592-021-01316-y

Huisken, J., & Stainier, D. Y. (2007). Even fluorescence excitation by multidirectional selective plane illumination microscopy (mSPIM). *Opt Lett, 32*(17), 2608-2610. doi:10.1364/ol.32.002608

Huisken, J., & Stainier, D. Y. (2009). Selective plane illumination microscopy techniques in developmental biology. *Development, 136*(12), 1963-1975. doi:10.1242/dev.022426

Huisken, J., Swoger, J., Del Bene, F., Wittbrodt, J., & Stelzer, E. H. (2004). Optical sectioning deep inside live embryos by selective plane illumination microscopy. *Science, 305*(5686), 1007-1009. doi:10.1126/science.1100035

Hüpfel, M., Yu. Kobitski, A., Zhang, W., & Nienhaus, G. U. (2021). Wavelet-based background and noise subtraction for fluorescence microscopy images. *Biomedical Optics Express, 12*(2), 969-980. doi:10.1364/BOE.413181

Ikawa, M., Kominami, K., Yoshimura, Y., Tanaka, K., Nishimune, Y., & Okabe, M. (1995). Green fluorescent protein as a marker in transgenic mice. *Dev Growth Differ, 37*(4), 455-459. doi:10.1046/j.1440-169X.1995.t01-2-00012.x

Im, K., Mareninov, S., Diaz, M. F. P., & Yong, W. H. (2019). An Introduction to Performing Immunofluorescence Staining. *Methods Mol Biol, 1897*, 299-311. doi:10.1007/978-1-4939-8935-5_26

Kasha, M. (1950). Characterization of electronic transitions in complex molecules. *Discussions of the Faraday Society, 9*(0), 14-19. doi:10.1039/DF9500900014

Ke, M.-T., Fujimoto, S., & Imai, T. (2013). SeeDB: a simple and morphology-preserving optical clearing agent for neuronal circuit reconstruction. *Nat Neurosci, 16*(8), 1154-1161. doi:10.1038/nn.3447

Keller, Philipp J., & Ahrens, Misha B. (2015). Visualizing Whole-Brain Activity and Development at the Single-Cell Level Using Light-Sheet Microscopy. *Neuron, 85*(3), 462-483. doi:https://doi.org/10.1016/j.neuron.2014.12.039

Keller, P. J., & Stelzer, E. H. (2010). Digital scanned laser light sheet fluorescence microscopy. *Cold Spring Harb Protoc, 2010*(5), pdb.top78. doi:10.1101/pdb.top78

Kidger, M. J., & Society of Photo-optical Instrumentation, E. (2002). *Fundamental optical design*. In. Retrieved from https://doi.org/10.1117/3.397107 doi:10.1117/3.397107

Kiernan, J. A. (2000). Formaldehyde, Formalin, Paraformaldehyde And Glutaraldehyde: What They Are And What They Do. *Microscopy Today, 8*(1), 8-13. doi:10.1017/S1551929500057060

Kim, D., & Kim, B. (2022). Anatomical and Functional Differences in the Sex-Shared Neurons of the Nematode C. elegans. *Front Neuroanat, 16*, 906090. doi:10.3389/fnana.2022.906090

Kim, M. H., Radaelli, C., Thomsen, E. R., Monet, D., Chartrand, T., Jorstad, N. L., . . . Lein, E. (2023). Target cell-specific synaptic dynamics of excitatory to inhibitory neuron

connections in supragranular layers of human neocortex. *Elife, 12*. doi:10.7554/eLife.81863

Kim, S. Y., Cho, J. H., Murray, E., Bakh, N., Choi, H., Ohn, K., . . . Chung, K. (2015). Stochastic electrotransport selectively enhances the transport of highly electromobile molecules. *Proc Natl Acad Sci U S A, 112*(46), E6274-6283. doi:10.1073/pnas.1510133112

Klimas, A., Gallagher, B. R., Wijesekara, P., Fekir, S., DiBernardo, E. F., Cheng, Z., . . . Zhao, Y. (2023). Magnify is a universal molecular anchoring strategy for expansion microscopy. *Nat Biotechnol, 41*(6), 858-869. doi:10.1038/s41587-022-01546-1

Křížek, P., Lukeš, T., Ovesný, M., Fliegel, K., & Hagen, G. M. (2016). SIMToolbox: a MATLAB toolbox for structured illumination fluorescence microscopy. *Bioinformatics, 32*(2), 318-320. doi:10.1093/bioinformatics/btv576

Ku, T., Swaney, J., Park, J.-Y., Albanese, A., Murray, E., Cho, J. H., . . . Chung, K. (2016). Multiplexed and scalable super-resolution imaging of three-dimensional protein localization in size-adjustable tissues. *Nat Biotechnol, 34*(9), 973-981. doi:10.1038/nbt.3641

Levanon, K., Ng, V., Piao, H. Y., Zhang, Y., Chang, M. C., Roh, M. H., . . . Drapkin, R. (2010). Primary ex vivo cultures of human fallopian tube epithelium as a model for serous ovarian carcinogenesis. *Oncogene, 29*(8), 1103-1113. doi:10.1038/onc.2009.402

Lindek, S., Pick, R., & Stelzer, E. H. K. (1994). Confocal theta microscope with three objective lenses. *Review of Scientific Instruments, 65*(11), 3367-3372. doi:10.1063/1.1144574

Lohse, M., Bajo, V. M., King, A. J., & Willmore, B. D. B. (2020). Neural circuits underlying auditory contrast gain control and their perceptual implications. *Nature Communications, 11*(1), 324. doi:10.1038/s41467-019-14163-5

Long, B., Zhou, Z., Cetin, A., Ting, J., Gwinn, R., Tasic, B., . . . Peng, H. (2017). SmartScope2: Simultaneous Imaging and Reconstruction of Neuronal Morphology. *Scientific Reports, 7*(1), 9325. doi:10.1038/s41598-017-10067-w

Lux, K., Goerlitz, N., Schlemminger, S., Perabo, L., Goldnau, D., Endell, J., . . . Büning, H. (2005). Green Fluorescent Protein-Tagged Adeno-Associated Virus Particles Allow the Study of Cytosolic and Nuclear Trafficking. *Journal of Virology, 79*(18), 11776-11787. doi:doi:10.1128/jvi.79.18.11776-11787.2005

Maafa, I. M. (2023). Inhibition of Free Radical Polymerization: A Review. *Polymers (Basel), 15*(3). doi:10.3390/polym15030488

Mano, T., Albanese, A., Dodt, H. U., Erturk, A., Gradinaru, V., Treweek, J. B., . . . Ueda, H. R. (2018). Whole-Brain Analysis of Cells and Circuits by Tissue Clearing and Light-Sheet Microscopy. *J Neurosci, 38*(44), 9330-9337. doi:10.1523/jneurosci.1677-18.2018

Masters, B. R., & So, P. T. (2004). Antecedents of two-photon excitation laser scanning microscopy. *Microsc Res Tech, 63*(1), 3-11. doi:10.1002/jemt.10418

Mazi, W. (2019). NEAR-INFRARED FLUORESCENT PROBES FOR SENSITIVE DETERMINATION OF LYSOSOMAL & MITOCHONDRIAL pH IN LIVE CELLS.

McFarlan, A. R., Chou, C. Y. C., Watanabe, A., Cherepacha, N., Haddad, M., Owens, H., & Sjöström, P. J. (2023). The plasticitome of cortical interneurons. *Nature Reviews Neuroscience, 24*(2), 80-97. doi:10.1038/s41583-022-00663-9

Menter, P. A., & Drive, A. N. (2000). *Acrylamide Polymerization — A Practical Approach*.

Method of the Year 2014. (2015). *Nature Methods, 12*(1), 1-1. doi:10.1038/nmeth.3251

Monici, M. (2005). Cell and tissue autofluorescence research and diagnostic applications. *Biotechnol Annu Rev, 11*, 227-256. doi:10.1016/s1387-2656(05)11007-2

Müllenbroich, M. C., Silvestri, L., Di Giovanna, A. P., Mazzamuto, G., Costantini, I., Sacconi, L., & Pavone, F. S. (2018). High-Fidelity Imaging in Brain-Wide Structural Studies Using Light-Sheet Microscopy. *eNeuro, 5*(6). doi:10.1523/eneuro.0124-18.2018

Müllenbroich, M. C., Silvestri, L., Onofri, L., Costantini, I., Hoff, M. V., Sacconi, L., . . . Pavone, F. S. (2015). Comprehensive optical and data management infrastructure for high-throughput light-sheet microscopy of whole mouse brains. *Neurophotonics, 2*(4), 041404. doi:10.1117/1.NPh.2.4.041404

Nehrhoff, I., Ripoll, J., Samaniego, R., Desco, M., & Gómez-Gaviro, M. V. (2017). Looking inside the heart: a see-through view of the vascular tree. *Biomed Opt Express, 8*(6), 3110-3118. doi:10.1364/boe.8.003110

Nelson, S. B., & Valakh, V. (2015). Excitatory/Inhibitory Balance and Circuit Homeostasis in Autism Spectrum Disorders. *Neuron, 87*(4), 684-698. doi:10.1016/j.neuron.2015.07.033

Oh, S. W., Harris, J. A., Ng, L., Winslow, B., Cain, N., Mihalas, S., . . . Zeng, H. (2014). A mesoscale connectome of the mouse brain. *Nature, 508*(7495), 207-214. doi:10.1038/nature13186

Okay, O., & Sariisik, S. B. (2000). Swelling behavior of poly(acrylamide-co-sodium acrylate) hydrogels in aqueous salt solutions: theory versus experiments. *European Polymer Journal, 36*(2), 393-399. doi:https://doi.org/10.1016/S0014-3057(99)00058-0

Olarte, O. E., Andilla, J., Gualda, E. J., & Loza-Alvarez, P. (2018). Light-sheet microscopy: a tutorial. *Advances in Optics and Photonics, 10*(1), 111-179. doi:10.1364/AOP.10.000111

Park, J., Khan, S., Yun, D. H., Ku, T., Villa, K. L., Lee, J. E., . . . Chung, K. (2021). Epitope-preserving magnified analysis of proteome (eMAP). *Science Advances, 7*(46), eabf6589. doi:doi:10.1126/sciadv.abf6589

Parra-Damas, A., & Saura, C. A. (2020). Tissue Clearing and Expansion Methods for Imaging Brain Pathology in Neurodegeneration: From Circuits to Synapses and Beyond. *Frontiers in Neuroscience, 14*. doi:10.3389/fnins.2020.00914

Paschotta, R. Gaussian Beams. In *RP Photonics Encyclopedia*.

Paschotta, R. Numerical Aperture. In *RP Photonics Encyclopedia*.

Pesce, L., Scardigli, M., Gavryusev, V., Laurino, A., Mazzamuto, G., Brady, N., . . . Pavone, F. S. (2022). 3D molecular phenotyping of cleared human brain tissues with light-sheet fluorescence microscopy. *Commun Biol, 5*(1), 447. doi:10.1038/s42003-022-03390-0

Power, R. M., & Huisken, J. (2017). A guide to light-sheet fluorescence microscopy for multiscale imaging. *Nature Methods, 14*(4), 360-373. doi:10.1038/nmeth.4224

Pusterla, J. M., Malfatti-Gasperini, A. A., Puentes-Martinez, X. E., Cavalcanti, L. P., & Oliveira, R. G. (2017). Refractive index and thickness determination in Langmuir monolayers of myelin lipids. *Biochimica et Biophysica Acta (BBA) - Biomembranes, 1859*(5), 924-930. doi:https://doi.org/10.1016/j.bbamem.2017.02.005

Remacha, E., Friedrich, L., Vermot, J., & Fahrbach, F. O. (2020). How to define and optimize axial resolution in light-sheet microscopy: a simulation-based approach. *Biomed Opt Express, 11*(1), 8-26. doi:10.1364/boe.11.000008

Renier, N., Wu, Z., Simon, D. J., Yang, J., Ariel, P., & Tessier-Lavigne, M. (2014). iDISCO: a simple, rapid method to immunolabel large tissue samples for volume imaging. *Cell, 159*(4), 896-910. doi:10.1016/j.cell.2014.10.010

Reynaud, E. G., Krzic, U., Greger, K., & Stelzer, E. H. (2008). Light sheet-based fluorescence microscopy: more dimensions, more photons, and less photodamage. *Hfsp j, 2*(5), 266-275. doi:10.2976/1.2974980

Rodriguez-Gatica, J. E., Iefremova, V., Sokhranyaeva, L., Au Yeung, S. W. C., Breitkreuz, Y., Brüstle, O., . . . Kubitscheck, U. (2022). Imaging three-dimensional brain organoid architecture from meso- to nanoscale across development. *Development, 149*(20). doi:10.1242/dev.200439

Ruder, L., Schina, R., Kanodia, H., Valencia-Garcia, S., Pivetta, C., & Arber, S. (2021). A functional map for diverse forelimb actions within brainstem circuitry. *Nature, 590*(7846), 445-450. doi:10.1038/s41586-020-03080-z

Rusch, H., Brammerloh, M., Stieler, J., Sonntag, M., Mohammadi, S., Weiskopf, N., . . . Morawski, M. (2022). Finding the best clearing approach - Towards 3D wide-scale multimodal imaging of aged human brain tissue. *Neuroimage, 247*, 118832. doi:10.1016/j.neuroimage.2021.118832

Sancataldo, G., Gavryusev, V., de Vito, G., Turrini, L., Locatelli, M., Fornetto, C., . . . Pavone, F. S. (2019). Flexible Multi-Beam Light-Sheet Fluorescence Microscope for Live Imaging Without Striping Artifacts. *Front Neuroanat, 13*. doi:10.3389/fnana.2019.00007

Schindelin, J., Arganda-Carreras, I., Frise, E., Kaynig, V., Longair, M., Pietzsch, T., . . . Cardona, A. (2012). Fiji: an open-source platform for biological-image analysis. *Nature Methods, 9*(7), 676-682. doi:10.1038/nmeth.2019

Schmid, M., Prinz, T. K., Stäbler, A., & Sängerlaub, S. (2017). Effect of Sodium Sulfite, Sodium Dodecyl Sulfate, and Urea on the Molecular Interactions and Properties of Whey Protein Isolate-Based Films. *Frontiers in Chemistry, 4*. doi:10.3389/fchem.2016.00049

Schweizer, T., Kubach, H., & Koch, T. (2021). Investigations to characterize the interactions of light radiation, engine operating media and fluorescence tracers for the use of qualitative light-induced fluorescence in engine systems. *Automotive and Engine Technology, 6*(3), 275-287. doi:10.1007/s41104-021-00092-3

Sharma, K. K. (2006). *Optics: Principles and Applications*: Elsevier Science.

Shimomura, O., Johnson, F. H., & Saiga, Y. (1962). Extraction, purification and properties of aequorin, a bioluminescent protein from the luminous hydromedusan, Aequorea. *J Cell Comp Physiol, 59*, 223-239. doi:10.1002/jcp.1030590302

Strnad, P., Gunther, S., Reichmann, J., Krzic, U., Balazs, B., de Medeiros, G., . . . Ellenberg, J. (2016). Inverted light-sheet microscope for imaging mouse pre-implantation development. *Nature Methods, 13*(2), 139-142. doi:10.1038/nmeth.3690

Szegedi, V., Paizs, M., Baka, J., Barzó, P., Molnár, G., Tamas, G., & Lamsa, K. (2020). Robust perisomatic GABAergic self-innervation inhibits basket cells in the human and mouse supragranular neocortex. *Elife, 9*. doi:10.7554/eLife.51691

Tang, J., & Han, K. Y. (2019). Low-photobleaching line-scanning confocal microscopy using dual inclined beams. *J Biophotonics, 12*(10), e201900075. doi:10.1002/jbio.201900075

Taube, J. M., Akturk, G., Angelo, M., Engle, E. L., Gnjatic, S., Greenbaum, S., . . . Bifulco, C. B. (2020). The Society for Immunotherapy of Cancer statement on best practices for multiplex immunohistochemistry (IHC) and immunofluorescence (IF) staining and validation. *J Immunother Cancer, 8*(1). doi:10.1136/jitc-2019-000155

Tillberg, P. W., Chen, F., Piatkevich, K. D., Zhao, Y., Yu, C.-C., English, B. P., . . . Boyden, E. S. (2016). Protein-retention expansion microscopy of cells and tissues labeled using standard fluorescent proteins and antibodies. *Nat Biotechnol, 34*(9), 987-992. doi:10.1038/nbt.3625

Toader, B., Boulanger, J., Korolev, Y., Lenz, M. O., Manton, J., Schönlieb, C. B., & Mureşan, L. (2022). Image Reconstruction in Light-Sheet Microscopy: Spatially Varying Deconvolution and Mixed Noise. *J Math Imaging Vis, 64*(9), 968-992. doi:10.1007/s10851-022-01100-3

Tokita, M. (2022). Phase Transition of Gels-A Review of Toyoich Tanaka's Research. *Gels, 8*(9). doi:10.3390/gels8090550

Ueda, H. R., Dodt, H. U., Osten, P., Economo, M. N., Chandrashekar, J., & Keller, P. J. (2020). Whole-Brain Profiling of Cells and Circuits in Mammals by Tissue Clearing and Light-Sheet Microscopy. *Neuron, 106*(3), 369-387. doi:10.1016/j.neuron.2020.03.004

Ueda, H. R., Ertürk, A., Chung, K., Gradinaru, V., Chédotal, A., Tomancak, P., & Keller, P. J. (2020). Tissue clearing and its applications in neuroscience. *Nat Rev Neurosci, 21*(2), 61-79. doi:10.1038/s41583-019-0250-1

Voie, A. H., Burns, D. H., & Spelman, F. A. (1993). Orthogonal-plane fluorescence optical sectioning: three-dimensional imaging of macroscopic biological specimens. *J Microsc, 170*(Pt 3), 229-236. doi:10.1111/j.1365-2818.1993.tb03346.x

Voie, A. H., & Spelman, F. A. (1995). Three-dimensional reconstruction of the cochlea from two-dimensional images of optical sections. *Comput Med Imaging Graph, 19*(5), 377-384. doi:10.1016/0895-6111(95)00034-8

Wacker, I., Spomer, W., Hofmann, A., Thaler, M., Hillmer, S., Gengenbach, U., & Schröder, R. R. (2016). Hierarchical imaging: a new concept for targeted imaging of large volumes from cells to tissues. *BMC Cell Biology, 17*(1), 38. doi:10.1186/s12860-016-0122-8

Wan, Y., McDole, K., & Keller, P. J. (2019). Light-Sheet Microscopy and Its Potential for Understanding Developmental Processes. *Annu Rev Cell Dev Biol, 35*, 655-681. doi:10.1146/annurev-cellbio-100818-125311

Wassie, A. T., Zhao, Y., & Boyden, E. S. (2019). Expansion microscopy: principles and uses in biological research. *Nat Methods, 16*(1), 33-41. doi:10.1038/s41592-018-0219-4

Winnubst, J., Bas, E., Ferreira, T. A., Wu, Z., Economo, M. N., Edson, P., . . . Chandrashekar, J. (2019). Reconstruction of 1,000 Projection Neurons Reveals New Cell Types and Organization of Long-Range Connectivity in the Mouse Brain. *Cell, 179*(1), 268-281.e213. doi:https://doi.org/10.1016/j.cell.2019.07.042

Wong, H. H.-W., Chou, C. Y. C., Watt, A. J., & Sjöström, P. J. (2023). Comparing mouse and human brains. *Elife, 12*, e90017. doi:10.7554/eLife.90017

Wu, Y., Wawrzusin, P., Senseney, J., Fischer, R. S., Christensen, R., Santella, A., . . . Shroff, H. (2013). Spatially isotropic four-dimensional imaging with dual-view plane illumination microscopy. *Nat Biotechnol, 31*(11), 1032-1038. doi:10.1038/nbt.2713

Zhang, Z., Yao, X., Yin, X., Ding, Z., Huang, T., Huo, Y., . . . Guo, Z. V. (2021). Multi-Scale Light-Sheet Fluorescence Microscopy for Fast Whole Brain Imaging. *Front Neuroanat, 15*, 732464. doi:10.3389/fnana.2021.732464

Zhao, J., Lai, H. M., Qi, Y., He, D., & Sun, H. (2021). Current Status of Tissue Clearing and the Path Forward in Neuroscience. *ACS Chem Neurosci, 12*(1), 5-29. doi:10.1021/acschemneuro.0c00563

Zhao, S., Todorov, M. I., Cai, R., Maskari, R. A., Steinke, H., Kemter, E., . . . Ertürk, A. (2020). Cellular and Molecular Probing of Intact Human Organs. *Cell, 180*(4), 796-812.e719. doi:10.1016/j.cell.2020.01.030